1994

Weld overlay coatings for erosion control

Boris Feliksovich Levin
Lehigh University

AUTHOR:

Levin, Boris Feliksovich

TITLE:

Weld Overlay Coatings for Erosion Control

DATE: October 9, 1994

WELD OVERLAY COATINGS FOR EROSION CONTROL

by

Boris Feliksovich Levin

A Thesis

Presented to the Graduate Committee

of Lehigh University

in Candidacy for Degree of
Master of Science

in

Materials Science and Engineering

Lehigh University

1994

Certificate of Approval

This thesis is accepted and approved in partial fulfillment of the requirements for the degree of Master of Science.

8/26/94
Date

Professor in charge.

Department Chairman

In memory of my mom
Anna Isaakovna Levin

ACKNOWLEDGMENTS

I would like to express my appreciation to my advisor Dr. A. R. Marder for his continuous patience, support and encouragements during my work at Lehigh. But most importantly I would like to thank him for his trust to me. Thank you and Carole for being with me in most difficult for me and my family times. You also discover for me something that I became proud of.

My gratitude also extends to Mr. J.N. DuPont, for teaching me how to think critically, for his good advise, friendship, and what is most important, for letting me borrow his car. I would like to thank Mr. A. O. Benscoter for teaching me how to use my hands and brain at the same time. Without his help, this work would never been completed.

I have no appropriate words to describe my gratitude for my mom Anna and my dad Felix. Your waited for many, many years to see this moment. Thank you for all the sacrifices that your made. I know it was not easy. Mom, you will be always with me in memories. Without you I would never be where I am now. Thank your for giving me strength and a spark of hope when everything looked hopeless. I would also like thank my brother Vitaly, for his moral support.

I would like to thank Dr. Brian Smith for his technical assistance, guidance, and friendship. Brian, you always raised my spirit when I needed and made my life at

Lehigh a lot of fun. I would also like to acknowledge all the technicians and fellow graduate students: Scott Bluni, Bruce Lindsley, Don Susan, Kevin Stein, Rick Baron, Sean Hayse, Kathy Jordan, Steve Banovic, Saikumar Vivekanand, Mark Thompson, Jay Goodelle, Kathy Repa, and many others who have made this research enjoyable.

I also would like to express my gratitude to Bob and Ruth Lipshutz for unconditional support, help and teaching me what life is all about. My appreciation is also extends to Bob and Eileen Levin-Dando for help and good times that we had. I also thank Roderik, Emily, Rory and Larisa Macfarqvhar for everything that they have done for me. Help and support of Dr. M.R. Notis and J.I. Goldstein is also appreciated. My apologies to those whom I may have inadvertently failed to mention

Funding for this work was provided by US Department of Energy and Air Products and Chemicals Inc to whom I am very thankful.

Finally there only is one thing left to say:

WHAT A COUNTRY!!!

Table of Contents

LIST OF TABLES

LIST OF FIGURES

ABSTRACT

The erosion behavior of weld overlay coatings has been studied. Eleven weld overlay alloys were deposited on 1018 steel substrates using the plasma arc welding process and erosion tested at 400°C at 90° and 30° particle impact angles. The microstructure of each coating was characterized before erosion testing. A relative ranking of the coatings erosion resistance was developed by determining the steady state erosion rates. Ultimet, Inconel-625, and 316L SS coatings showed the best erosion resistance at both impact angles. It was found that weld overlays that exhibit good abrasion resistance did not show good erosion resistance. Erosion tests were also performed for selected wrought materials and their erosion resistances were compared with the weld overlays. Eroded surfaces of the wrought and weld alloys were examined by Scanning Electron Microscopy (SEM). Microhardness tests were performed on the eroded samples below the erosion surface, to determine size of the plastically deformed region. It was found that one group of coatings experienced significant plastic deformation as a result of erosion, while the other did not. It was also established that, in the steady state erosion regime, the size of the plastically deformed region is constant. For coatings that did not have appreciable plastic deformation, an increase in hardness led to an increase in their erosion rates. No correlations were found between hardness and erosion resistance for coatings that deformed plastically. For this group of overlays erosion resistance was correlated to to the the calculated area under the curve of microhardness versus distance from the eroded surface. The possible erosion mechanisms for these coatin groups were analyzed.

I. INTRODUCTION

The erosion of materials by the impact of solid particles has received increasing attention during the past twenty years. Recently, research has been initiated with the event of advanced coal conversion processes in which erosion plays an important role. The resulting damage, termed Solid Particle Erosion (SPE), is of concern primarily because of the significantly increased operating costs which result in material failures. Today SPE damage remains one of the most significant performance problems among U.S. utilities, affecting roughly 80% of fossil fuel systems [1]. According to the industry estimate, SPE alone is costing the utilities at least 150 $ million annually in reduced efficiency, lost power generation, and maintenance of damaged components (boiler tubes and waterwalls) [1]. Reduced power plant efficiency due to solid particle erosion has led to various methods to combat SPE. One method is to apply coatings to the components subjected to erosive environments. Protective weld overlay coatings are particularly advantageous in terms of coating quality. The weld overlay coatings are essentially immune to spallation due to a strong metallurgical bond with the substrate material. By using powder mixtures, multiple alloys can be mixed in weld overlay coating systems in order to achieve the best performance in an erosive environment. Although there has been a large amount of research conducted to understand wear resistance of weld overlay coatings, only a few of them dealt with erosion aspect of wear. The objective of this research was to determine the effects of weld overlay coating composition, microstructure and mechanical properties on their erosion resistance.

II. LITERATURE REVIEW

A literature review of previous work on Solid Particle Erosion was conducted in order to determine possible mechanisms of erosion, identify mechanical properties of materials that control their erosion behavior, and select commercially available weld overlay coatings for erosion protection.

II.A. EROSION MECHANISMS

Erosion is defined by the American Society for Testing and Materials (ANSI/ASTM G40-77) as the progressive loss of original material from a solid surface due to mechanical interaction between the surface and impinging solid particles [2]. Erosion mechanisms may include plastic deformation, chipping, cracking, elastic fracture, and melting. Specific mechanisms depend upon the composition, microstructure and mechanical properties of the material being eroded, composition, size, shape, and density of the eroded particles, their velocity and angle of impact, and the environment temperature [3].

II.A.1. Ductile Materials

Hutchings and Levy [4] used scanning electron microscopy (SEM) to determined the erosion mechanism of ductile metals. It was established that this mechanism shows certain common features, irrespective of the type of the alloy. In all cases, severe plastic deformation occurs in a localized region surrounding the point of particle impact. The observed erosion mechanism can be described in terms of three distinct phases which occur sequentially at any one location. In the initial phase, an

impacting particle forms a crater and material extruded or displaced from the crater forms a raised lip or mound. In the second phase, the displaced metal is deformed by subsequent impacts: this may lead to lateral displacement of the surface material, and can be accompanied by some ductile fracture in heavily strained regions. Finally, after relatively few impacts, the displaced material becomes so severely strained that it is detached from the surface by ductile fracture. This mechanism of erosion in ductile materials has been termed the "platelet" mechanism by Levy et al. [4]. A schematic diagram of this process is shown in Figure 1. It was hypothesized by Sundararranjan [5] that the formation of the extruded lip is facilitated once a critical strain is exceeded in the deformation volume underneath the impacting particle. Evidence of the "platelet" mechanism for erosion of ductile materials has been observed by many uthors [6].

II.A.3. Brittle Materials

The erosion of brittle materials, (i.e. ceramic-type materials) involves brittle fracture, chipping and cracking after particle impact [2]. When a particle strikes the material surface, it may remain undamaged, it may fracture, or deform by plastic flow. Hard particles striking relatively soft targets will tend to produce plastic deformation. However, brittle materials do not deform plastically and therefore, brittle fracture (median and lateral cracking) may occur [7]. It was documented that some materials may exhibit ductile or brittle erosion behavior upon particle impact [7]. This behavior can be explained in terms of the competition between the energy required to produce plastic deformation and the work needed to produce a new crack surface. The

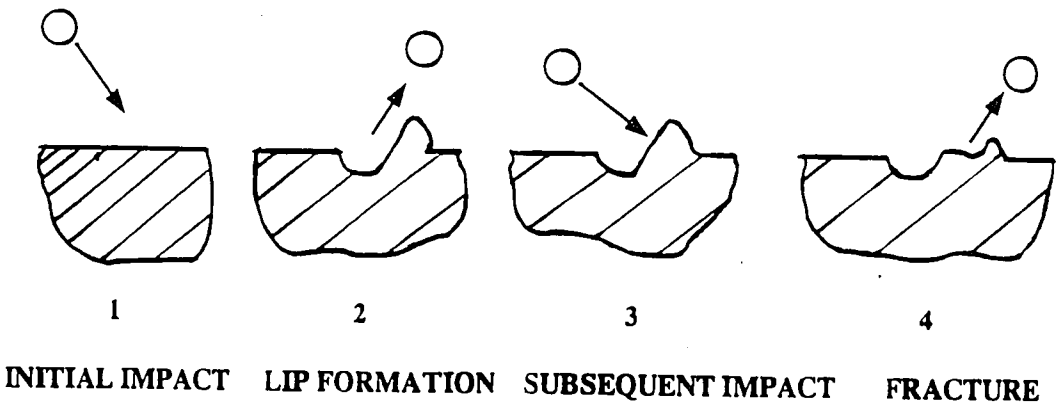

Figure 1. Schematic diagram of material loss during erosion of ductile materials.

occurrence of the transition between plasticity-dominated (ductile) and fracture dominated (brittle) erosion behavior depends upon several interrelated factors. Atkins et al.[8] have shown that such transitions may be controlled by the material parameter given by (ER/σ^2_y), where E is the Young's modulus, R is the specific work of fracture (work per unit area of crack) and σ_y is the flow stress. Since the fracture toughness of a material, K_c, is equivalent to $(ER)^{0.5}$, [9] this material parameter is proportional to fracture toughness. Therefore, the fracture toughness of materials may determine the transition from brittle to ductile behavior during erosion. It was also shown that the ductile to brittle transition depends on erodent particle hardness, density, shape, velocity, and size [7]. It is clear that such a transition is a function of the material's physical and mechanical properties, the erosion conditions and the properties of the erosive particles.

II.A.4. Other Erosion Mechanisms

Several other mechanisms of erosion have been proposed to account for the loss of material. Material removal by melting has been favored by some investigators [11]. A large portion of the kinetic energy of the impacting particles is transformed into heat during plastic work around the impact area. This may lead to a significant temperature rise in this region. Doule et al. [11] suggested that the maximum temperature rise will be determined by the amount of work that is done on the target material, its specific heat, and density. It was calculated that for steel a temperature rise of about 200^0C may be experienced [12] due to the particle impact. The temperature rise was calculated from the following equation [11]:

$$T_{max}=P/(C)x(p), \qquad (1)$$

where P is the indentation hardness, C is the specific heat, and p is the density of the target material. As a result of this temperature rise, the local thermal cycling may assist the formation and propagation of subsurface cracks and therefore, accelerate material loss. It was also established [11,12] that this temperature rise is proportional to the material hardness. Therefore, for materials with low hardness, erosion is not affected significantly by local thermal cycling. Hutchings et. al [13] have indicated that melting is not likely to be an important mechanism in steels. However, there is some evidence that melting may occur in ceramic material [11]. Other mechanisms which have been proposed are associated with the cyclic nature of deformation at the eroded surface. Possible mechanisms involve fatigue or delamination processes. Richman et al. [14] have found that the cavitation erosion rate for different steels and nickel-base alloys is inversely proportional to the their fatigue strength coefficient σ_f. However, there is little definitive evidence in the form of experimental observations to prove this for the case of solid particle erosion.

II.B. THE EFFECT OF MECHANICAL PROPERTIES ON EROSION RESISTANCE

Over the years, many attempts have been made to find a material property or combination of properties that can correlate with the erosion resistance of materials. Such properties include hardness, ductility, strain hardening coefficient, and toughness. However, this literature search revealed that good correlations were obtained only

within narrow classes of materials.

II.B.1. Hardness

In the past, the hardness of a material was thought to be the property that determined erosion resistance. For pure metals, some correlation, between erosion rate and hardness have been shown [2]. The best correlation was found with the hardness of the metal in the fully annealed condition, rather than with the hardness of the metal in a heavily work-hardened condition. The dependence of erosion resistance on hardness for different materials is shown in Figure 2. It can be seen that for metals in the fully annealed condition, an increase in hardness leads to an increase in the erosion resistance. However, several other observations have indicated that the erosion rate is not dependent on material hardness [2]. Levy et. al [15] showed that an increase in the hardness of a steel by microstructural modifications can lead to an increase in erosion rate. For 1075 carbon steel, erosion resistance increases with decreasing hardness for a spheroiditic compared with a perlitic microstructure. Oca et al. [16] have shown that for a series of tool steels, carbon steels, brass, copper, and aluminum, erosion resistance is proportional to the hardness of the surface after erosion.

Recently, Guo et al. [17] documented that the erosion resistance of low chromium white cast irons did not change significantly with a hardness increase when eroded by hard silicon carbide particles. However, when eroded by softer particles (glass sand) the erosion resistance of cast irons significantly increased with an increase in hardness. It was suggested that for a softer erodent, the impacting particles are easily broken and therefore, produce less damage to the surface. Hutchings [7], also proposed that the

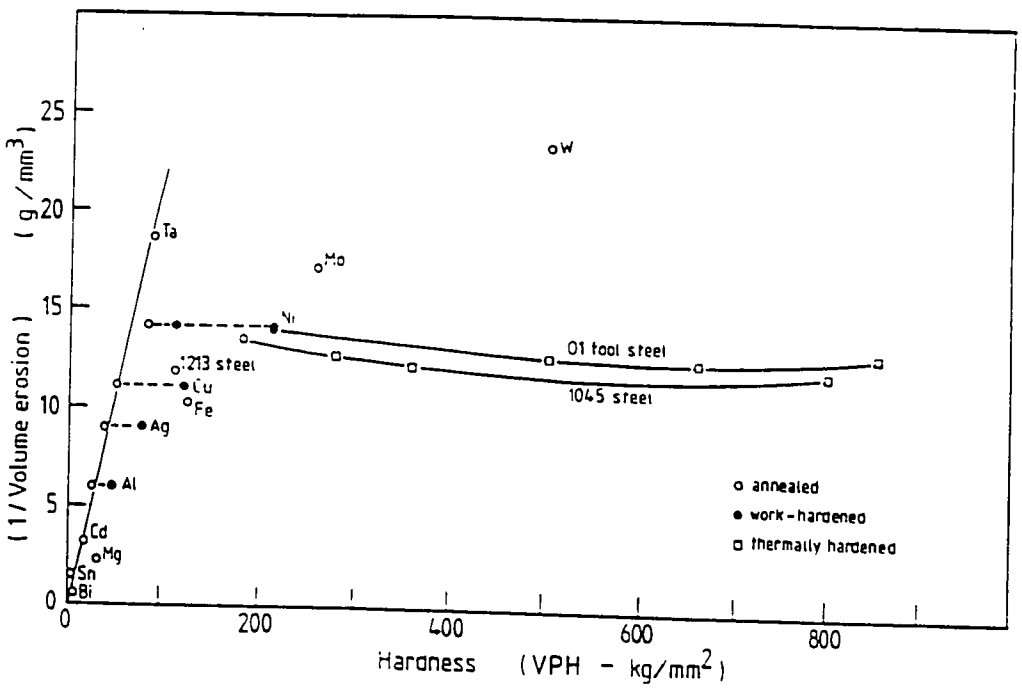

Figure 2. Dependence of erosion resistance (1/volume erosion) on Vickers hardness for several pure metals and steels, and for various states of work-hardening and heat treatment [2].

effect of hardness on erosion resistance is strongly dependent on the properties of the erosive particles (velocity, shape, size, and density). When hard angular particles strike a relatively soft target, the target surface will tend to deform plastically. On the other hand, if the erodent particle hardness decreases, they may distort or even fragment on impact. In this case, erosion damage will decrease as the target hardness increases. This theory is in good agreement with results obtained by Guo et al. [17]. The effect of the eroded particle hardness and target material hardness on erosion resistance of white cast irons is shown in Figure 3 [17]. It can be seen that when eroded by soft glass the sand particle erosion rate decreases with an increase in target hardness. But when eroded by hard silicon carbide particles, the erosion rate increases with an increase in target hardness. It was suggested by Wert et al. [18] that ceramic coatings with high hardness/elastic modulus ratios should have low erosion rates. Also, Ruff et al. [19] have obtained an empirical expression for the erosion of brittle materials. The erosion rate was found to be inversely proportional to the fracture toughness and directly proportional to the indentation hardness according to

$$w=V_0^{2.4}R^{3.7}p^{1.2}K_c^{-1.3}H^{0.11}, \qquad (2)$$

where w is the volume of material removed, V_0 is the impacting particle velocity, p is the particle density, R is the particle radius, K_c is the fracture toughness, and H is the indentation hardness of the eroded material. As discussed above, it is clear that the effect of material hardness on erosion resistance depends on many factors that include its composition, microstructure, erodent properties, and erosion conditions. Thus, the relationship in equation (2) may hold only for a certain group of materials that were

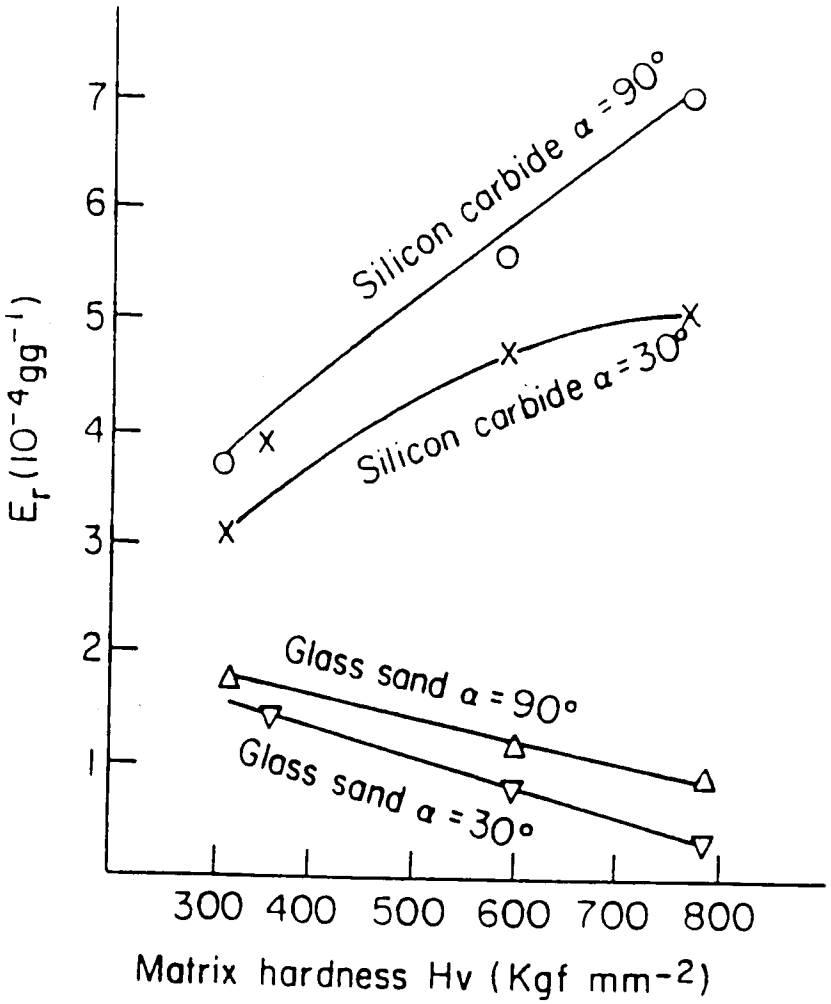

Figure 3. Erosion rate as a function of hardness for low chromium cast iron [17]. Two different erodent were used (silicon carbide and glass sand). α is the particle impact angle, E_r is the erosion rate.

tested in specific erosion conditions.

II.B.2. Strain Hardening

It was suggested by some researches's that material loss from a metal surface due to erosion occurs when a critical fracture strain is achieved at the surface [5]. A critical fracture strain may be achieved locally after single or multiple impacts by the erodend particles. As a result of the particle impact, the material is plastically deformed and the dislocation density increases in the vicinity of the impact. The increase in dislocation density leads to an increase in hardness at the surface. It should be noted that as material is lost at the attainment of the critical strain, the material below the surface is still plastically yielding. A schematic diagram of this process is shown in Figure 4 [20]. Ball [20] proposed that in order to design a material to resist erosion, attention must be given to providing a microstructure which ideally never accumulates the critical fracture strain under the stress that imposed by the impacting particles. Therefore, the ability of a material to accommodate impact energy may contribute to its erosion resistance.

Materials with high strain hardening capacity are able to dissipate impact energy and therefore, the critical strain is accumulated after a much longer time. This effect is illustrated in Figure 5 [20]. In this figure the hypothetical stress-strain curves for the erosive wear of two materials (A and B) are shown. The impacting particles produced a stress that increased from σ_1 to σ_4. As a result of stress increase, the strains (ε) produced in each material are also increased. From this figure it can be seen that material with a higher strain hardening coefficient (material A) require a

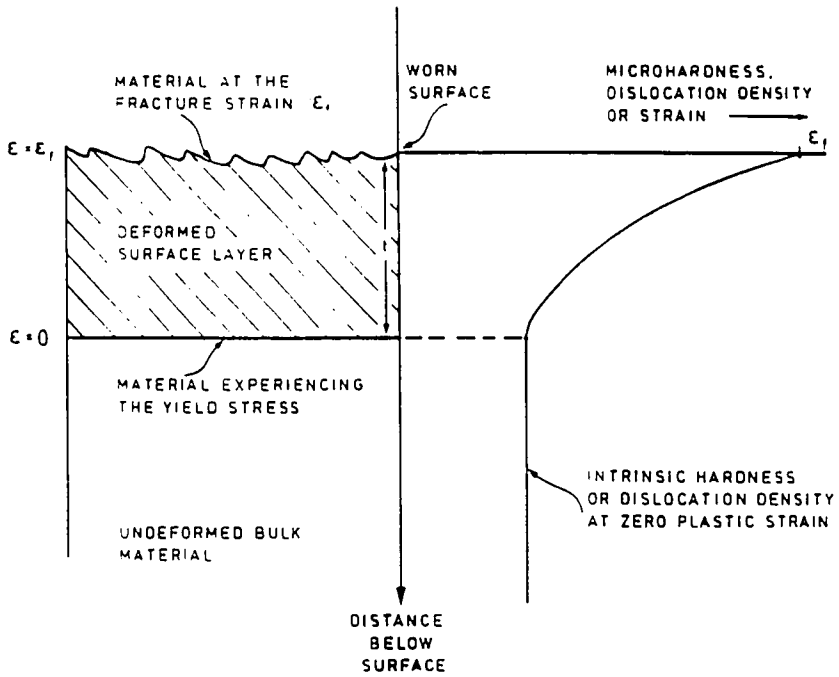

Figure 4. Schematic illustration of the deformed surface layer of an abraded or eroded material. the curve on the right-hand side indicates the change in microhardness, dislocation density or strain with depth below the worn surface [20].

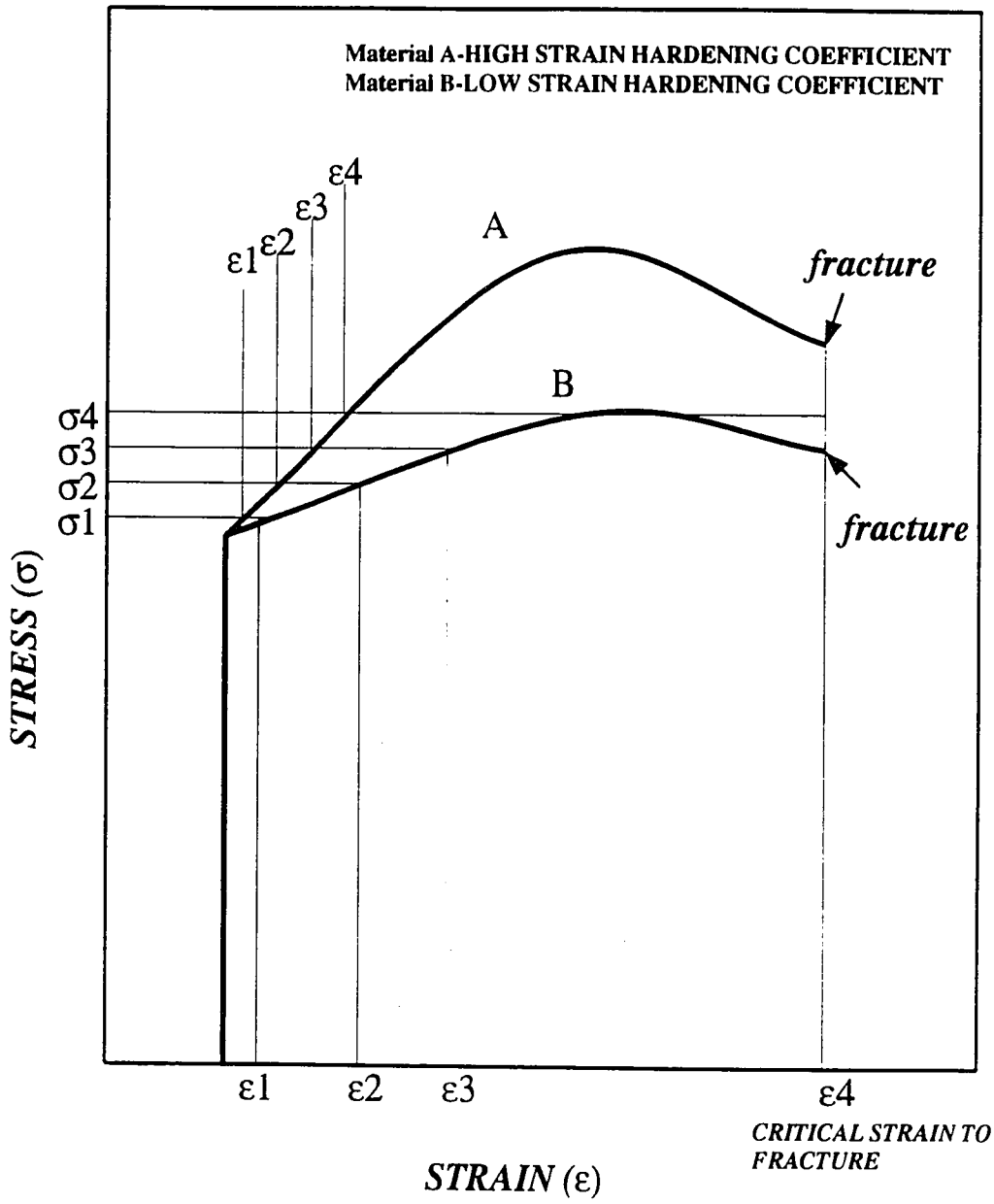

Figure 5. The hypothetical stress-strain curves for the erosive wear of two materials (A and B) having identical yield stresses and strain to fracture. The strains (ε) produced in each material by erosive particles having stress magnitudes from σ_1 to σ_4 are indicated [20].

higher stress to achieve the critical strain to fracture compare with material with low strain hardening coefficient (material B). Gee [21] pointed out that generally metals with face centered cubic (FCC) crystal structures exhibit superior wear resistance compared with base centered cubic (BCC) metals at equivalent hardnesses. This effect was attributed to the higher strain hardening coefficient (n) of the FCC metals. This coefficient (n) appears in the following relationship:

$$\sigma_t = C\varepsilon_t^n, \qquad (3)$$

where, σ_t is the true stress, ε_t is the true strain, and C is a constant.

Venugopal et al. [22] have studied the erosion behavior of Cu-Al, Cu-Zn, and Cu-Si alloys. It was documented that their erosion rates decreased linearly with an increase in the strain hardening coefficient (n). The authors suggested that a higher n values correspond to a higher critical strain that necessary for material removal. As a result of an increase in the critical strain to fracture, the erosion resistance of alloys tested increased. However, Srinvas et al. [23,24] have found that for the series of steels (1040, Cr-Mo and A533 B) with relatively high fraction of second phase particles (i.e. carbides), an increase in strain hardening coefficient leads to a decrease in the critical strain to fracture. It is believed that void nucleation in the materials that consists of a high fraction of second phases particles occurs either by decohesion of the particle/matrix interface or by breaking of the particles when the local stress exceeds a critical value [25]. The higher strain hardening coefficient values enable attainment of the critical stress for decohesion of the particle matrix interface. Therefore, a lower critical strain is required to promote fracture. Also, second phase

particles may disrupt plastic flow during plastic deformation [12]. As a result of this, the critical strain to fracture significantly decreases.

In addition, it was established that the fracture toughness of steels with high volume percent of carbides decreased as the strain hardening coefficient increased [23,25]. However, the strain hardening coefficient may have a different effect on the critical strain to fracture for single phase materials. For example, with commercially pure iron, an increase in the strain hardening coefficient (n) leads to an increase in the critical strain to fracture [24]. In single phase systems fracture nucleation occurs by slip band impingement on grain boundaries or by intersection of slip bands [24]. Therefore, a higher strain is required to initiate fracture. As a result of this effect the fracture toughness of commercially pure iron was found to be proportional to the strain hardening coefficient.

It is clear that the strain hardening coefficient can play an important role in determining the erosion resistance of ductile materials. However, the effect of strain hardening on erosion resistance may vary with the alloy system. With a single phase materials an increase in strain hardening coefficient may lead to an increase in the erosion resistance. However, with a multiphase materials an increase in the strain hardening coefficient may lead to a decrease in the erosion resistance. Only a few metallic systems were studied in order to evaluate the effect of strain hardening on erosion resistance. Moreover, the erosion behavior of brittle materials that do not deform plastically can not be explained based upon strain hardening concept.

II.B.3. Fracture Toughness

The fracture toughness of a material is defined by Hertzburg [9] as a unique stress intensity level that causes fracture. In other words, fracture toughness represents a measure of the amount of energy that a material can absorb before fracture. It is surprising that the effect of fracture toughness on erosion resistance has not received significant attention in the literature since it might contribute to erosion resistance. It was shown previously in this review that fracture toughness is related to the material hardness and strain hardening coefficient. Also, very often ductile or brittle fracture due to erosion is accompanied by subsurface crack initiation and propagation [7]. It is well known that fracture toughness is a primary factor that contributes to the material's resistance to crack initiation and propagation [9]. Therefore, fracture toughness of the target material may contribute significantly to erosion resistance.

The effect of fracture toughness on two body abrasion resistance is shown in Figure 6. It can be seen from this figure that wear resistance initially increases with an increase in fracture toughness. However, when fracture toughness reaches a certain critical value, wear resistance decreases with an increase in fracture toughness. It is also shown that the hardness of the material is decreases as the fracture toughness increases. Hutchings [7] proposed that during abrasion of low fracture toughness materials, brittle fracture is the primary mechanism of abrasion. Therefore, an increase in fracture toughness leads to a decrease in abrasion wear rate. On the other hand, in materials with high fracture toughness, abrasive wear is controlled by plastic deformation and brittle fracture does not occur. In this case the abrasive wear rate is

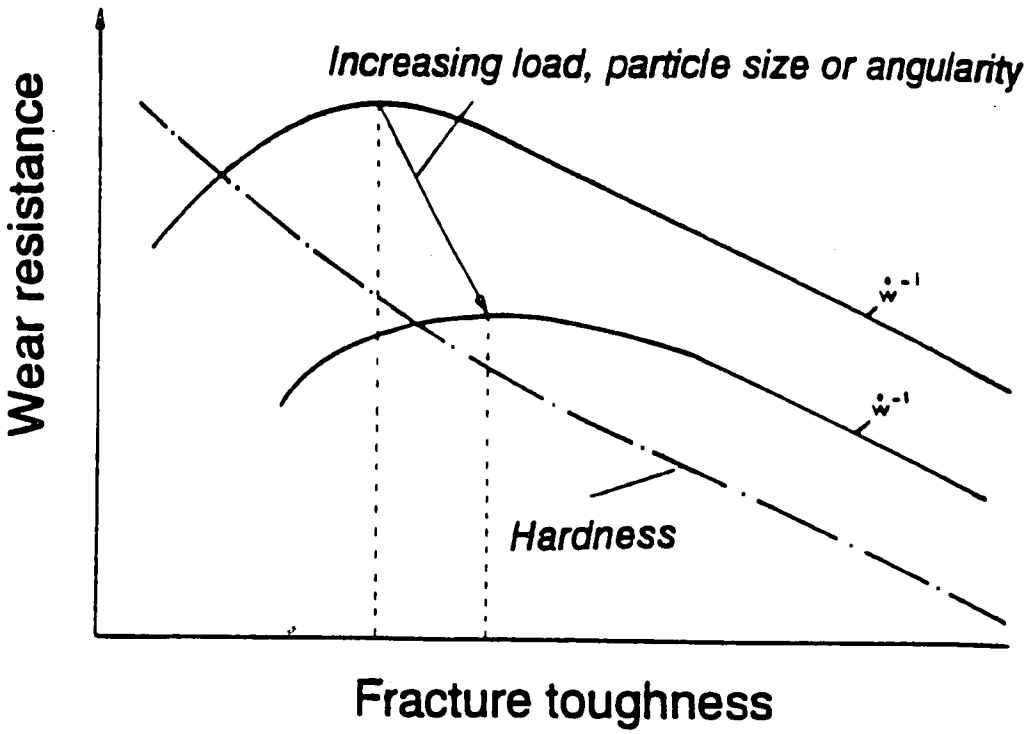

Figure 6. Schematic diagram showing how the abrasive wear resistance depends on fracture toughness. The hardness of materials is also indicated, falling as the fracture toughness increased [7].

controlled by the hardness of the material. Since for most materials an increase in hardness leads to a decrease in fracture toughness, abrasion resistance decreases with increasing fracture toughness at high values of fracture toughness.

Hutchings suggested that the peak in the abrasion resistance-fracture toughness curve (Figure 6) occurs at the point of transition between the two regimes, in which wear is controlled by fracture toughness or hardness. The author also hypothesized that the erosion resistance of materials varies with fracture toughness in the same manner as abrasion resistance. However, there are only a few observations in the form of experimental work to prove this theory for erosion wear. According to Wert et al. [18], the erosion rate of brittle TiB_2 coatings is inversely proportional to fracture toughness. This result has been documented by other workers [19].

It was established by Lawn [26] that fracture toughness of brittle materials is inversely proportional to $(HE)^{0.5}$, where H is the hardness and E is the elastic modulus of the coating. Guo et al. [17] have studied the erosion behavior of brittle low chromium white cast irons. When eroded by hard silicon carbide particles, the erosion rate drastically decreased if fracture toughness increased. The microstructure of low chromium white cast irons consists of a large volume fraction of chromium carbides. The erosion mechanism of these materials may include microcutting, subsurface crack initiation and propagation, spalling, and fragmentation. When eroded by much harder silicon carbide particles, the chromium carbides can not resist cutting or absorb the energy of impact. This leads to crack initiation and crack growth into the matrix. However, if the matrix has a high fracture toughness it can partially absorb the impact

energy and delay crack propagation and fracture, thus leading to lower erosion rate. Several authors have concluded that, when impacted by a harder erodent, materials with a high fracture toughness and hardness offer good protection against erosion [17]. But for a softer erodent, harder target materials are a better choice for erosion protection. Although it can be seen that the fracture toughness can contribute to the erosion resistance of brittle materials, no information was found on its effect on erosion behavior of ductile materials.

II.C. EROSION RESISTANCE OF WELD OVERLAY COATINGS

This literature search revealed a lack of information about weld overlay coating performance in erosive environment (e.g. boiler tubes, waterwalls in power plants). However, it has been established that weld overlay coatings exhibit excellent abrasion resistance [27]. Given the many similarities between erosion and abrasion [28], highly abrasion-resistant materials might be expected to exhibit high erosion resistance. Several different coating groups can be used as weld overlays for erosion protection. They may be separated into four major groups: 1) Cobalt base/carbide type alloys, 2) Nickel base superalloys and Nickel base/boride-type alloys, 3) Iron-base alloys, and 4) Tungsten carbide alloys [27,29].

II.C.1. Cobalt-Base/Carbide Alloys

Cobalt base alloys are extensively used in many industries for components which require high resistance to wear of all kinds [30]. The main difference between the various cobalt base/carbide type alloys is carbon content [27]. It was found that

carbide volume fraction has a significant effect on erosion, abrasion and corrosion resistance of cobalt base alloys [27,31]. Table 1 lists typical compositions of the cobalt base/carbide type alloys. Chromium rich M_7C_3 is the reported predominant carbide in these alloys. Tungsten-rich M_6C carbide was also found in cobalt base alloys that had a high tungsten content. Chromium-rich $M_{23}C_6$ carbide is common in cobalt base alloys that have a low carbon concentration [27]. Photomicrographs of plasma transferred arc deposits of the most widely used cobalt base carbide/type alloys (Stellite-6, 12, and 20) are shown in Figures 7 a,b, and c, It can be seen that tungsten and carbon contents have a strong influence on carbide formation. Both elements increase the volume fraction of carbides [28]. The microstructure of cobalt base/carbide hardfacing alloys consists of primary-solidified hard phases such as M_7C_3 or other type of carbides that were listed above, depending on chemical composition. These carbides are embedded in a eutectic that consists of a metal matrix(Co-Cr-W solid solution) and eutectic hard phases. The structure of the eutectic hard phases consists of carbides (M_6C, M_7C_3, $M_{23}C_6$) and intermetallic compounds [31]. It was documented by Berns et. al. [31] that the hardness of the primary solidified phases in cobalt base alloys was much greater than the hardness of the eutectic. It was also found that coarse primary solidified carbides are responsible for excellent abrasion resistance of cobalt base alloys [27,31].

The eutectic hard phases also significantly contribute to the abrasion resistance of this alloy by covering the areas between primary carbides [27,31]. However, Ninham [32] found that the morphology of the carbides in cobalt base/carbide alloys has a

Table 1. Nominal chemical compositions (wt%) of cobalt-base alloys [27]

ALLOY	B	C	Co	Cr	Fe	Mn	Mo	Ni	Si	W
Stellite 6		1.1	Bal	27.7	3.0	1.0	1.0	3.0	1.1	4.5
Stellite 12	--	1.4	Bal	29.5	3.0	1.0	1.0	3.0	1.4	8.3
Stellite 20	--	2.5	Bal	32.5	3.0	1.0	1.0	3.0	1.0	17.3

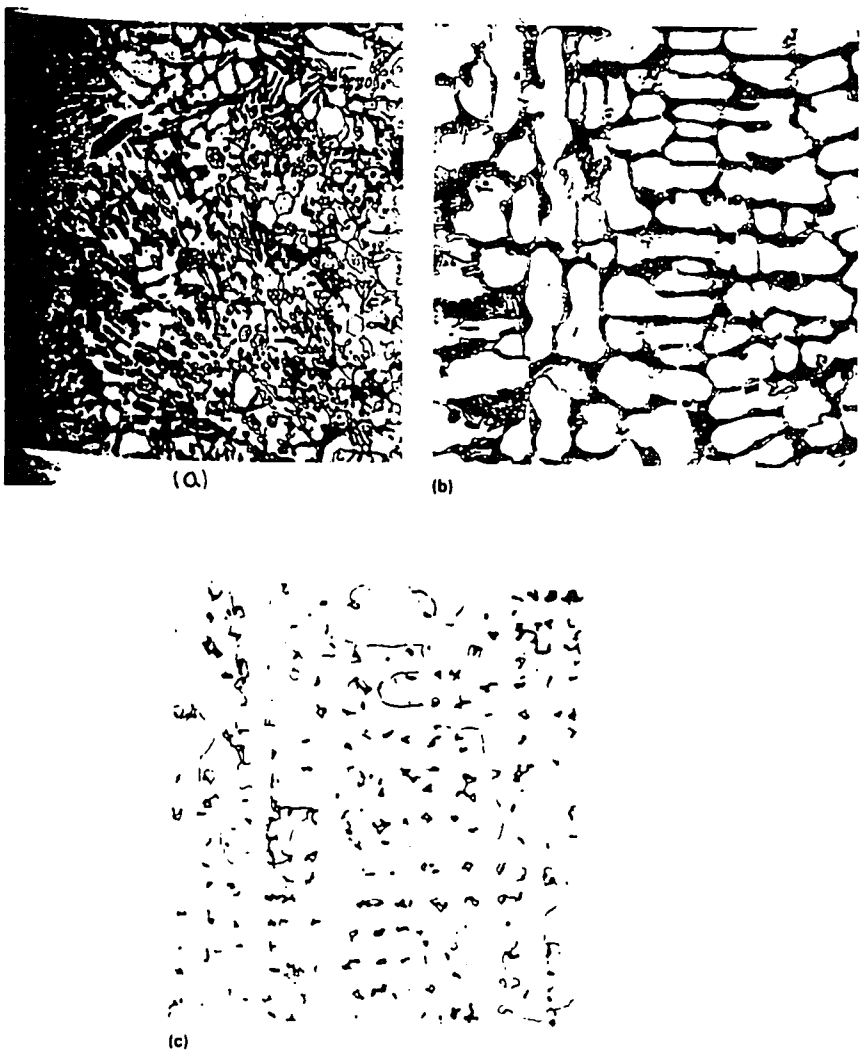

Figure 7. Microstructure of plasma-transferred-arc deposited hardfacing cobalt-base/carbide-type alloys. a) Stellite-20, b) Stellite-12, c) Stellite-6 [27].

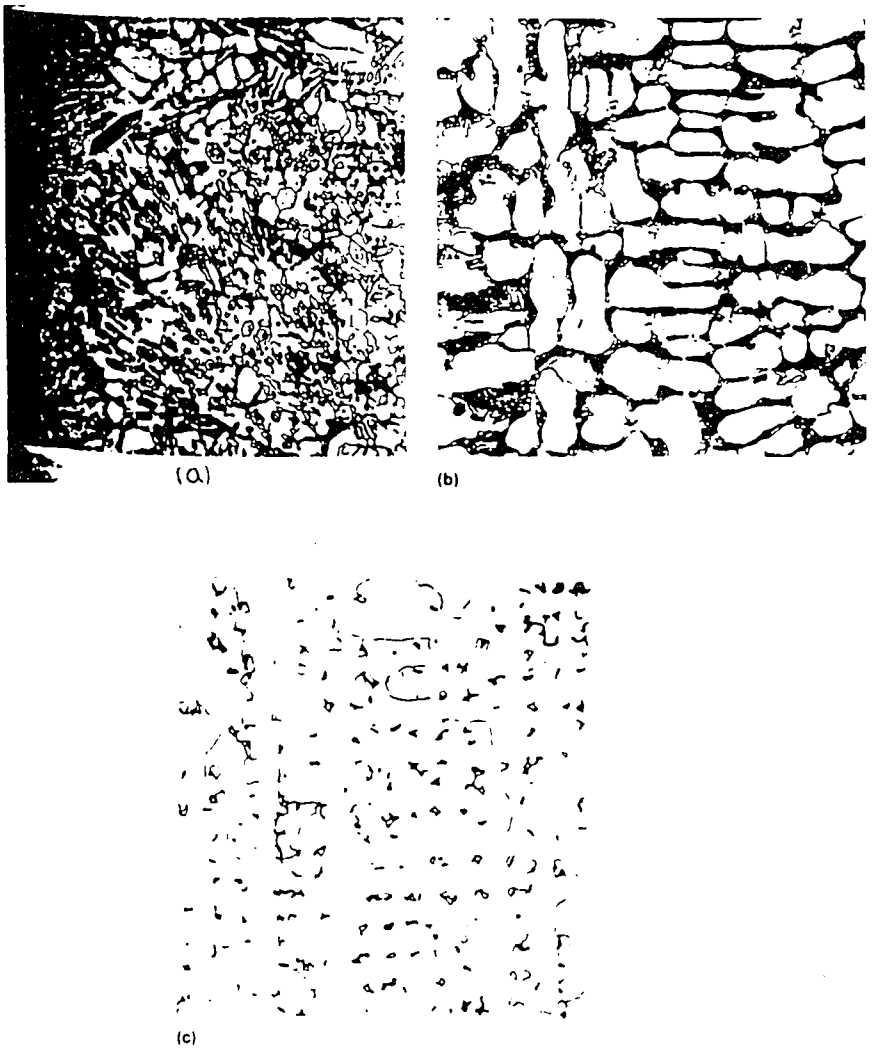

Figure 7. Microstructure of plasma-transferred-arc deposited hardfacing cobalt-base/carbide-type alloys. a) Stellite-20, b) Stellite-12, c) Stellite-6 [27].

much smaller effect on erosion performance than the composition of the matrix. The author also concluded that the hard coarse carbides which provide good abrasion resistance to cobalt base alloys cause a disruption of plastic flow during erosion. It is believed [32] that the inhomogeneous nature of the plastic flow results in very high strain gradients and consequently to void formation and cracking of the carbides. These processes facilitate material removal when the erodent particles strike a surface of the material and increases erosion rate [32]. As it was discussed in section II.B.2., the second phase particles may significantly decrease a critical strain that necessary for material removal. As a result of this effect the material erosion rate is increases. Therefore, hard coarse carbides in cobalt base/carbide alloys may be responsible for high erosion rates. However, it is still unclear how the composition, size and shape of primary and secondary carbides in cobalt base alloys affect erosion rate.

The cobalt base matrix provides excellent strength of the material at high temperature, and chromium additions contribute to corrosion resistance of cobalt base/carbide type alloys [27]. For the past few years, a significant amount of research has been conducted in order to modify cobalt base/carbide alloys by additions of alloying elements that provide better abrasion and erosion resistance [27,30,31]. Berns et.al [31] have found that by alloying additional Nb, Mo, and B the volume fraction of coarse, hard phases is raised. With respect to the base material certain amounts of Ni, W, Si, Cr, B and C that remain after the primary solidification of the hard phases bring fine eutectic phases (carbides, borides, intermetallic phases) together with the metal matrix [30,31]. For example, with addition of niobium in cobalt base alloys,

primary carbide (MC) solidified from the melt an additional intermetallic phases dissolved in Co-Cr matrix [31]. Because of the relatively high cost of cobalt, application of this coating to power plants may not be feasible. Therefore, alternate material should be evaluated, with iron and nickel as potential cobalt substitutes.

II.C.2. Nickel-Base/Boride Alloys

Of all the hardfacing materials, the nickel-base/boride type alloy are microstructuraly the most complex [27]. The typical alloys compositions are shown in Table 2. Together with nickel, the other elements such as chromium, boron and carbon determine the level and type of hard phases within the structure of nickel-base/boride hardfacing alloys upon solidification [27]. The actual phases that form in the nickel base/boride type alloys are listed in Table 3 [27]. The microstructure of a commercial Ni-Cr-B-Si hardfacing alloy is shown in Figure 8 [33]. The alloy microstructure shows initially solidified coarse chromium borides of MB type, which are embedded in a Ni_3B/Ni-eutectic and Ni metal matrix hardened by the dissolved Cr and Si. This alloy has good resistance against abrasive wear and good corrosion resistance [33]. It appears that abrasion resistance of Ni-Cr-B alloys is controlled by the amount of coarse hard phases in the microstructure [33]. This mechanism is very similar to that in cobalt base alloys. It was found that additions of Nb, Mo, W, and Si can increase the volume fraction of hard phases and therefore improve abrasion resistance of these types of alloys [33,35]. Berns et.al. [31] found that for hardfaced alloys the best abrasion wear resistance at a given volume fraction of coarse hard phases occurs in alloys having the lowest amount of metal matrix.

Table 2. Nominal chemical compositions (wt%) of nickel-base/boride-type hardfacing alloys [27].

Alloy	B	C	Co	Cr	Fe	Mn	Mo	Ni	Si	W
Deloro 50	2.4	0.4	--	11.0	3.0	--	--	Bal	4.0	--
Deloro 60	3.1	0.6	--	15.0	4.0	--	--	Bal	4.3	--

Table 3. Phases formed in nickel-base/boride-type hardfacing alloys [27].

Chromium content	Secondary phases formed	Required conditions for secondary phase formation	Dominant hard phase
Low (5 wt%)	Ni_3Si	≥ 3 wt% Si	Ni_3B, complex carbides of $M_{23}C_6$ and M_7C_3 types.
Medium (15 wt%)	Ni_3Si	≥ 2.5 wt% Si	Ni_3B and chromium boride(usually CrB, although Cr_2B and Cr_3B_2 may also be present. Comlex carbides of $M_{23}C_6$ and M_7C_3 types.
High (25 wt%)	Ni_3Si	≥ 3.0 wt% Si	CrB and Cr_5B_3. Complex carbides of $M_{23}C_6$ and M_7C_3 types.

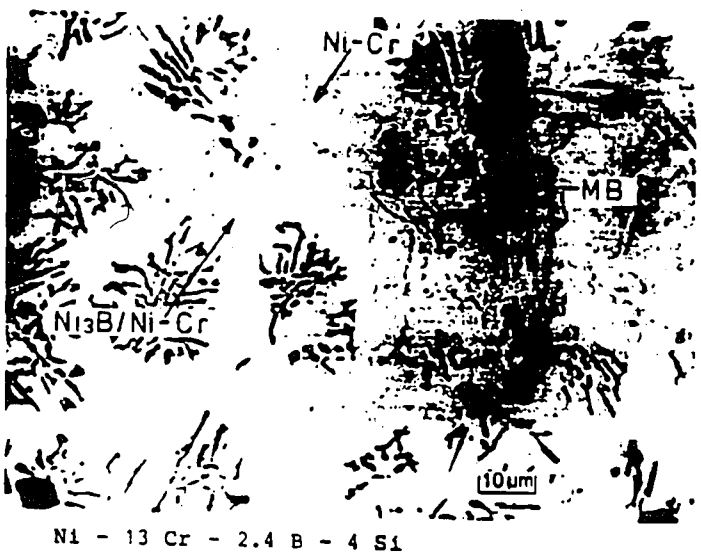

Figure 8. Microstructure of nickel-base/boride hardfacing alloy (13 wt%-Ni, 2.4 wt%-B, 4 wt%-Si) [33].

II.C.3. Nickel-Base Superalloys

Nickel-base superalloys can be defined as alloys that consists of a Ni-Cr matrix, hardened by τ' phase [$Ni_3(Al,Ti)$], with further optional additions of cobalt, iron, tungsten, molybdenum, vanadium, niobium, tantalum, boron, zirconium, carbon, and magnesium [36]. It is well known that nickel-base superalloys are widely used for high temperature applications. Typical compositions of nickel-base superalloys are shown in Table 4 [36]. The carbon concentration in Ni-base superalloys is lower than the carbon concentration in Ni-base/boron alloys. Therefore, one can expect that the amount of carbide phases in Ni-base superalloys is lower than the amount of carbide phases in Ni-base/boride alloys.

Nickel-base superalloys may exhibit high erosion resistance due to their unique hardening mechanism. It was established that Ni-base superalloys have two major microstructural characteristics: 1) Solid-solution hardening of the γ phase matrix and 2) Precipitation of γ' phase, Ni,(Al,Ti) [37]. Tungsten, molybdenum, chromium, and aluminum contribute strongly to solid solution hardening. The precipitation of γ' phase is a phenomenon that differs the Ni-base superalloys from Ni-base/boride alloys. γ' phase is a unique intermetallic phase, the strength of which increases as temperature increases. Moreover, the ductility of γ' phase prevents severe embrittlement of the microstructure. The chemical composition of γ' phase can vary depending upon the amount of alloying elements in the Ni-base superalloys. This literature search revealed no information about resistance of weld overlays nickel base/boride alloys and nickel base superalloys to solid particle erosion.

Table 4. Nominal chemical compositions of nickel-base superalloys [27].

Alloy	Composition, %							
	C	Fe	Ni	Co	Cr	Ti	Mo	Others
Nickel-base alloys								
Astroloy	0.06	...	bal	17.0	15.0	3.5	5.25	4.0Al, 0.03B
Hastelloy C	0.07	5.0	bal	2.5 max	16.0	...	17.0	4.0W
Hastelloy C-276	0.02	5.5	bal	2.5 max	15.5	...	16.0	3.75W, 0.35V
Hastelloy W	0.12 max	5.5	bal	2.5	5.0	...	24.5	0.6 V
Alloy 600	0.1 max	8.0	bal	...	15.5	...	...	...
Alloy 625	0.1 max	5.0 max	bal	1.0 max	21.5	0.4 max	9.0	3.65 Nb + Ta, 0.4 Al max
Alloy X-750	0.04	7.0	bal	...	15.5	2.5		0.95 Nb + Ta, 0.7Al
Nimonic 80	0.10 max	5.0 max	bal	2.0 max	19.5	2.25		1.13Al
René 41	0.09	...	bal	11.0	19.0	3.1	10.0	1.5Al, 0.010 B max
René 95	0.15	...	bal	8.0	14.0	2.5	3.5	3.5Al, 3.5W, 3.5 Nb
TD-Nickel	...	...	bal	...	...	...	...	2ThO_2
U-700	0.15 max	1.0 max	bal	18.5	15.0	3.5	5.2	4.25Al, 0.05B
U-710	0.07	...	bal	15.0	18.0	5.0	3.0	2.5Al, 1.5W, 0.02B
50Cr-50Ni	0.06	...	bal	...	50.0	1.0	...	...
Waspaloy	0.07	...	bal	13.5	19.5	3.0	4.3	1.4Al, 0.07 Zr, 0.006B

II.C.4. Iron-Base Alloys

It is believed that most hardfacing alloys develop their wear resistance by virtue of wear resistance carbides [37]. In iron-base hardfacing alloys intermetallic compounds along with the carbides are responsible for wear protection of the material. The development of iron- base hardfacing alloys is based on two criteria: 1) limited use of strategically important and expensive materials (e.g. cobalt), 2) use of intermetallic compounds as the primary hard phase [37]. A wide range of compositions exist for iron-base hardfacing alloys [38]. Chemical compositions of some of the iron-base hardfacing alloys are shown in Table 5. The lack of information on erosion resistance of these alloys makes material selection very difficult. However, iron-base alloys have a great potential as an erosion resistant weld overlay coating [39]. For example, new Fe-Cr-Ni and Fe-Cr-Ni-Mo alloys have been developed for erosion protection [39]. It was reported that these alloys have a partially amorphous structure that provides unique abrasion and erosion resistance.

Recently, several new high silicon stainless steels have been developed for abrasion protection of bulk materials [27]. The high-silicon hardfacing alloys differ from other hardfacing materials in terms of their corrosion resistance, mechanical properties at high temperature and thermal stability. Silicon is an important matrix element and is a potential promoter of intermetallic precipitates. It has a powerful influence on the wear properties of a material [27]. However, the effect of silicon on erosion resistance of hardfacing alloys has not been determined. Scholl et.al. [37] have found that Fe-Mo-Ni-Si-C hardfacing alloys, which have a microstructure of

Table 5. Nominal chemical compositions (wt%) of Iron-base alloys for hardfacing [27,36]

ALLOYS	C	Co	Cr	Fe	Mn	Mo	Ni	Si
Tristelle-2	2.0	12.0	35.0	Bal.	1.0	--	10.0	4.9
Delcrome-90	2.7	--	27.0	Bal.	1.0	--	1.0	1.0
Delcrome-92	3.7	--	1.5	Bal.	1.0	10.0	2.0	1.0
316 stainless steel	0.1	--	17.0	Bal.	2.0	2.5	12.0	3.5
430 stainless steel	0.1	--	17.0	Bal.	1.0	--	--	1.0
Low alloy steel	0.1	--	0.2	Bal.	1.0	--	--	

austenite/martensite matrix plus austenite/carbide eutectic, showed good abrasion resistance [37]. Apparently, the primary intermetallic compounds and carbides provided high abrasion resistance of this alloy [37]. Cavitation erosion behavior of ordered iron-aluminide alloys has been studied by Johnson et.al. [40]. It was found that Fe-Al alloys exhibited high erosion resistance at room temperature. The high erosion resistance of ordered iron aluminide coating can be attributed to the high strain hardening ability of this alloy [40].

II.D. SUMMARY

Solid particle erosion of waterwall boiler tubes is a failure mechanism that is not fully understood. The erosion resistance of a material is a complex function of the physical and mechanical properties of the target and erodent materials and environmental conditions. There is a wide uncertainty as to what various erosion mechanisms exist, and to what mechanical properties of a material control its erosion behavior. The deposition of weld overlay coatings is one method to combat erosion. However, this literature review revealed that little information exists about weld overlay coating performance in an erosive environment. In order to understand the erosion behavior of these coatings, it is essential to understand the role of mechanical properties, such as hardness, fracture toughness and strain hardening, in determining erosion behavior. The mechanical properties of a coating are a reflection of its microstructure. Therefore, the influence of coatings microstructure on mechanical properties and erosion behavior needs to be determined. It is the goal of this research

to determine effect of weld overlay coatings composition, mechanical properties and microstructure on their erosion behavior.

III. EXPERIMENTAL PROCEDURE

III.A. COATING SELECTION

Eleven weld overlay coatings were selected for erosion testing based upon a literature review and vendors surveys. The nominal chemical composition of the selected coatings is shown in Table 6. All coatings were separated into three major groups: 1)Cobalt-base (or cobalt containing), 2)Nickel-base, and 3)Iron-base alloys.

III.B. COATING DEPOSITION

The plasma transferred arc welding (PTAW) process was employed for coating deposition. Each coating was deposited on a 1018 carbon steel substrate (12 inch x 12 inch x 0.25 inch thick). This substrate was chosen because it is widely used for boiler tube applications in Circulated Fluidized Boilers (CFB's). The 1018 steel surface was prepared to a 24 grit finish and cleaned in acetone prior to welding. Powders of hardfacing alloys were provided by Anval Inc, Stellite Coatings Inc., and Ametec companies.

III.B.1. Welding Laboratory

The welding laboratory consists of a Thermodynamics power source and plasma console unit interfaced to a Texas Instruments/Siemens 405 programmable control unit. Plasma arc welding is conducted with an L-Tec plasma arc torch which delivers fluidized powder alloys directly through the torch into the weld pool. The plasma arc welding process was selected based on its ability to apply a wide range of overlay

Table 6. Nominal chemical composition (wt%) of the selected weld overlay coatings.

WELD OVERLAY	Co	Ni	Fe	Cr	C	Other
COBALT-BASE						
STELLITE-6	62		2.3	28	1.1	4.5%W, 1%Si
TS-2 (TRISTELLE)	11	9	37	35	2.0	4.5%Si
ULTIMET	57	8.8	2.9	24	0.058	2%W, 5%Mo
NICKEL-BASE						
HASTELLOY-22	--	57.1	5.1	21	0.006	2.9%W, 13%Mo
INCONEL-625	--	62	--	21	0.023	3.5(Nb+ Ta), 8.5%Mo
B-60	--	73	4	13	0.67	2.8%B, 4.2%Si
IRON-BASE						
ARMACOR-M	--	--	39	49	--	8%B, 3%Si
IRON-ALUMINIDE	--	--	84	2	--	14%Al
HIGH Cr IRON	--	0.3	68	27	2.7	0.4%Mn 0.6%Si
316L SS	--	10	69	16	0.03	2%Mo, 1.5%Mn
420 SS	--	--	85	13	0.4	0.4%Si 0.3%Mn

alloys in powder form. Photographs of the welding laboratory are shown in Figures 9 and 10. A schematic of the Plasma ARC Welding unit is shown in Figure 11. With this process, the heat required for welding is generated by an arc which is maintained between a non-consumable tungsten electrode and the base metal. The tungsten electrode in the PAW torch is recessed within the gas nozzle and two gases are used. An argon orifice gas flows at high velocity through the orifice body and forces the arc to form a cylindrical shape. An auxiliary argon shielding gas protects the weld metal from atmospheric gases. The intensity of the heat source is controlled primarily by adjusting the current that flows through the arc. Also, the recessed tungsten electrode permits the use of powder filler metals which can be transported directly through the torch. The welding parameters such as voltage, travel speed, current, and filler metal feed rate were optimized in order to provide good fusion between coating and substrate.

III.B.2. Welding Process Parameters

The welding process parameters that were used for coating deposition and the resultant coating thicknesses are listed in Table 7. The heat generated per unit length of weld (H) was calculated by using the following equation: $H= \alpha VI/S$, where V is the voltage drop across the arc, I is the welding current, S is the travel speed of the arc and α is an arc efficiency factor [42]. To accurately determine the heat input to the material the arc efficiency factor must be known. The arc efficiency factor is given as α = Energy Transferred into Work Piece/Energy Generated by Arc [42], α is always less than unity and the arc efficiency is mainly a function of the type of

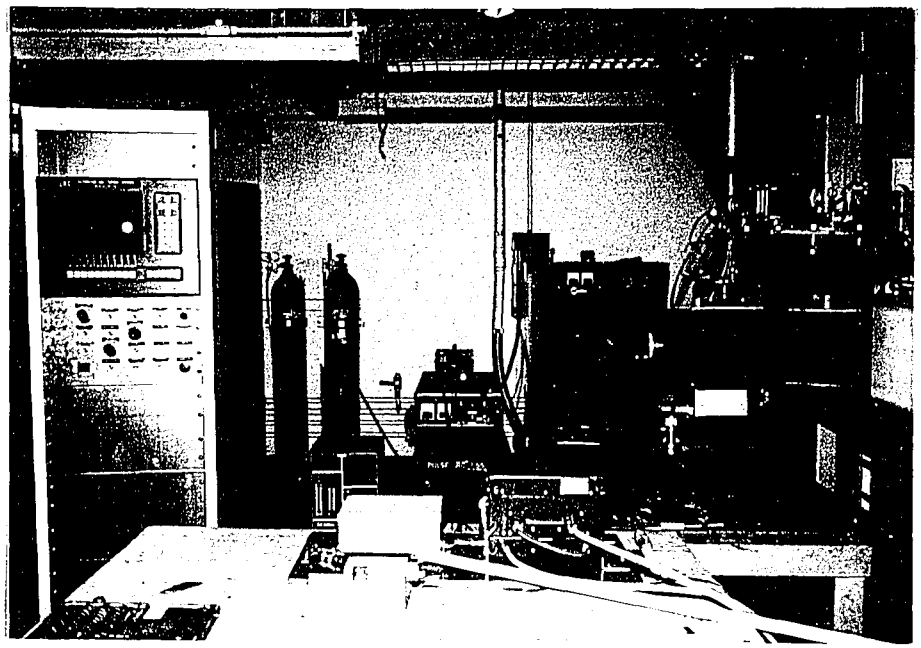

Figure 9. Overall view of the welding laboratory

Figure 10. A photograph of the plasma arc torch assembly

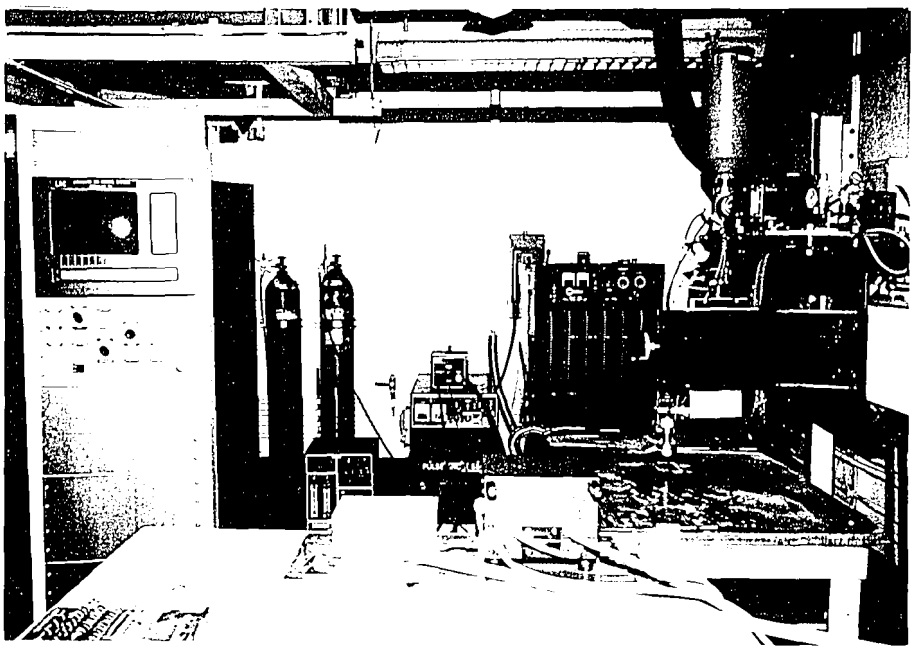

Figure 9. Overall view of the welding laboratory

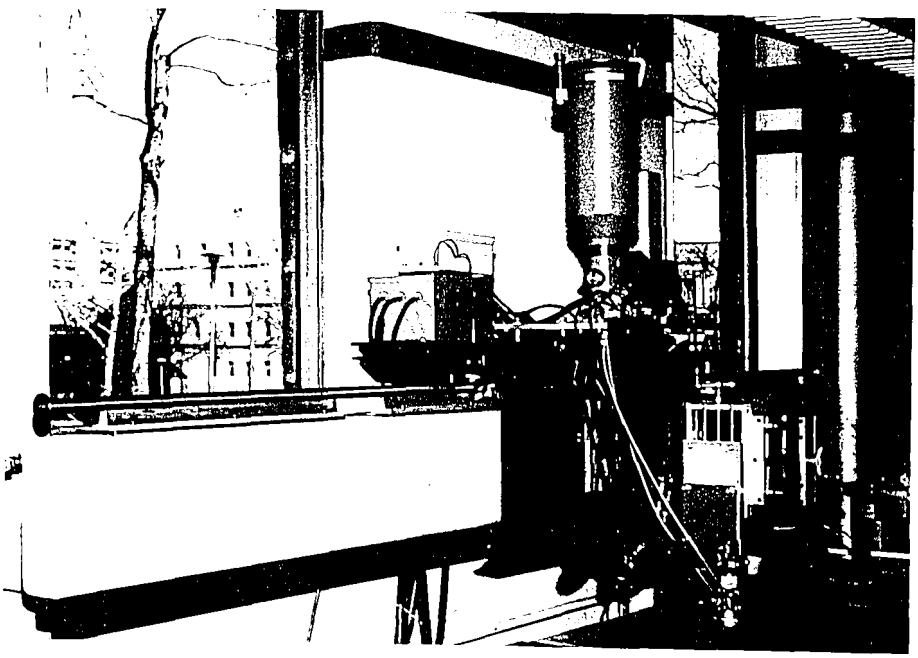

Figure 10. A photograph of the plasma arc torch assembly

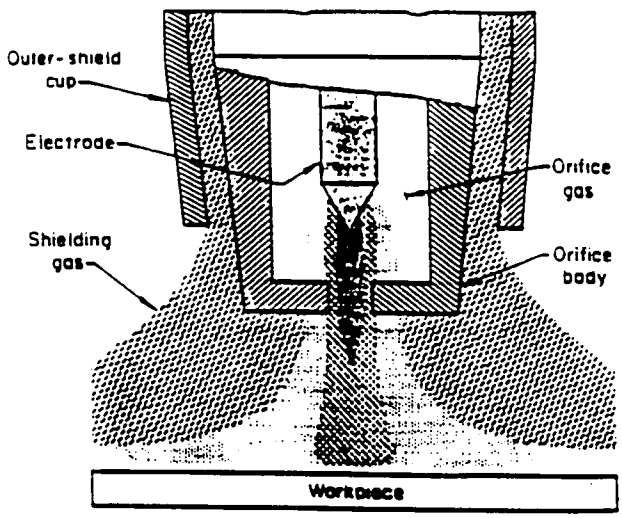

Figure 11. A schematic diagram of the plasma arc welding unit.

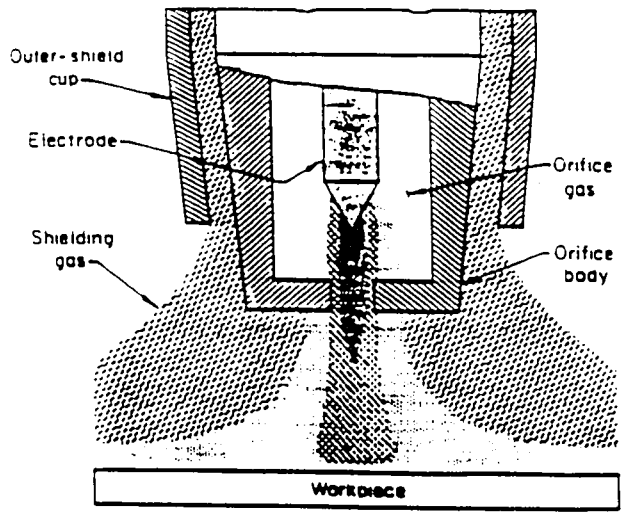

Figure 11. A schematic diagram of the plasma arc welding unit.

Table 7. Process parameters for deposition of hardfacing weld overlays alloys. Plasma transferred arc process.

Hardfacing Weld Overlay Coating	Coating thickness mm	Heat input J/mm	Powder feed rate cm^3/sec	Interpass temperature C°
STELLITE-6	3.3	1272	3.0	<60
TRISTELLE TS-2	4.2	1272	3.0	<60
ULTIMET	3.4	1296	3.0	<60
HASTELLOY 22	1.8	695	3.5	<60
B-60	4.0	787	3.5	<60
INCONEL 625	3.5	1056	3.5	<60
ARMACOR	2.4	777	4.0	<60
IRON ALUMINIDE	3.3	1272	3.0	<60
HIGH CHROMIUN IRON	3.5	912	4.0	<60
316L SS STAINLESS STEEL	4.3	1131	3.5	<60
420 SS STAINLESS STEEL	4.6	1131	3.5	<60

Plasma Gas Flow Rate-5 SCFH (argon)
Shielding Gas Flow Rate-30 SCFH (argon)
Powder Gas Flow Rate-10 SCFH (argon)
These parameters were kept constant for all materials.

welding process. The arc efficiency factor for plasma transferred arc welding was experimentally determined to be 0.48 from previous work at Lehigh [43].

Each coating sample contains 10 to 15 single weld beads which overlap by approximately 50 percent. This value of overlap is typical in surfacing applications because it provides low dilution in the coating and a smooth coating surface. Dilution is given by the following equation [42] (see Figure 12):

$$\% \text{ Dilution} = A_s/(A_s+A_o) \text{ X } 100$$

The dilution is a measure of the amount of base metal that mixes with the weld overlay. Because of dilution, the final chemical composition of the alloying elements in the weld overlay coating will be less than the initial composition of the powder. Therefore, dilution can significantly affect coating composition. On completion of the welding of each layer, the test piece was allowed to cool in air to room temperature.

III.C. SAMPLE PREPARATION

III.C.1. Sectioning and Mounting

After deposition, weld overlays were sectioned with an abrasive (Al_2O_3) cut off wheel into 0.5 inch x 0.5 inch coupons for erosion tests. The first three and the last welding beads were not included in the samples for erosion tests due to the high dilution level in these beads. Two uneroded samples from each coating (longitudinal and transverse locations) were cross-sectioned and mounted in cold curing, thermosetting epoxy. This material cures at room temperature without an externally applied pressure. The lack of applied mounting pressure prevents any damage to the

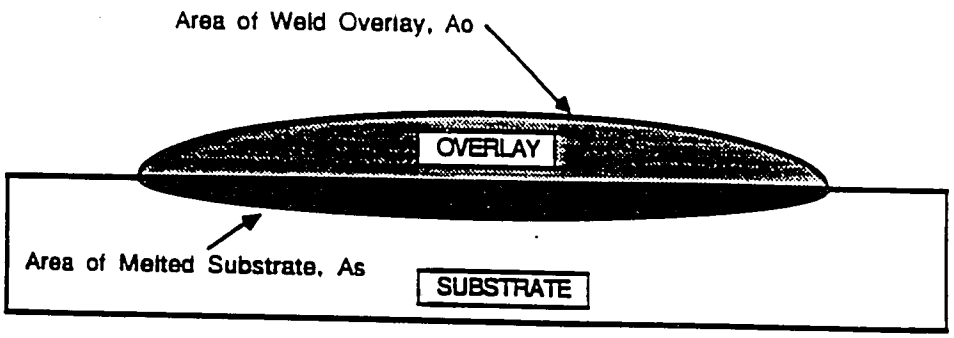

Figure 12. A schematic illustration of the cross-section of the weld overlay describing dilution. dilution is defined as the ratio of the melted substrate area (A_s) to the total melted cross-sectional area (A_0+A_s).

coating surface. Longtudinal and transverse samples were placed in the same mount. In this way, the two coated surfaces provide support for each other.

III.C.2. Metallography

The weld overlay coating samples were ground on an automatic polisher to a 600 finish using silicon carbide paper. Final polishing was performed to a 0.3 micron finish using alumina powder. The polishing steps removed the surface scratches and deformation that were incurred during the final grinding step. The specimens were etched and their microstructure was characterized by using Light Optical Microscopy (LOM).

III.D. MICROSCOPY

The microstructure of all the coatings in the as-weld condition was characterized using Light Optical Microscopy (LOM). LOM was performed using a Zeiss Axiomat Inverted Light Microscope. In addition, eroded surfaces of each coating after 100 min exposure (longest time) were observed by Scanning Electron Microscopy (SEM). SEM analysis was performed using an ETEC Autoscan Electron Microscope operated at 10 and 20 KV. Observation of the eroded surface using SEM required the application of a thin amorphous carbon coating to each specimen. A Denton Vacuum carbon evaporator was used to apply the carbon coating to the eroded surfaces. Also, carbon tape was applied on the sides of each sample and from the edge down to the stub. These two specimen preparation techniques were necessary to prevent imaging problems associated with specimen charge collection.

III.E. EROSION TESTS

III.E.1. Erosion Tester

A schematic diagram of the erosion tester that was used in this investigation is shown in Figure 13. The system is driven by an air compressor which can deliver up to 35 scfm of air. The air is cleaned through a series of fibers to remove any entrained water. The flow meter and pressure regulator control the amount of air that flow through the system. The air is heated by two inline fluid heaters to temperatures up to 700°C exiting the heaters. Erodent is fed into the air stream with a screw feeder to ensure constant feed rates. The particles and hot air are accelerated and impinge upon the sample at any angle between 0° and 90°. The particles velocity distribution prior to impact is directly measured with a Laser Doppler Velocometer (LDV).

III.E.2. Erosion Tests Conditions

The standard test conditions that were chosen for this study were:

Eroded Sample Planar Dimensions = 0.5 inch x 0.5 inch

Sample Temperature = 400°C

Erodent Particles Velocity = 40 m/s ± 5%

Erodent Particles Flux = 8.56 mg/(mm^2/sec)

Impingement Angle = 90° and 30°

Erodent = alumina (Al_2O_3)

Erodent size = 300 microns

Exposure time = 5, 10, 20, 50, and 100 min

The sample size was chosen to be 0.5 inch x 0.5 inch because these dimensions

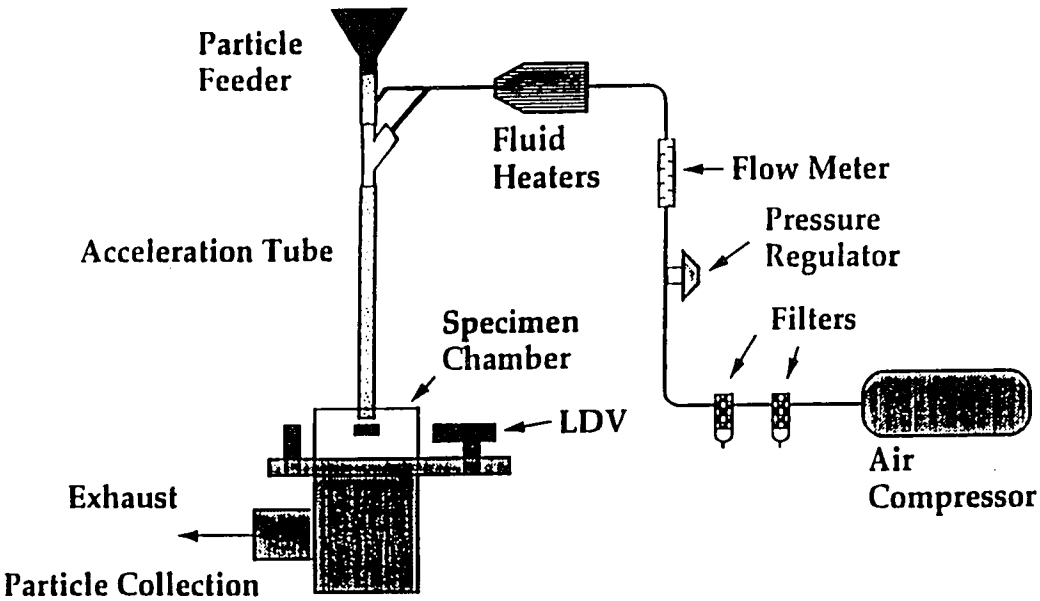

Figure 13. A schematic diagram of the erosion tester.

are slightly smaller than the acceleration tube inner diameter (0.6 inch). Therefore, the top surface of the coatings are completely covered by the erodent particle stream. An example of a typical erosion sample is shown in Figure 14.

The sample temperature was chosen to be 400°C, similar to the temperature of the fireside boiler tube surface [44]. The particle velocity is simmilar to this used by other investigators [45]. The erodent particle velocity is reported as an average velocity and the standard deviation was found to be approximately 5%.

The particle impingement angles were chosen to be 90° and 30°. The impingement angle is defined as the angle between the direction of the impinging particles and the metal surface at the point of impact [2]. From the literature review, it was found that some ductile materials exhibited a maximum erosion rate at 20-30° impact angles [2] while several brittle materials exhibited maximum rates at a 90° impact angle. Based upon these results it was decided to conduct erosion tests at these two impingement angles in order to evaluate potential variations in erosion rates between classes of overlays (i.e. ductile vs. brittle) due to differences in impact angle. For many materials it was found that erosion rate is independent of erodent particle size for particles larger than about 100 to 200 um in diameter [2]. Therefore, erodent particle size was chosen to be 300 um.

III.E.3. Steady State Erosion Rate Determination

The erosion kinetics which are typical of most materials are schematically shown in Figure 15. The weight loss of a given material as a function of time during erosion often follows a pattern consisting of a relatively small incubation period with little or

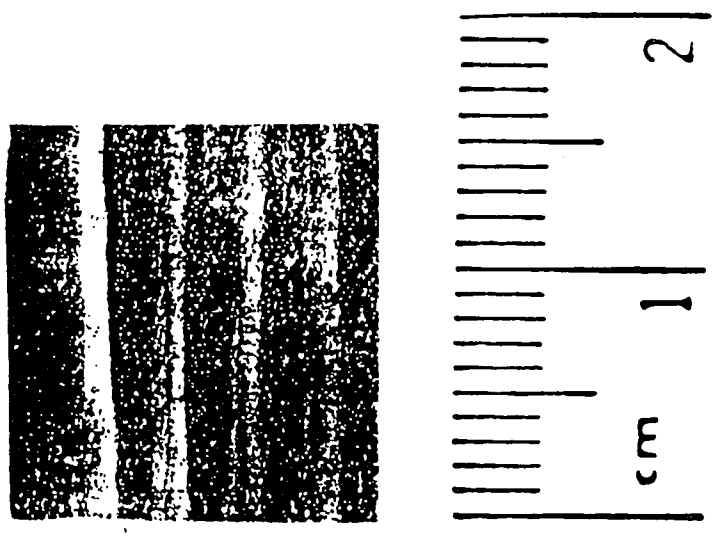

Figure 14. Top view of the typical erosion sample.

no material removal. Apparently, incubation periods are indicative of the time required for sufficient work hardening prior to localized fracture [46]. The material eventually experiences surface weight loss and surface hardening at the same rates, and attains a steady state erosion rate. Steady state erosion is defined by the linear portion of the weight loss versus erosion time graph [2]. Determination of the steady state erosion rate is very important from a practical point of view since most of the material removal occurs during this period. Five different erosion exposure times (5, 10, 20, 50, and 100 min.) were used in this study in order to adequately obtain the weight loss vs. erosion time plot for each weld overlay coating. For some coatings, additional 80 min and 120 min tests were conducted. One sample was used per each erosion time. Therefore, five or six samples from each coating were used in order to obtain the relationship between weight loss and erosion exposure time for each impingement angle.

To quantify weight loss during the erosion experiments, the erosion coupons were ultrasonically cleaned in acetone and weighed before the erosion tests to the nearest 0.1 mg. The samples were handled with plastic tweezers to avoid contamination and stored in wax paper envelopes until testing. Once the erosion tests were complete, the samples were again ultrasonically cleaned in acetone and weighed to determine the weight change due to erosion. The graphs of weight loss vs. time of exposure were obtained for each weld overlay coating for each impingement angle. A linear regression analysis was performed on the data in the steady state erosion regime of the weight loss versus erosion time plots, the slopes of which yield the steady state

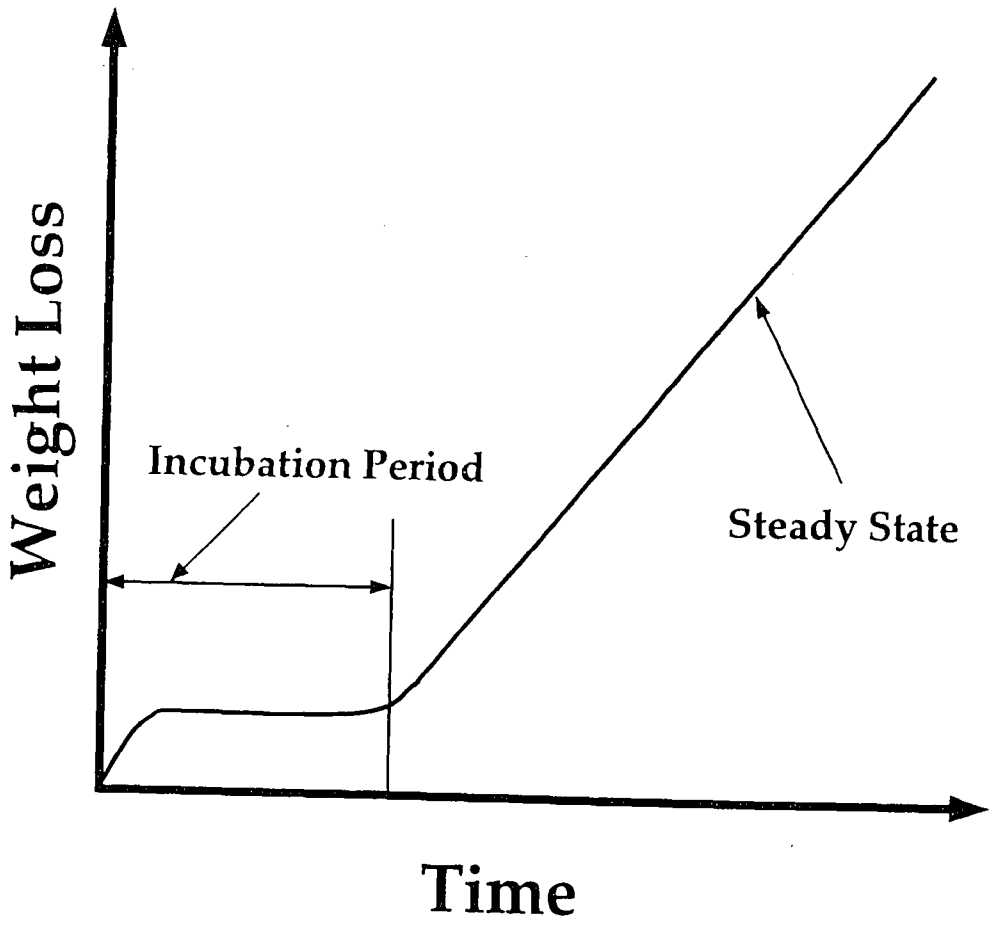

Figure 15. A schematic diagram of the erosion kinetics.

erosion rate. The volume erosion rate for each coating was obtained by dividing weight loss rate to the density of the coating. The volume erosion rate is a more objective parameter that measure material loss due to erosion than the weight loss rate. For example, two materials with different densities may exhibit equal weight loss due to erosion, however, high density material will have a lower volume loss than a material with low density, since V=m/p, where V is the volume of the removed material, m is the weight of the removed material, and p is its density.

III.F. MICROHARDNESS MEASUREMENTS

III.F.1. Room Temperature Microhardness Profiles

The room temperature microhardness tests were performed on all weld overlays in order to determine variations in weld hardness with distance from the top of the weld. All tests were conducted on the longitudinal sections of uneroded welds by using a LECO-M 400 FT Microhardness Tester interfaced with computing processor ACP-94. A highly polished, pointed rhombic-based, pyramidal diamond with included longitudinal edge angles of 172° and 130° was used as an indenter (Knoop indenter). The Knoop indenter produces a rhombic-shaped indentation that has a ratio between long and short diagonals of approximately 7 to 1 [47]. Due to its elongated shape, the use of a Knoop indenter enabled indentations to be made closer to the edge of the sample and adjacent indentations compared with a Vickers indenter. Therefore, variations of microhardness of the weld as a function of the distance from the top of the weld can be measured more accurately. The microhardness tests were conducted

according to ASTM E 384 standard [48]. The schematic diagram of the microhardness test is shown in Figure 16. All tested samples were cross-sectioned, mounted and polished according to the procedure previously described in Sections III.C.1. and III.C.2. The microhardness tests started at the top of the weld and proceeded well into the base metal. The long diagonals of the indentations were oriented parallel to surface of the weld. The spacing between each indentation was 120 microns. A 1 kg load was used to obtain microhardness measurements. The length of the long diagonal for each indentation was measured and the Knoop hardness number was determined by computer processor ACP-94.

III.F.2. Plastic Deformation Measurements

In order to determine the size of the deformed region beneath the eroded surface, microhardness tests were performed on a longitudinal section of each weld overlay coating after 100 min exposure in the erosion tester at 90° particle impact angles. As a result of the erosion, the material beneath the eroded surface may experience plastic deformation and coating hardness may increase directly below the surface. A plastic zone size and an increase coating hardness due to erosion can be estimated by obtaining a microhardness profile from the eroded surface into the base material. A schematic diagram of this profile is shown in Figure 17. The depth at which the hardness value becomes constant is defined as the plastic zone size. The same experimental procedure was used for these tests as for the microhardness measurements on uneroded samples (section III.F.1.). However, small applied loads (10 g, 25g, 50g and 100g) were used. Application of small loads decreases the

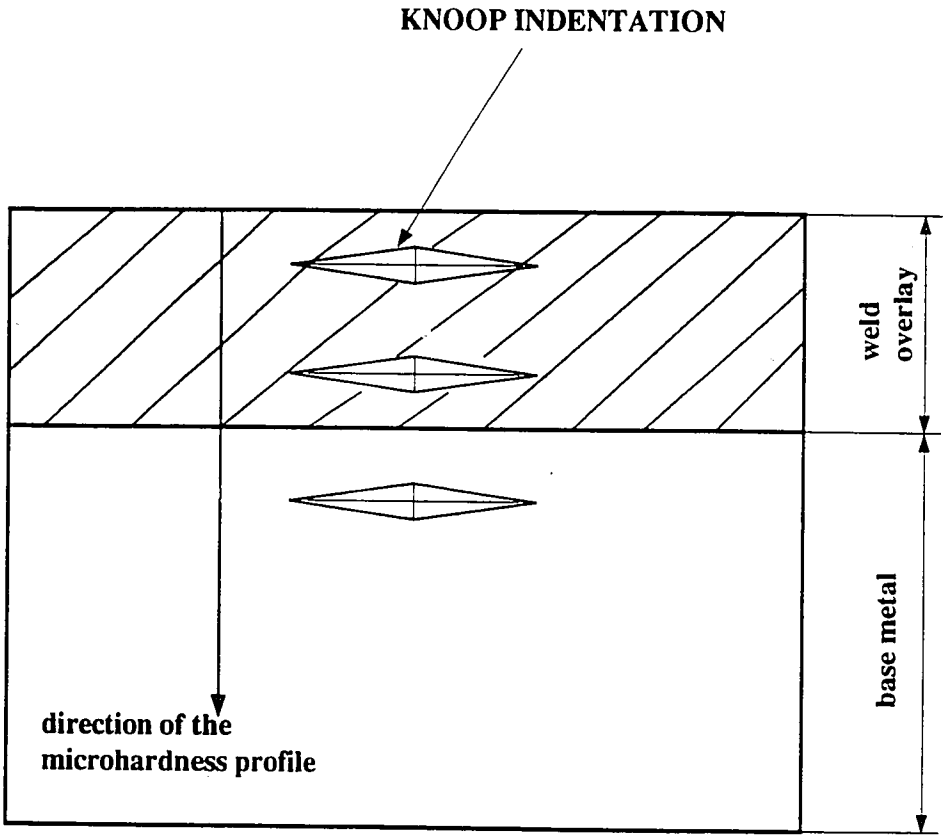

Figure 16. A schematic diagram of the microhardness test performed on the weld overlay coating cross-section.

indentation size and spacing between each indentation can be significantly decreased as a result. With this approach, even small variations in hardness with distance from the eroded surface can be detected. Measurements were made at the distance of 10 or 20 um from the eroded surface, depending upon the applied load and proceeded well into the weld. The microhardness tests were conducted according to ASTM E 384 standard [48]. Three to five microhardness profiles were obtained in different locations of each coating in order to improve the statistical significance of the data. From these profiles, the size of the plastic zone and increase in coating hardness due to erosion for each coating was determined.

III.F.3. High Temperature Microhardness Measurements

High temeparture hardness tests were conducted in order to determine the effect of coating hardness on their erosion resistance at elevated temperature (400°C). The tests were performed on a Nicon Microhardness Tester. The measurements were obtained on a longitudinal section of each weld overlay. The required sample size for these tests is 10 mm x 5mm x 5mm thick. Before testing, each sample was mechanically polished to 0.3 um surface finish. Hot-hardness tests were made with a 500 g load using a pointed square-base pyramidal diamond with face angles of 136°±30 min (Vickers indenter) at a constant dwell time (5 sec) at maximum load. The Vickers indenter produces a square-base indentation. Measurements were taken at 25°C and 400°C under 1 mPa (10^{-5} torr) pressure. The microhardness tests were conducted according to ASTM E 384 standard [48]. Both diagonals of each impression were measured and their mean value was used as a basis for calculation of

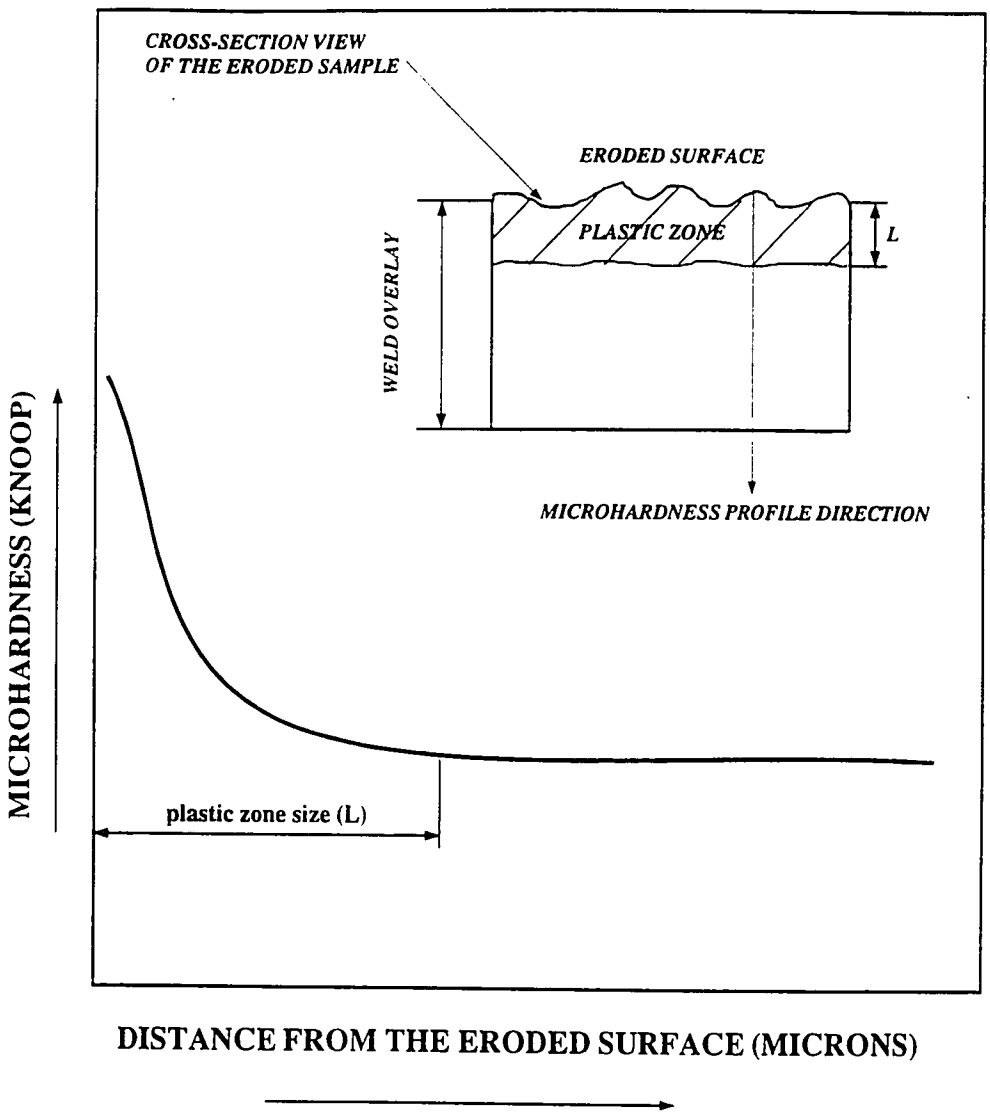

Figure 17. A schematic diagram of the microhardness profile that was taken in order to estimate plastic zone size due to erosion.

the Vickers hardness number. In order to calculate the Vickers hardness number the following expression was used [47]:

$$HV=1.8544P/d^2,$$

where HV is the Vickers hardness number, P is the applied load in kilograms, and d is the mean diagonal of the indentation in millimeters. Average microhardness numbers and standard deviations were calculated from at least ten to twenty indentations. It should be noted that indentations were made at different locations on each coating sample and therefore, variations in microstructure throughout the weld could contribute to the error in microhardness measurements.

IV. RESULTS

IV.A. MICROSTRUCTURAL CHARACTERIZATION

The microstructures of all the coatings in the as-welded condition were characterized using LOM. The mictrostructures of the welds are shown in Figures 18-28. Inspection of the photomicrographs shows that most of the coatings (Stellite-6, Ultimet, Inconel-625, Hastelloy-22, B-60, High Cr Iron, 316L SS, and 420 SS) exhibited dendritic microstructures that are typical for weld materials. The microstructures of all the coatings are inhomogeneous due to the non equilibrium solidification conditions which occur during welding. Particular features of each coating class are noted below.

IV.A.1. Cobalt-Base/or Containing Coatings

Figure 18-20 shows photomicrographs of the cobalt-base weld overlay coatings. Other work has reported that for Stellite-6 weld overlay coatings (Figure 18), the primary dendrites (white phase) are a cobalt-rich face-centered structure while the interdendritic eutectic regions (mixed dark and white phase) contain hard M_7C_3 carbides [28,33]. The stoichiometric compositions of the carbides were determined by the X-ray diffraction technique [28,33]. It has been indicated that these hard phases within the eutectic in the Stellite-6 significantly contribute to abrasion resistance [28].

The microstructures of the TS-2 and Ultimet weld overlay coatings are shown in Figure 19 and 20, respectively. The coating microstructures consists of second phase particles (dark features) and metal matrix (white regions). The second phase particles

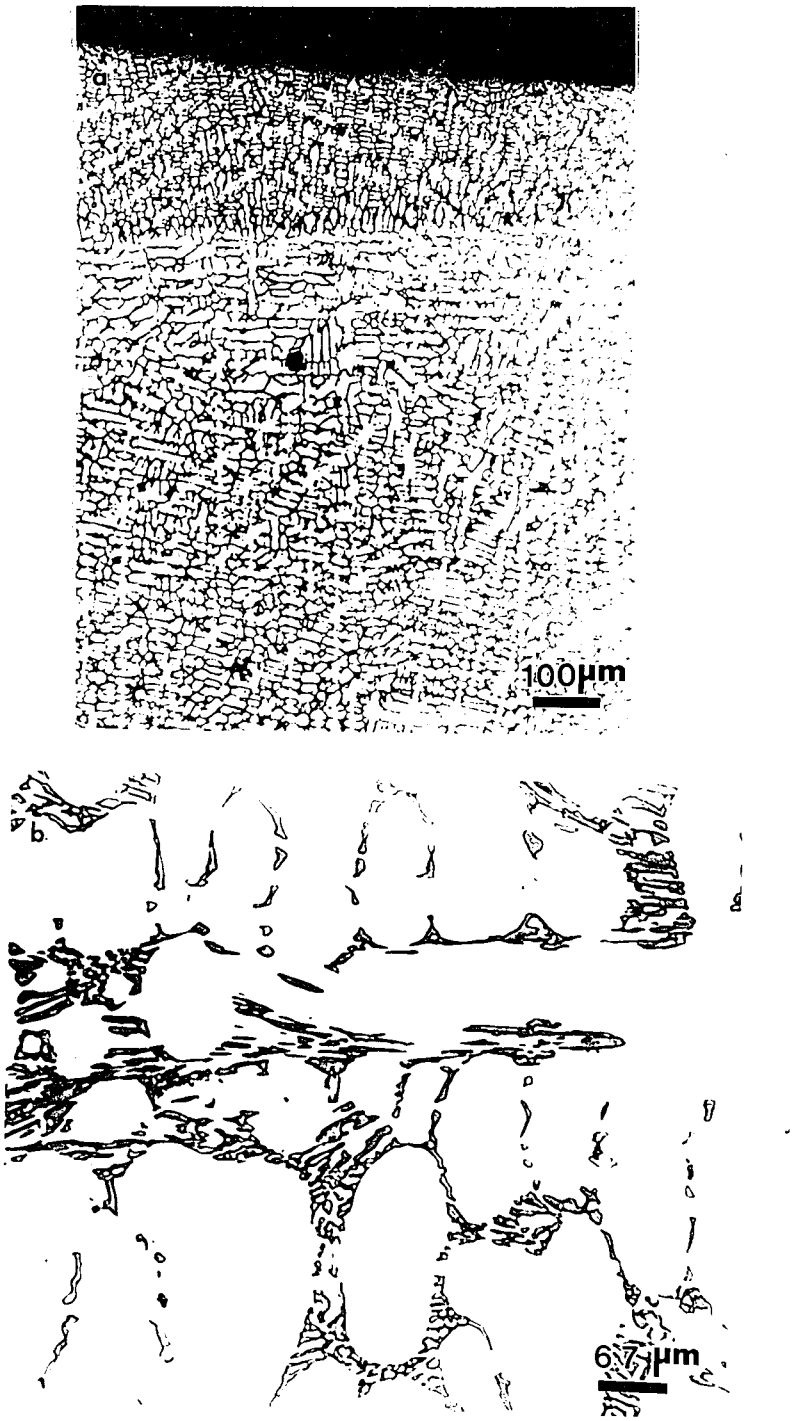

Figure 18. As-welded microstructure of the Stellite-6 weld overlay coating; (a) top of the coating; (b) matrix dendrites (white) and interdendritic phase (dark). Etchant-Muracami reagent.

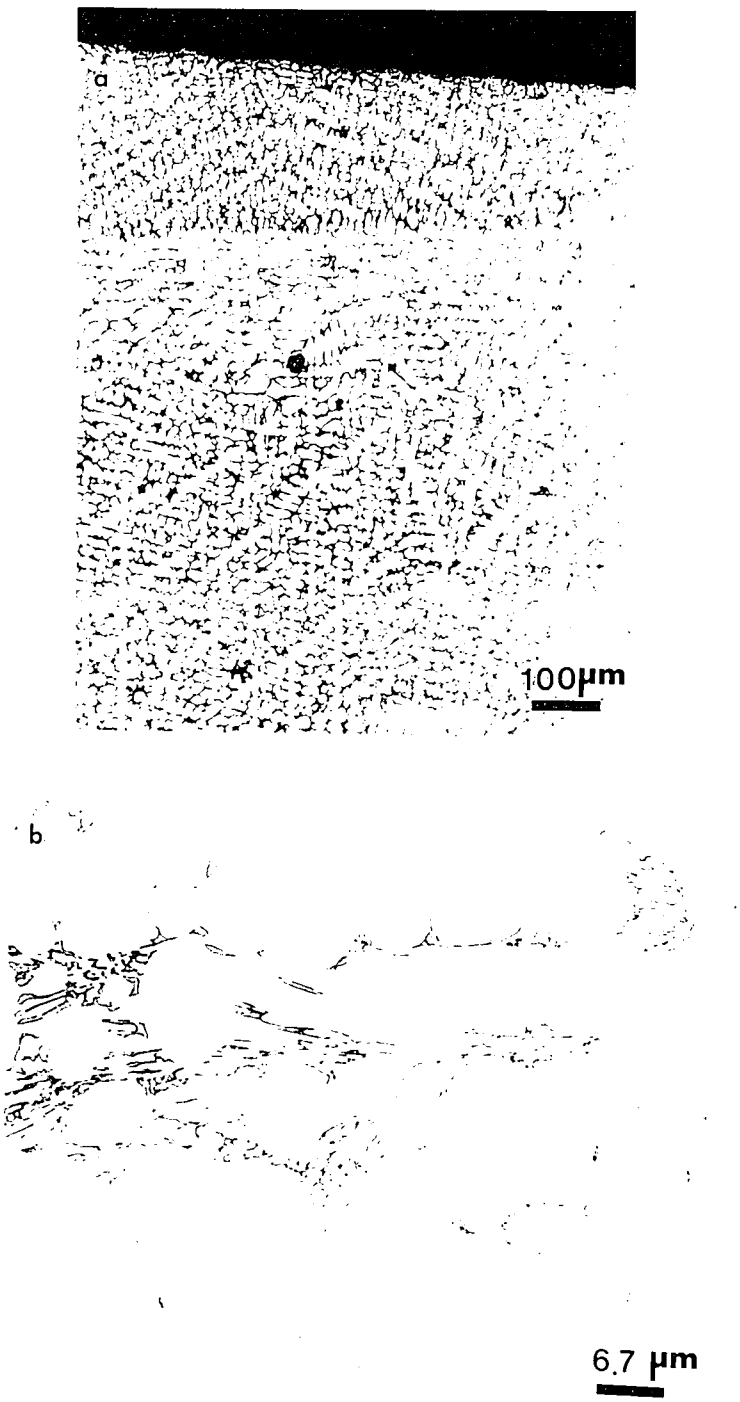

Figure 18. As-welded microstructure of the Stellite-6 weld overlay coating; (a) top of the coating; (b) matrix dendrites (white) and interdendritic phase (dark). Etchant-Muracami reagent.

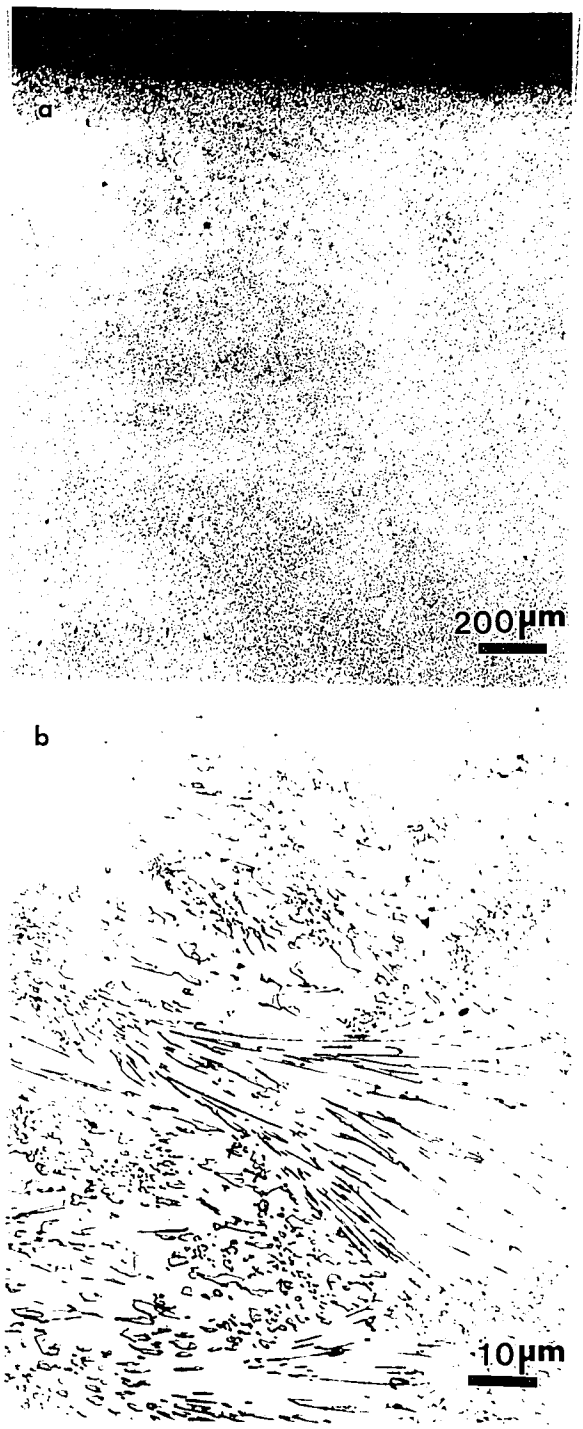

Figure 19. As-welded microstructure of the TS-2 weld overlay coating; (a) top of coating; (b) second phase particles (dark phase). Etchant-Muracami reagent.

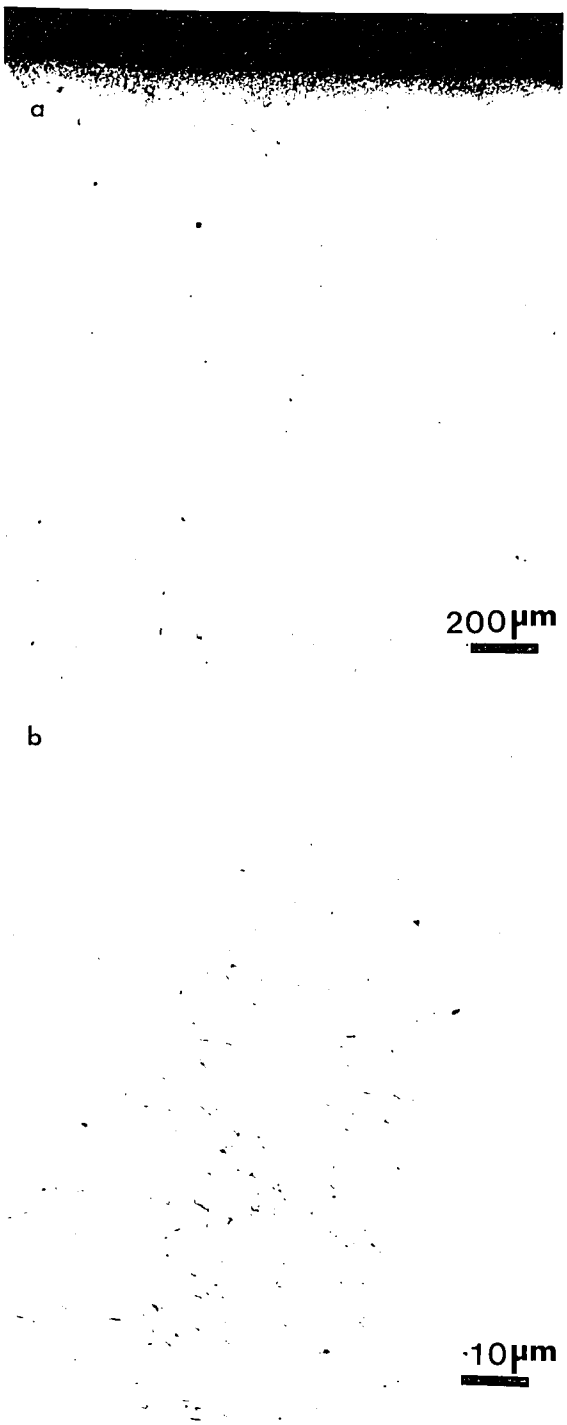

Figure 19. As-welded microstructure of the TS-2 weld overlay coating; (a) top of coating; (b) second phase particles (dark phase). Etchant-Muracami reagent.

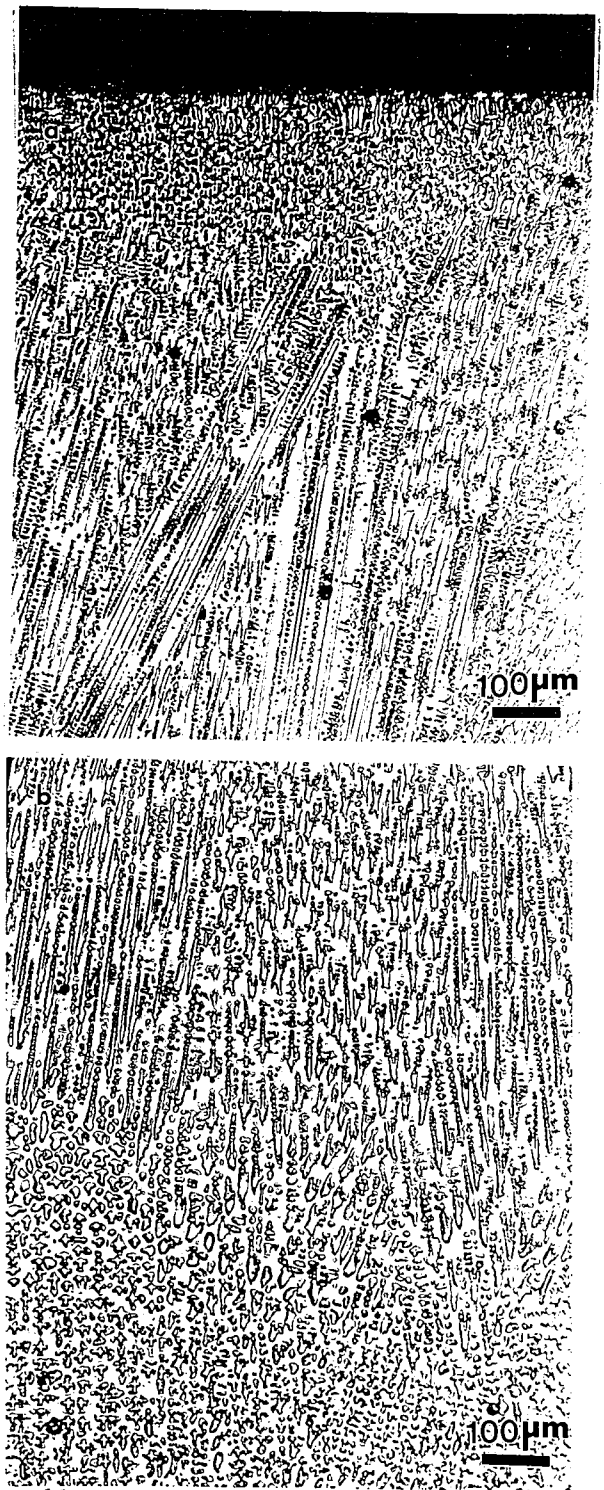

Figure 20. As-welded microstructure of the Ultimet weld overlay coating; (a) top of the coating; (b) dendritic microstructure in different regions of the sample, dendrites have various size and shape. Etchant: [16ml Cr_2O_3, 16ml water, and 30ml HCl] solution.

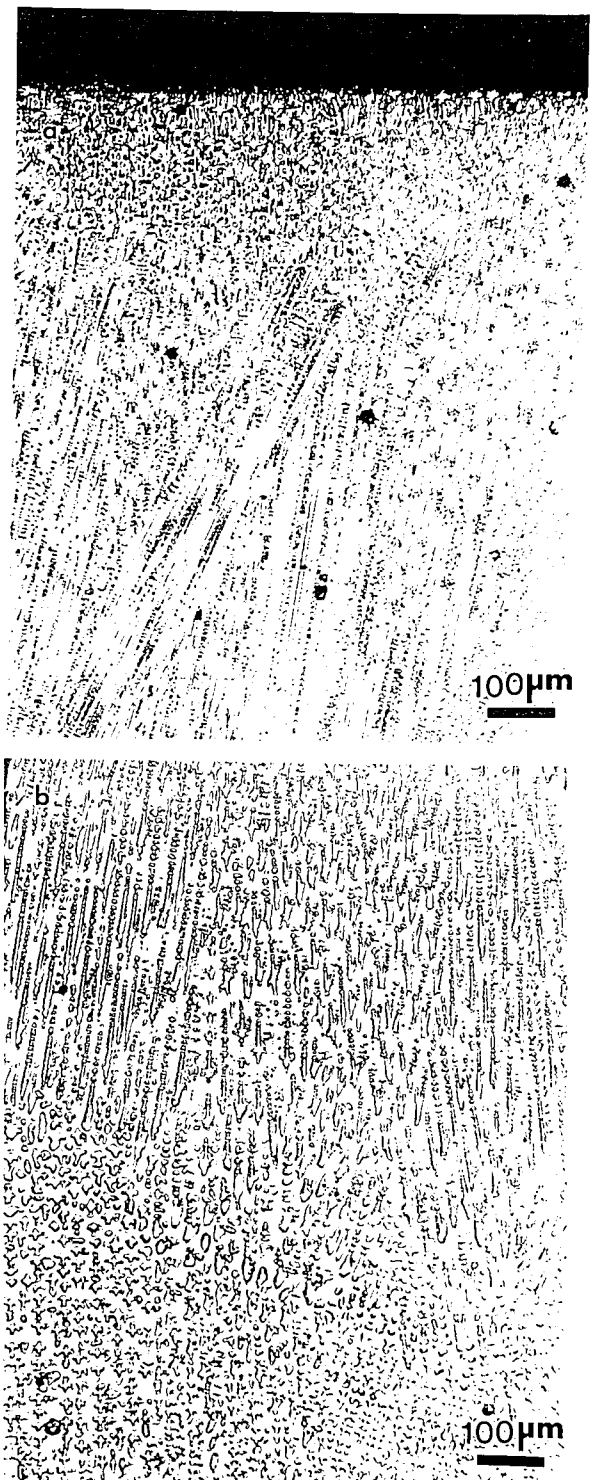

Figure 20. As-welded microstructure of the Ultimet weld overlay coating; (a) top of the coating; (b) dendritic microstructure in different regions of the sample, dendrites have various size and shape. Etchant: [16ml Cr_2O_3, 16ml water, and 30ml HCl] solution.

may be carbides and/or intermetallics. Work is required to determine quantitative and qualitative information about the phases in the TS-2 and Ultimet weld overlay coatings.

IV.A.2. Nickel-Base Coatings

All nickel-base welds had a dendritic microstructures. Microstructures of Inconel-625 and Hastelloy-22 coatings appeared to be somewhat similar (Figures 21 and 22, respectively) and possessed fine dendrites that have different shapes and orientations. The welding and solidification behavior of Inconel-625 alloy has been studied in detail [49] and it was found that the interdendritic regions consisted of NbC type carbides and Laves phases in the form of Ni_3SiNb_2 [50]. It also has been established that the weld microstructure of the Inconel-625 alloy is controlled by segregation of the niobium, carbon, and silicon [49]. The matrix of the Inconel-625 consists of the gamma (γ) phase. The microstructure of Inconel-625 wrought alloy is shown in Figure 21c. The wrought alloy was annealed by the supplier and the temperature of the annealing is not known. The microstructure of this alloy consists of fine austenite grains and annealing twins. However, very large grains are also randomly present in the microstructure. From Figure 23 it can be seen that the microstructure of the B-60 weld overlay consists of a crack that runs at a 45° angle to the coating surface. The cracking does not appear to be associated with any particular microstructural feature.

IV.A.3. Iron-Base Coatings

The photomicrographs of the iron-base weld overlay coatings are shown in Figures 24-28. The Iron-Aluminide coating microstructure is significantly different from all

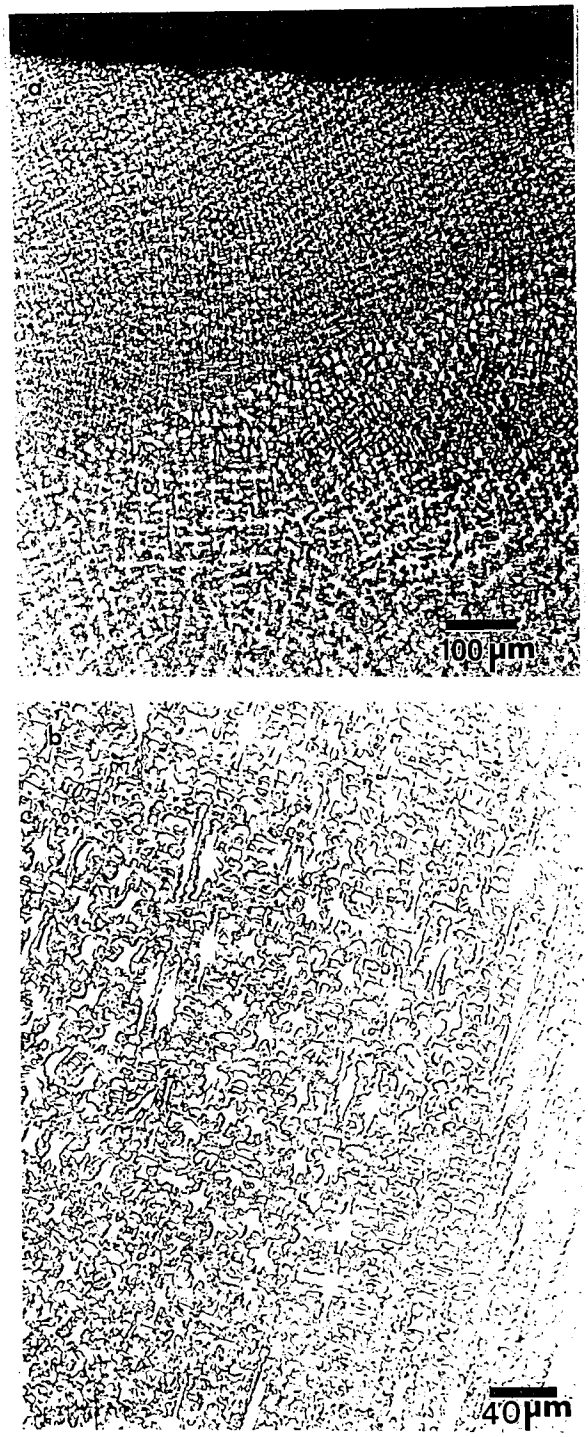

Figure 21. As-welded microstructure of the Inconel-625 weld overlay coating; (a) top of the coating; (b) high magnification of the dendritic microstructure. Etchant: electrolytic-5V [5g oxalic acid and 85ml HCl] solution.

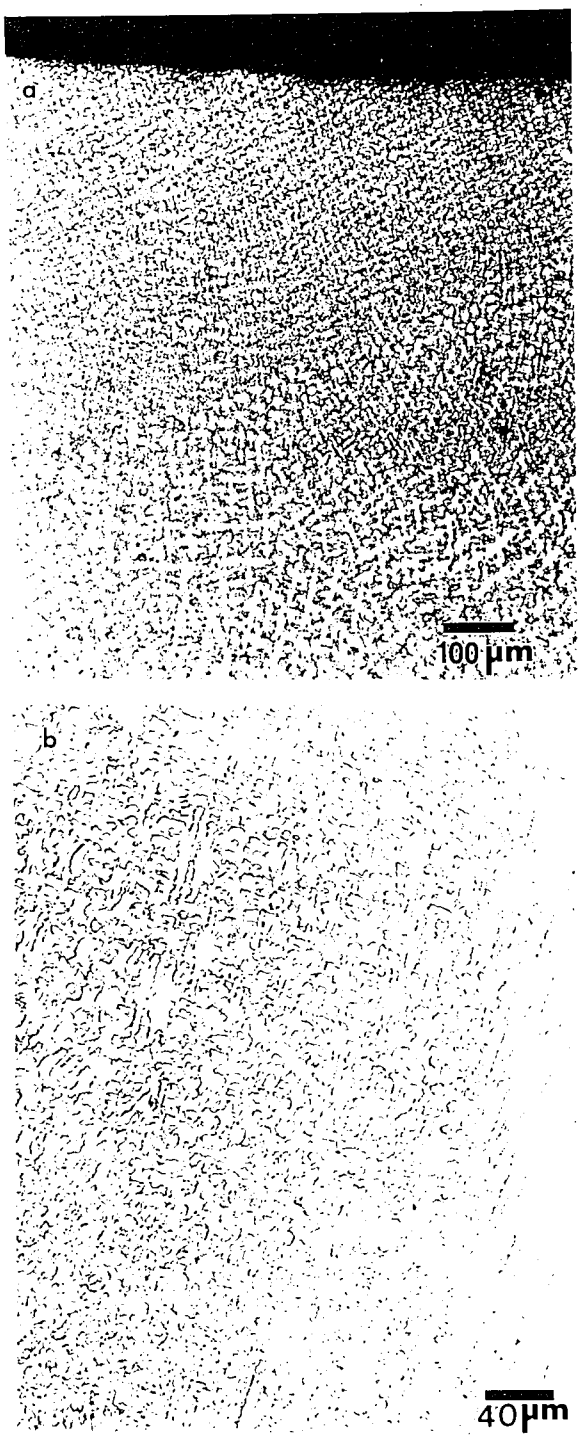

Figure 21. As-welded microstructure of the Inconel-625 weld overlay coating; (a) top of the coating; (b) high magnification of the dendritic microstructure. Etchant: electrolytic-5V [5g oxalic acid and 85ml HCl] solution.

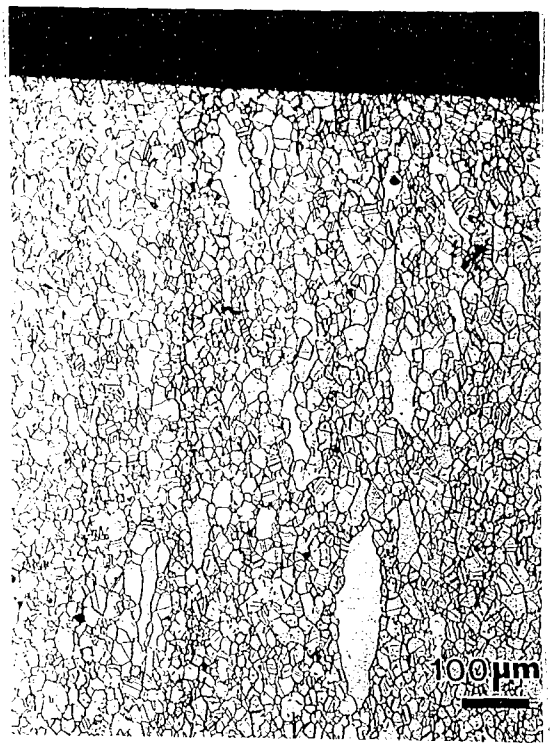

Figure 21c. The microstructure the wrought Inconel-625 alloy. Structure consists of austenite grains and annealing twins.

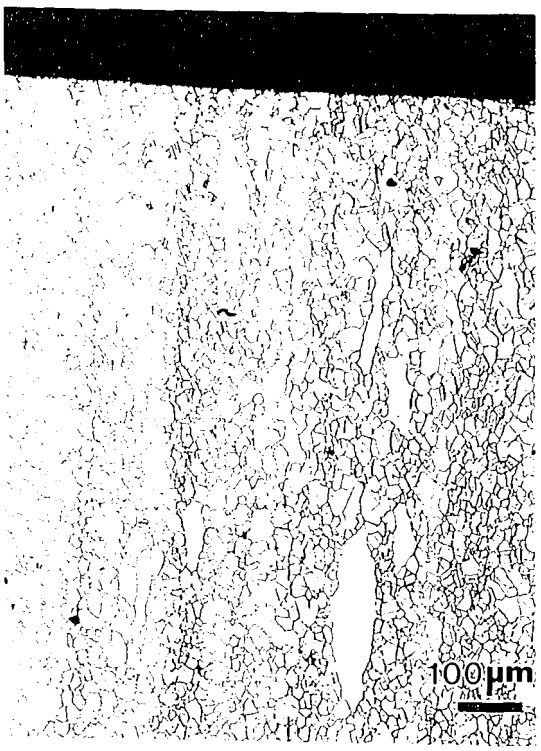

Figure 21c. The microstructure the wrought Inconel-625 alloy. Structure consists of austenite grains and annealing twins.

Figure 22. As-welded microstructure of the Hastelloy-22 weld overlay coating (top of the coating). Etchant: [16ml Cr_2O_3, 16ml water, and 30ml HCl] solution.

Figure 22. As-welded microstructure of the Hastelloy-22 weld overlay coating (top of the coating). Etchant: [16ml Cr_2O_3, 16ml water, and 30ml HCl] solution.

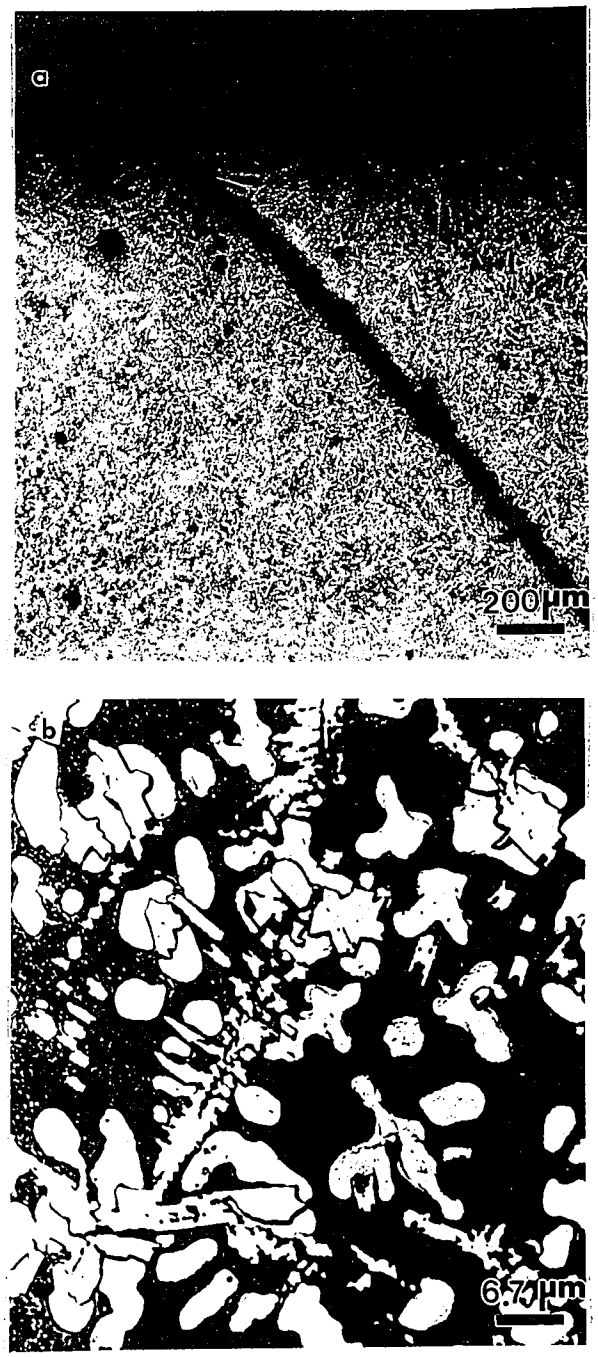

Figure 23. As-welded microstructure of the B-60 weld overlay coating; (a) top of the coating and crack that run from the top; (b) high magnification view of the dendrites. Etchant: Glicerigia reagent.

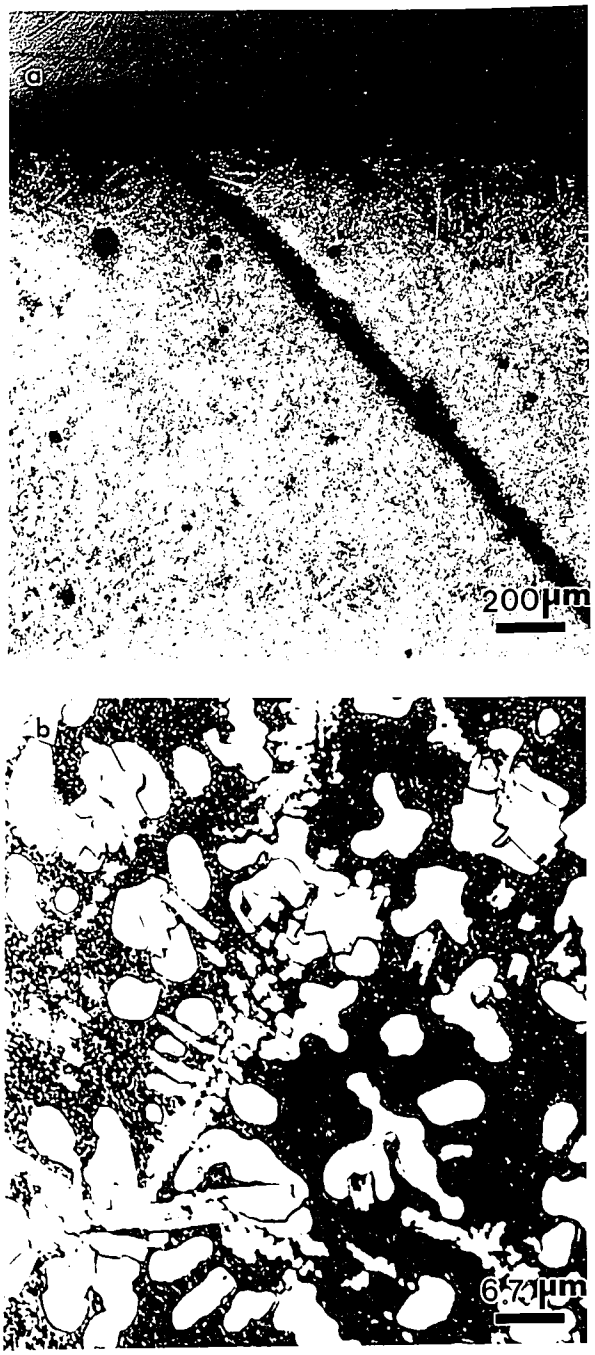

Figure 23. As-welded microstructure of the B-60 weld overlay coating; (a) top of the coating and crack that run from the top; (b) high magnification view of the dendrites. Etchant: Glicerigia reagent.

other coatings studied, Figure 24 (a,b, and c,). From Figures 24a and 24b (low magnification), it can be seen that the grain morphology of the coating consists of large columnar grains. Equiaxed grains are also present in the microstructure. Also, second phase precipitates within the grains (dark features) can be observed from the photomicrographs. A high magnification photomicrograph of these precipitates within the grains and at the grain boundaries are shown in Figures 24c. The chemical composition of these precipitates was not determined. The microstructure of Iron-Aluminide wrought alloy is shown in Figure 24d. From this figure, equiaxed grain morphology can be seen. The second phase precipitates are also present in microstructure.

The microstructure of the Armacor-M weld overlay coating is shown in Figure 25 (a,b, and c). From Figures 25a and 25b it can be seen that the coating microstructure possesses a needle-like phase of various sizes (white phase) in a metal matrix. Based upon its microstructural appearance and the chemical composition of the alloy powder, it is expected that this needle-like phase is a boride. Also, cracks were observed in the Armacor-M weld overlay deposit. A photomicrograph of the coating that contains a crack is shown in Figure 25c. The observed cracks were perpendicular to the weld bead and run through the entire coating.

Photomicrographs of the High-Chromium Iron are shown in Figure 26 (a and b). The microstructure of as-cast high-chromium irons has been investigated by many authors [36,51]. It was found that the as-cast microstructure consisted of austenite/or ferrite dendrites with an interdendritic mixture of austenite/or ferrite and Cr-rich M_7C_3

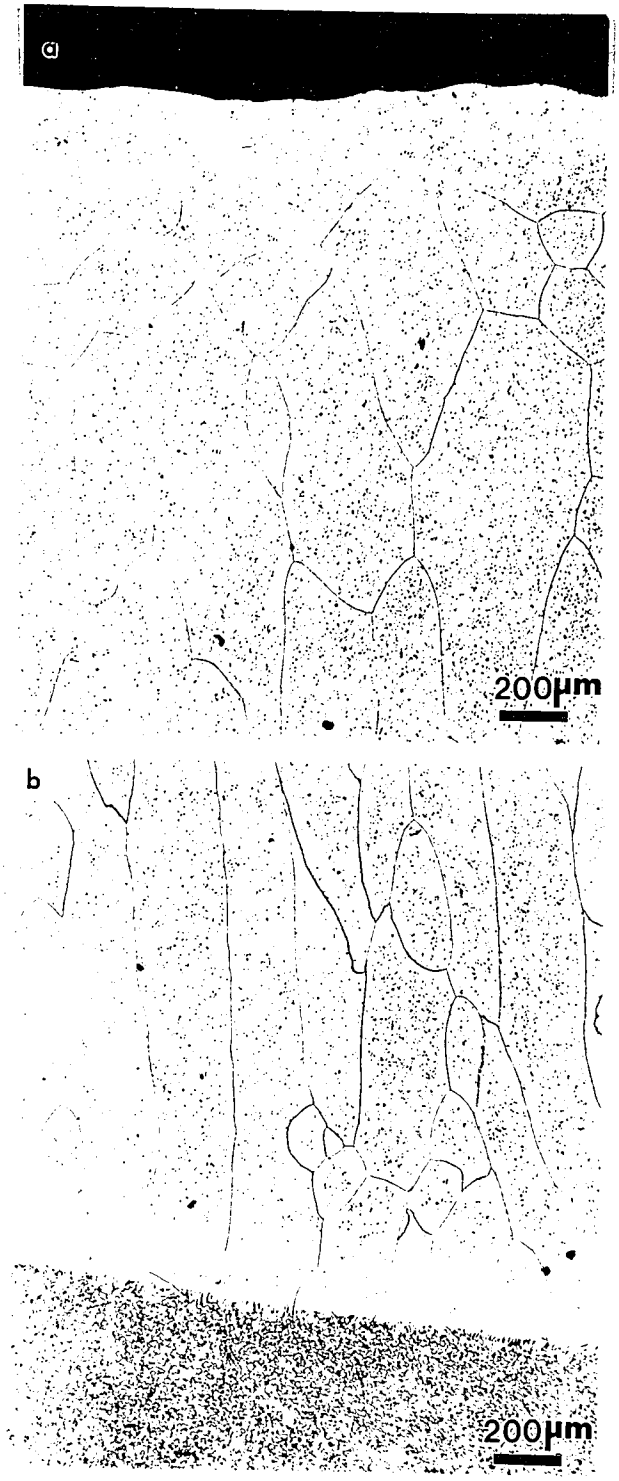

Figure 24. As-welded microstructure of the Iron-Aluminide weld overlay coating; (a) top of the coating; (b) coating/substrate interface. Etchant: Marshall reagent.

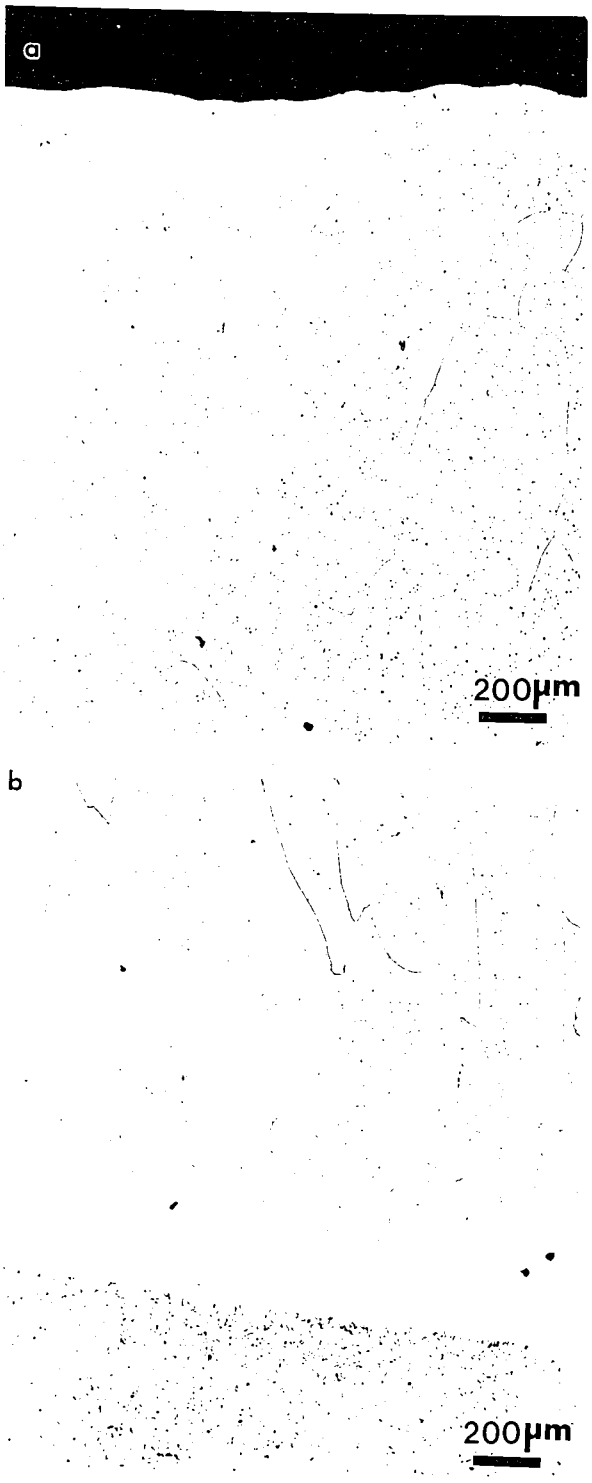

Figure 24. As-welded microstructure of the Iron-Aluminide weld overlay coating; (a) top of the coating; (b) coating/substrate interface. Etchant: Marshall reagent.

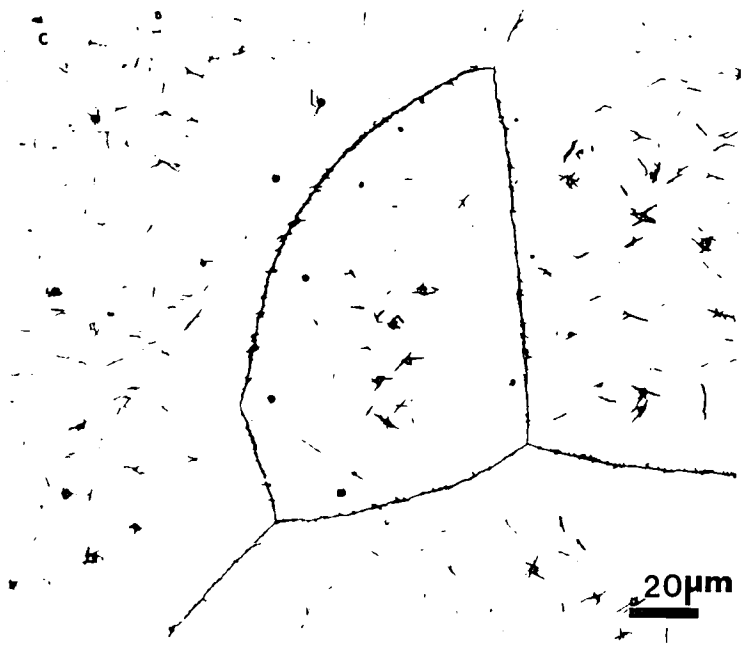

Figure 24c. As-welded microstructure of the Iron-Aluminide weld overlay coating; (a) top of the coating; (c) precipitates within the grain and at the grain boundaries. boundaries.

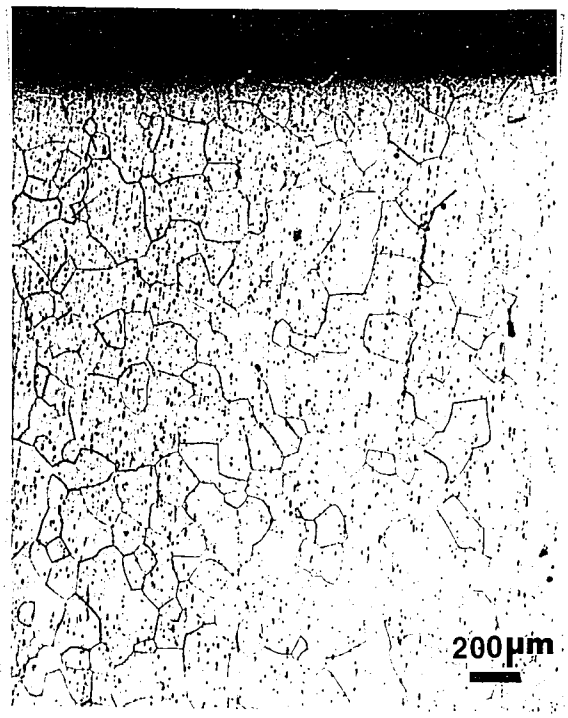

Figure 24d. The microstructure of the wrought Iron-Aluminide alloy. Structure consists of equiaxed grains and precipitates within the grains (dark phase).

Figure 24d. The microstructure of the wrought Iron-Aluminide alloy. Structure consists of equiaxed grains and precipitates within the grains (dark phase).

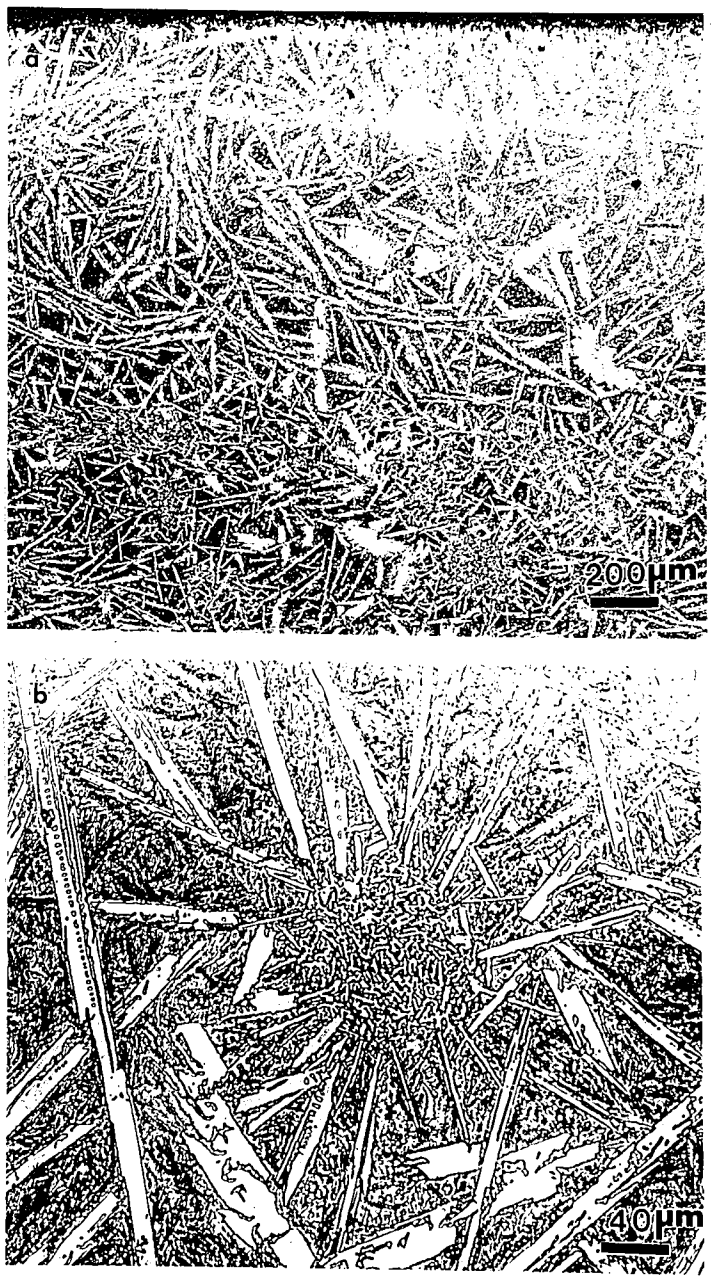

Figure 25. As-welded microstructure of the Armacor-M weld overlay coating; (a) top of the coating; (b) high magnification view of the needle-like phase. Etchant: Glicerigia reagent.

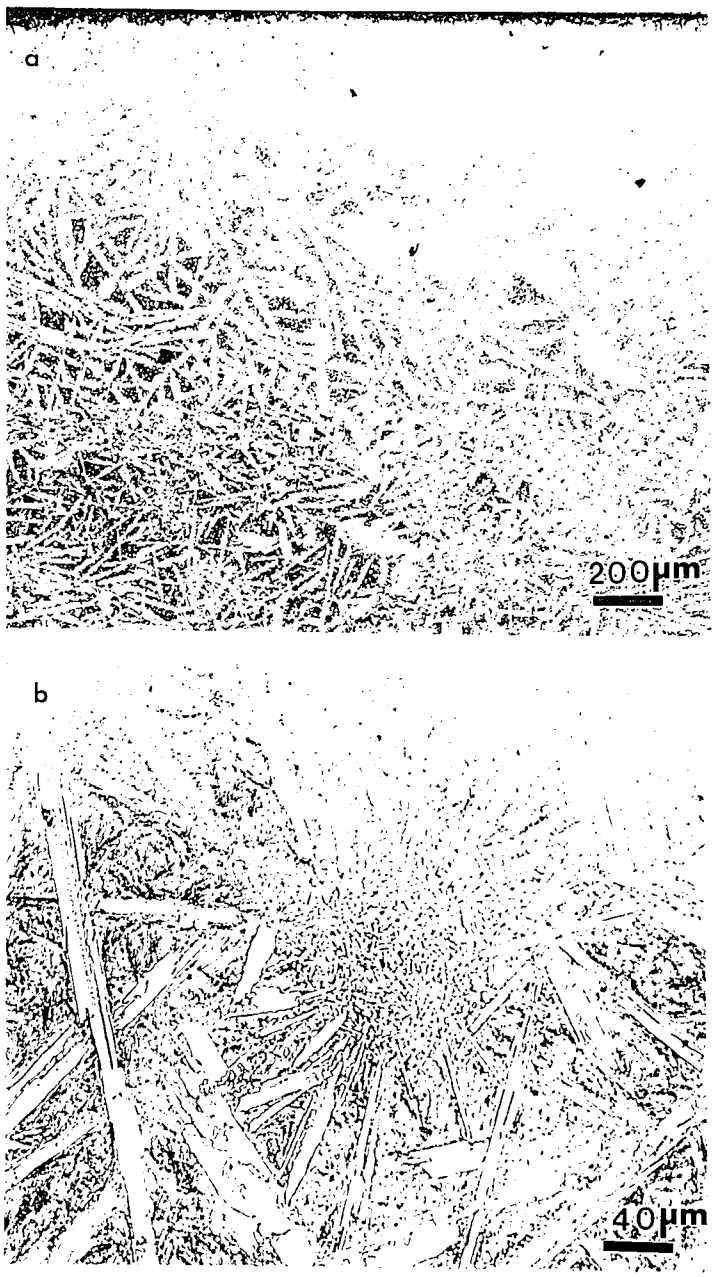

Figure 25. As-welded microstructure of the Armacor-M weld overlay coating; (a) top of the coating; (b) high magnification view of the needle-like phase. Etchant: Glicerigia reagent.

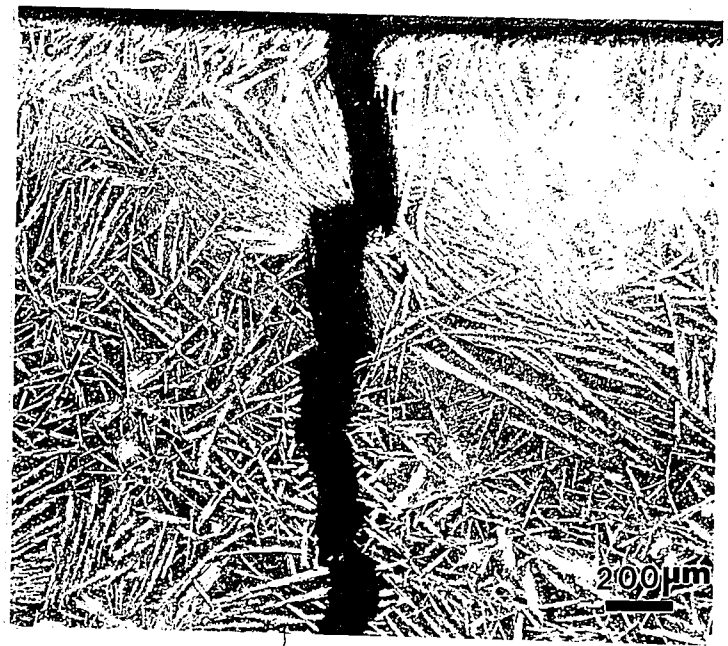

Figure 25c. As-welded microstructure of the Armacor-M Weld Overlay Coating (crack that run through the coating.

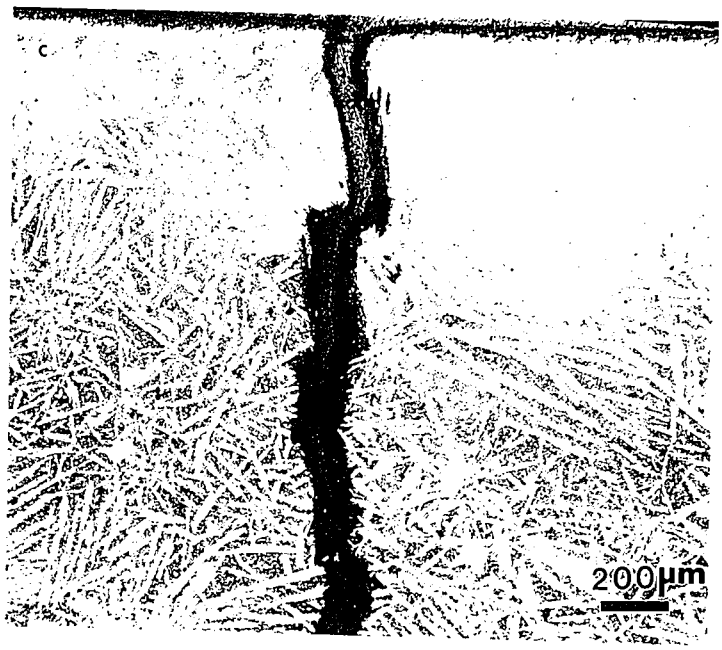

Figure 25c. As-welded microstructure of the Armacor-M Weld Overlay Coating (crack that run through the coating.

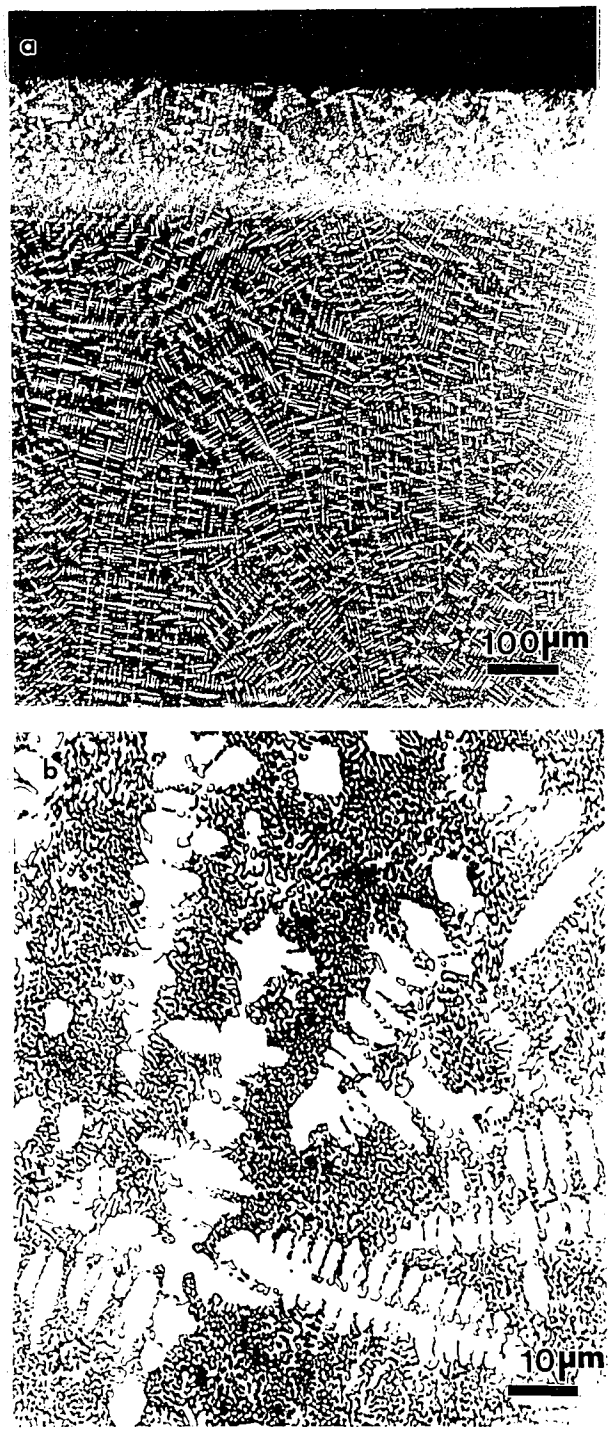

Figure 26. As-welded microstructure of the High Chromium Iron weld overlay coating; (a) top of the coating; (b) dendrites in the coating microstructure. Etchant: Muracami reagent.

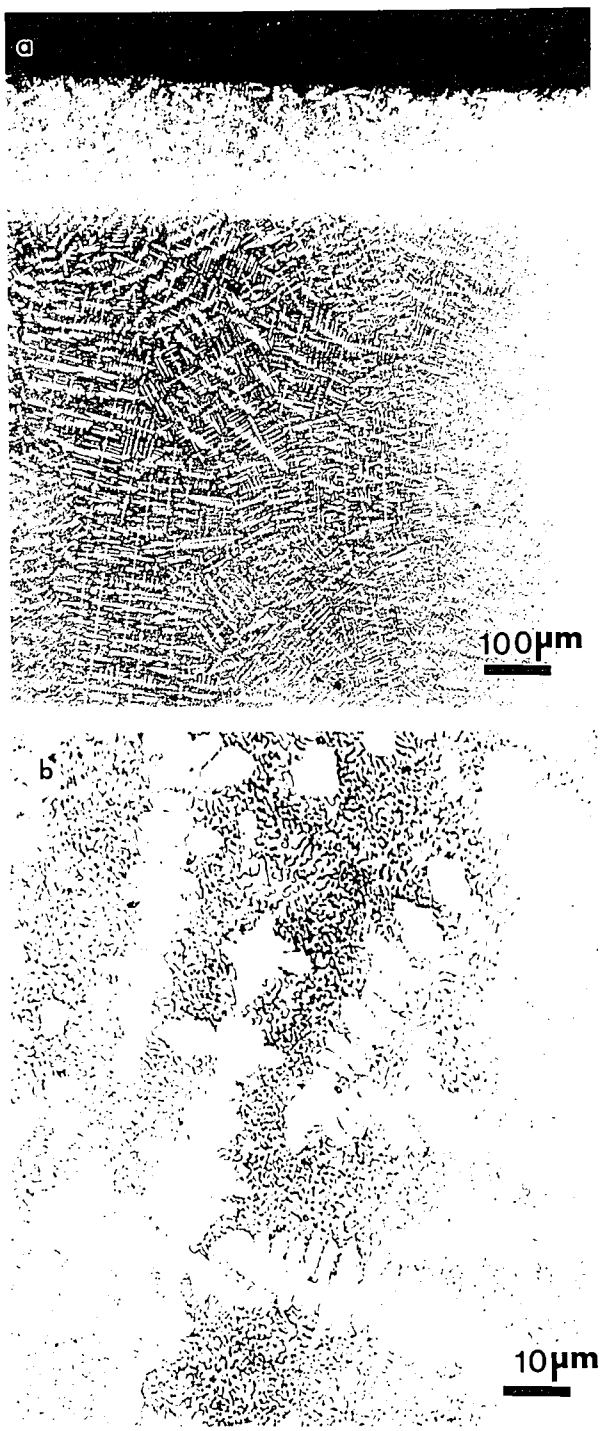

Figure 26. As-welded microstructure of the High Chromium Iron weld overlay coating: (a) top of the coating; (b) dendrites in the coating microstructure. Etchant: Muracami reagent.

carbides [51].

The microstructure of the 316L SS (austenitic stainless steel) and 420 SS (martensitic stainless steel) weld overlay coatings are shown in Figures 27 and 28, respectively. The microstructure of the 316L SS coating possesses dendrites of delta ferrite (dark phase) and an austenite matrix (white phase). The microstructure of wrought 316L SS alloy is shown in Figure 27c. The microstructure consists of equiaxed austenite grains and annealing twins. The microstructure of the 420 SS coating contains lath martensite (Figure 28b) and ferrite and/or austenite (white phase). Inspection of Figure 28c (high magnification) shows the prior austenite grains in the coating microstructure.

IV.A.4. Microhardness Measurements

The room temperature microhardness test results are shown in Figure 29 (a-k). The tests started at the coating surface and proceeded well into the base metal. It can be seen that all the coatings have a higher hardness than the substrate material. It should be noted that for B-60 and Armacor-M alloys (Figures 29i and j, respectively) a large scatter in hardness was observed. This effect is probably occurred due to the non-homogeneous microstructures of these alloys which include large amounts of second phase particles that vary in size. The high hardness of these weld overlay deposits is probably due to the presence of hard second phase particles, especially carbides and borides in the coating matrix. However, at high hardness levels, the tensile ductility of the weld overlay coating is reduced [52]. Apparently, this is the main reason for crack formation in B-60 and Armacor-M coatings, both of which

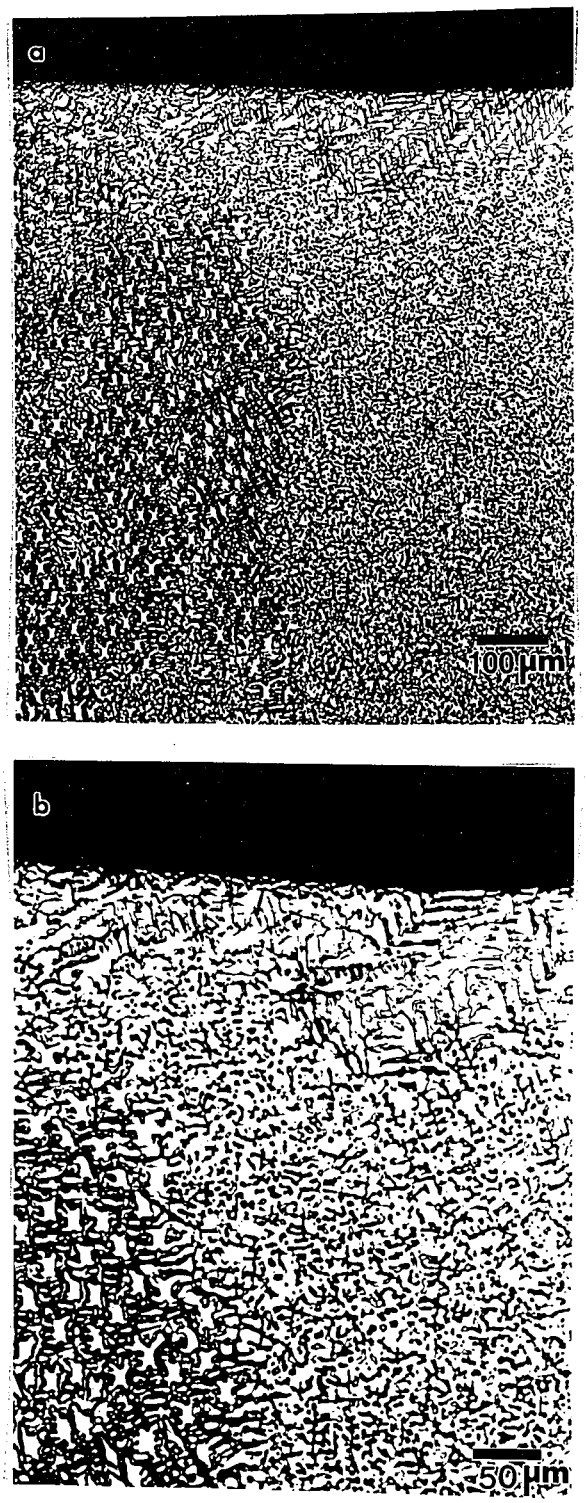

Figure 27. As-welded microstructure of the 316L SS weld overlay coating; (a) top of the coating; (b) delta ferrite in austenitic matrix. Etchant: electrolytic-5V [60% HNO_3 and 40% water] solution.

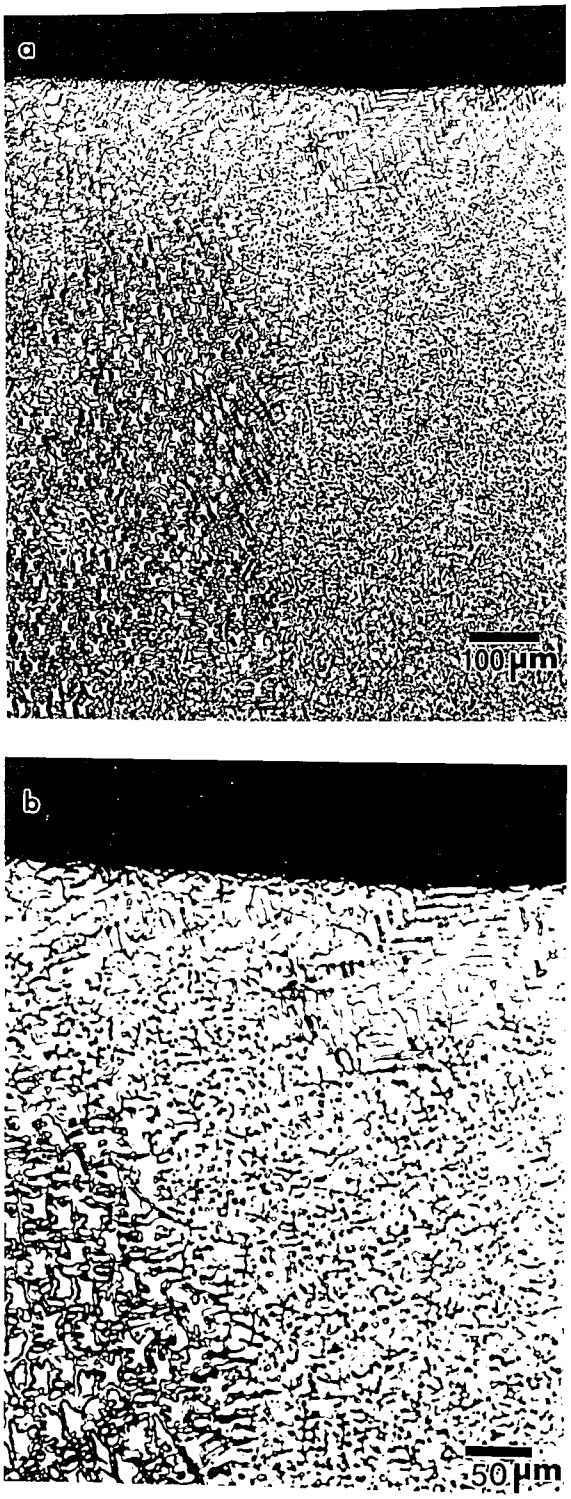

Figure 27. As-welded microstructure of the 316L SS weld overlay coating; (a) top of the coating; (b) delta ferrite in austenitic matrix. Etchant: electrolytic-5V [60% HNO_3 and 40% water] solution.

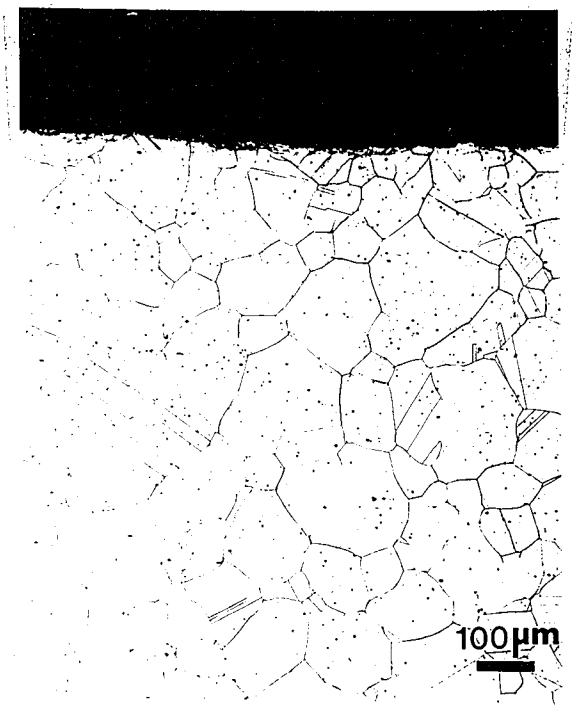

Figure 27c. Microstructure of the wrought 316L SS alloy. Microstructure consists of austenite grains and annealing twins.

Figure 27c. Microstructure of the wrought 316L SS alloy. Microstructure consists of austenite grains and annealing twins.

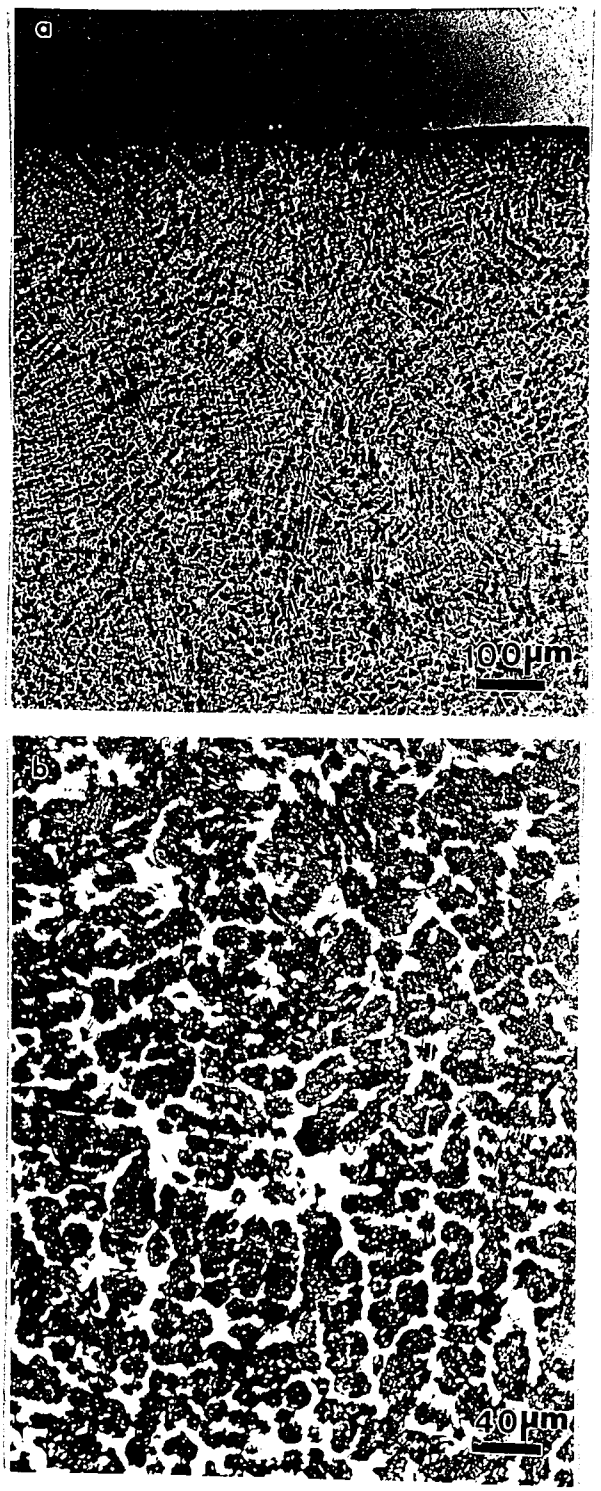

Figure 28. As-welded microstructure of the 420 SS weld overlay coating; (a) top of the coating; (b) dendrites of the lath martensite. Etchant: Viella reagent.

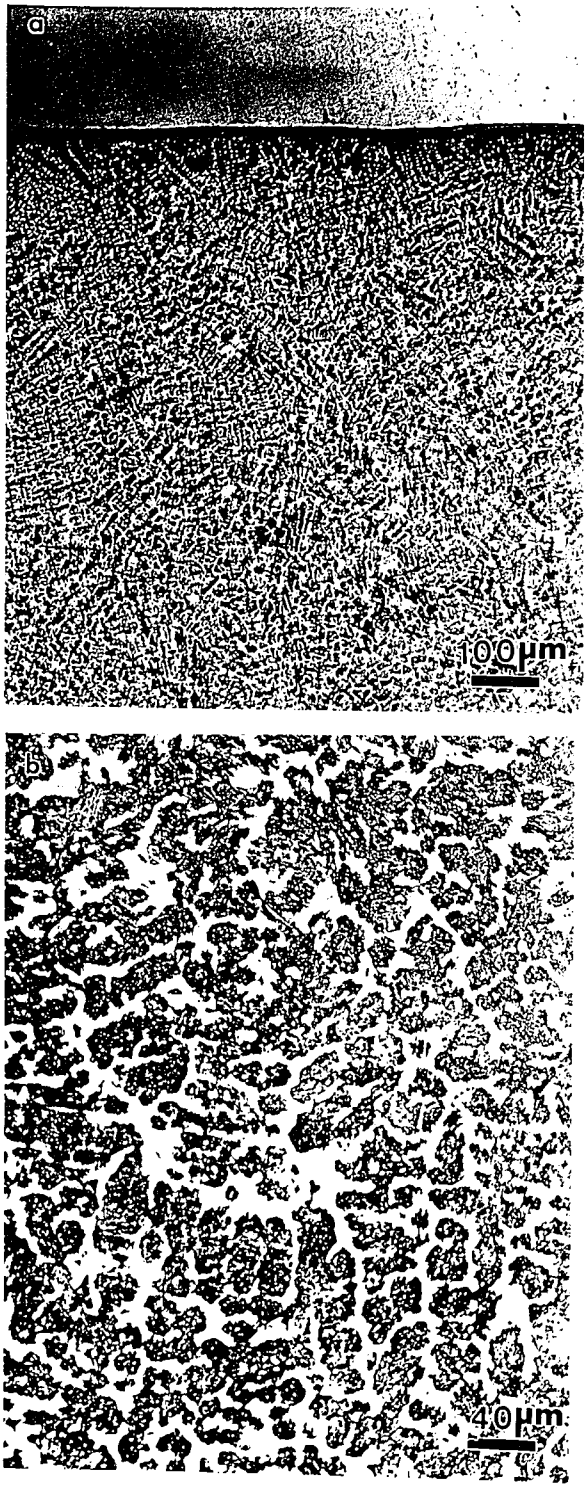

Figure 28. As-welded microstructure of the 420 SS weld overlay coating; (a) top of the coating; (b) dendrites of the lath martensite. Etchant: Viella reagent.

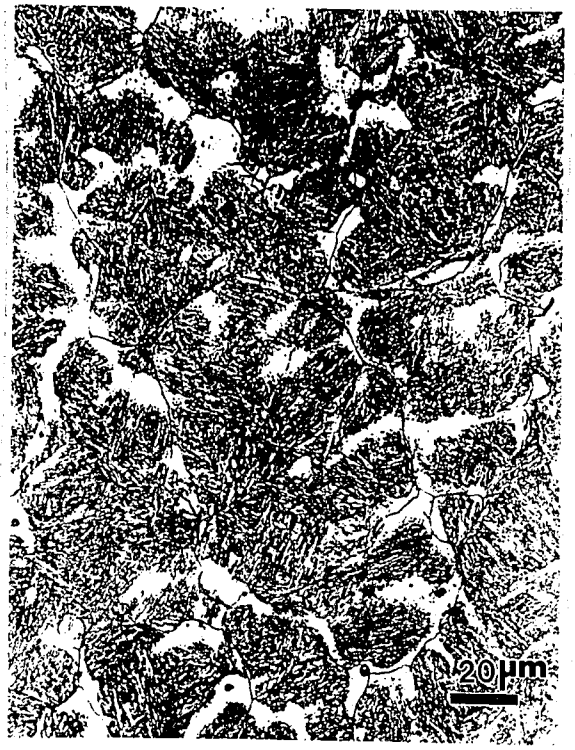

Figure 28c . As-welded microstructure of the 420 SS weld overlay coating; lath martensite within prior austenite grains.

Figure 28c . As-welded microstructure of the 420 SS weld overlay coating: lath martensite within prior austenite grains.

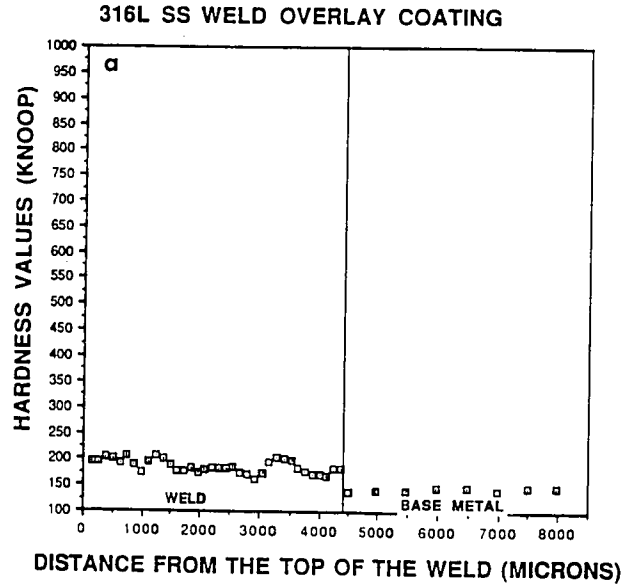

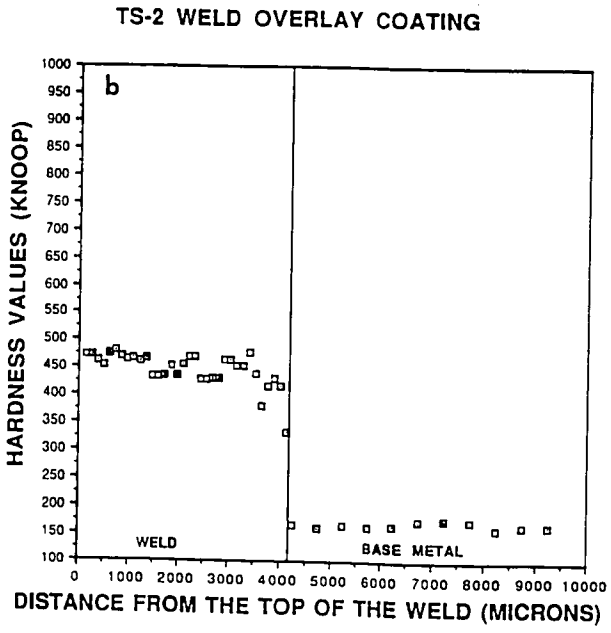

Figure 29 (a-k). Microhardness values across the longitudinal section of the weld.

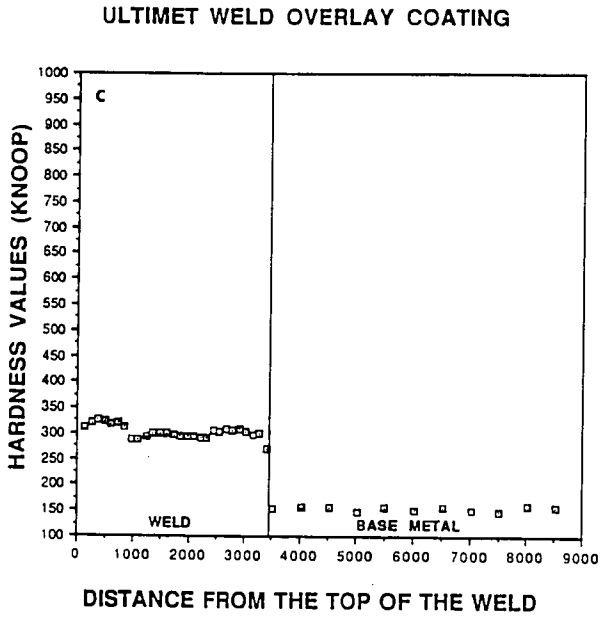

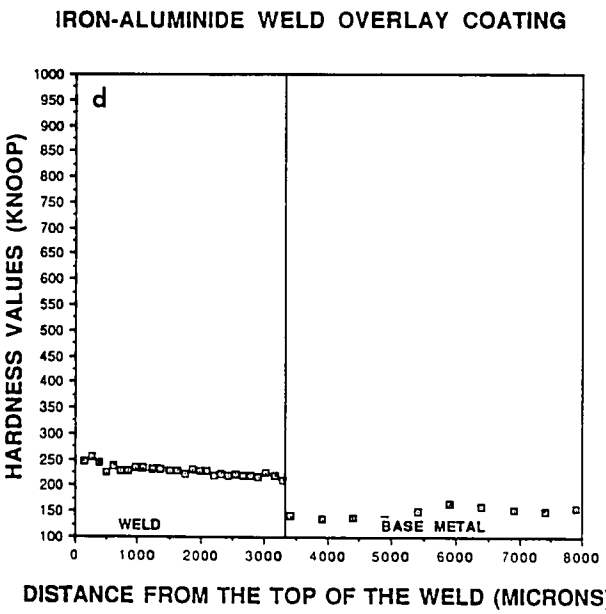

Figure 29 (c and d). Microhardness values across the longitudinal section of the weld.

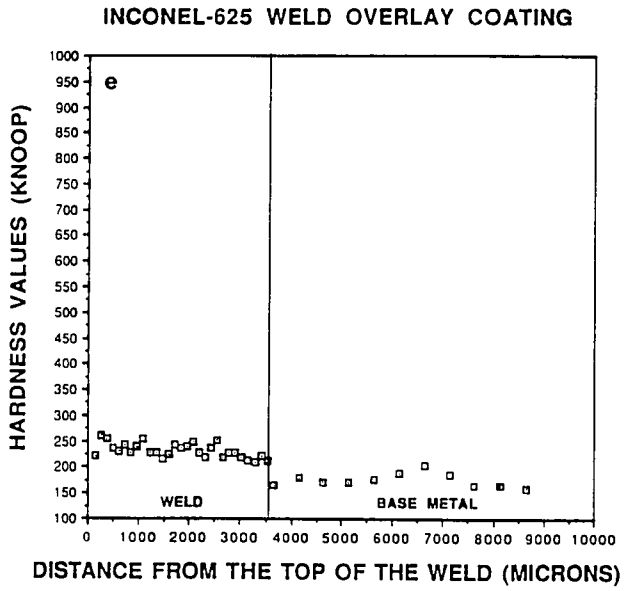

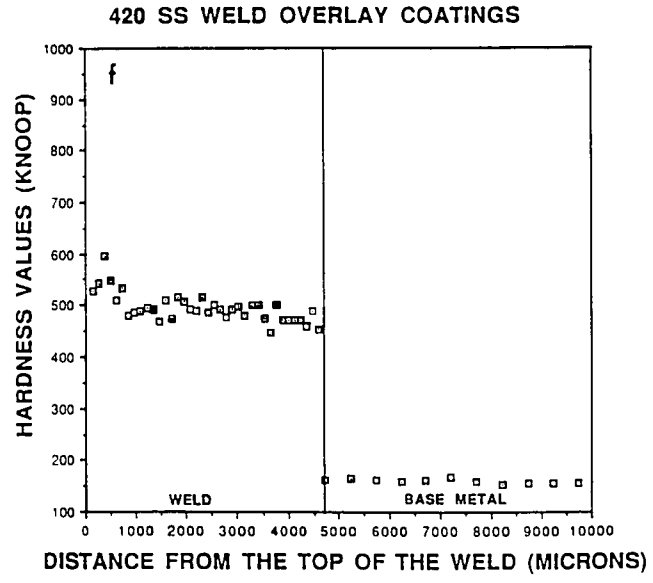

Figure 29 (e and f). Microhardness values across the longitudinal section of the weld.

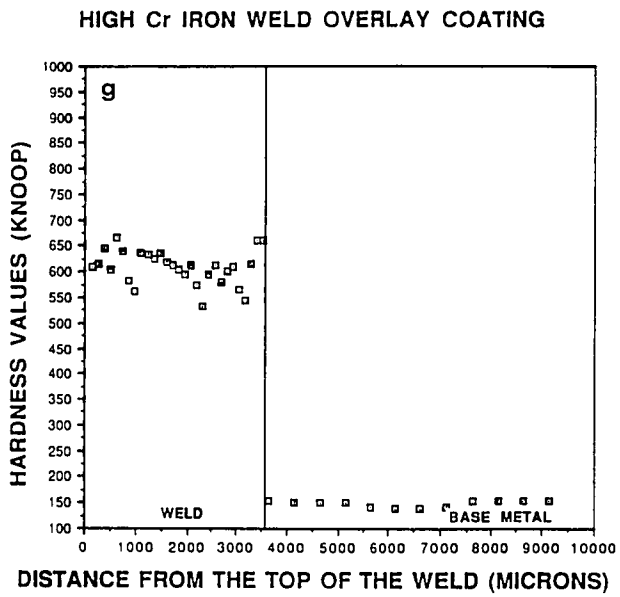

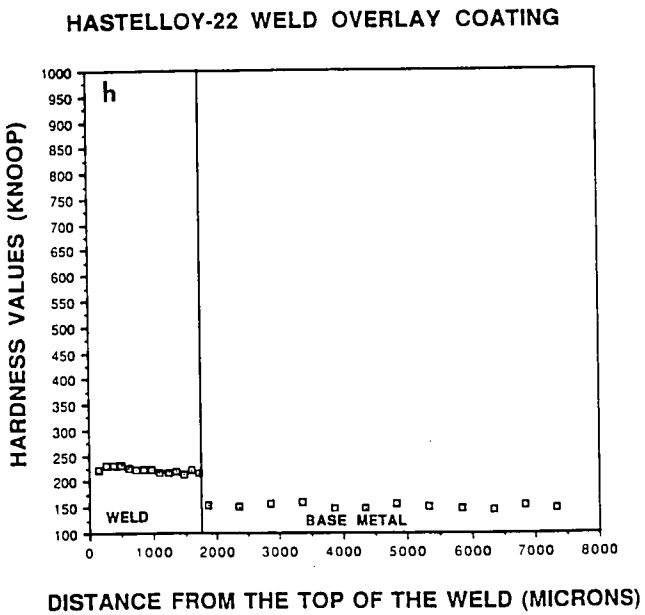

Figure 29 (g and h). Microhardness values across the longitudinal section of the weld.

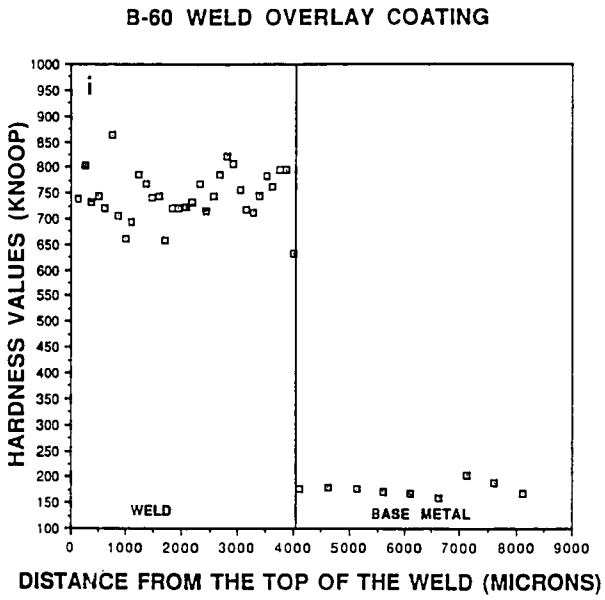

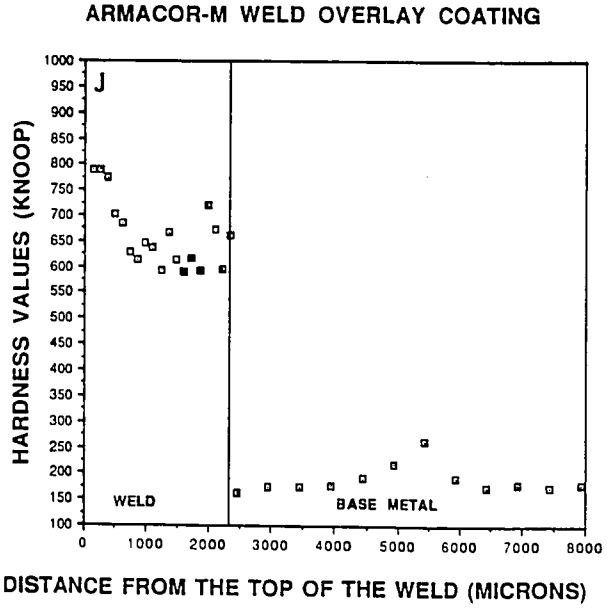

Figure 29 (i and j). Microhardness values across the longitudinal section of the weld.

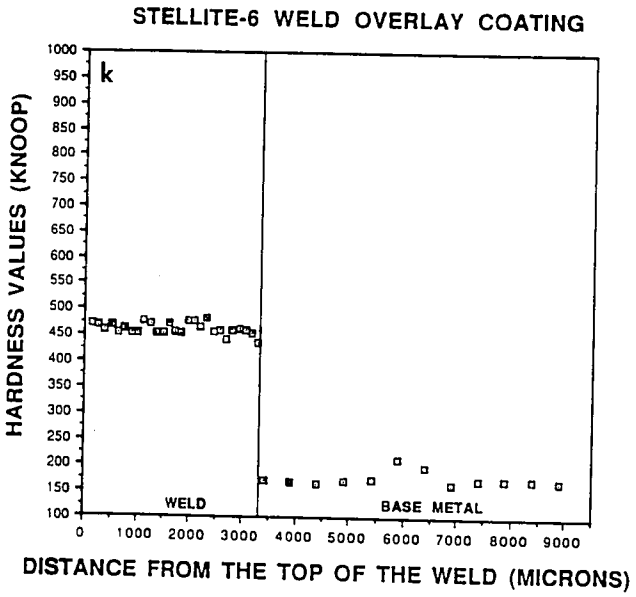

Figure 29 (k). Microhardness values across the longitudinal section of the weld.

exhibited very high hardness levels (up to 850 HK) compared with the substrate (175 HK). During the deposition of hardfacing coatings such as B-60 and Armacor-M, stresses due to the expansion mismatch between deposits and substrate is high. These coatings have a very high hardness compared with the substrate and, therefore, prevent accommodation of the shrinkage strain that occurs during cooling. As a result of this effect, cracking of the weld overlay deposits was observed.

IV.A.5. High Temperature Microhardness Measurements

High temperature microhardness tests were performed on longitudinal sections of each weld overlay. Measurements were taken at 25°C and 400°C. The results of these tests are summarized in Table 8.

IV.B. EROSION TESTS

Erosion tests were performed for all weld overlay coatings at 400°C. The erosion test conditions and procedure for determination of the steady state erosion rates for each coating were described in section III.E.2.

IV.B.1. Cobalt-Base/Containing Coatings

The erosion kinetics of the cobalt-base coatings at 90° and 30° impact angles are shown in Figure 30. Also shown on the graphs are the slopes of the best-fit straight lines through the data points. The slopes of these lines give the steady state erosion rate in milligrams per minute (mg/min). At 90° impact angle, the Ultimet and TS-2 coatings have nearly identical weight loss erosion rates, 0.072 mg/min and 0.074 mg/min, respectively. The TS-2 coating exhibited an incubation time of approximately

Table 8. Results of the high temperature microhardness tests.

WELD OVERLAY	AVERAGE VICKERS HARDNESS AT 25°C (500g load)	AVERAGE VICKERS HARDNESS AT 400°C (500g load)
STELLITE-6	470±30	320±15
TS-2	412±7	330±7
ULTIMET	230±16	121±8
IN-625	222±4	163±6
HASTELLOY-22	187±5	121±7
B-60	917±120	582±54
ARMACOR-M	688±72	650±52
IRON-ALUMINIDE	194±12	146±12
HIGH Cr IRON	631±26	403±12
316L SS	146±8	100±4
420 SS	463±22	350±10

5 minutes. The Stellite-6 weld overlay coating has a higher steady state erosion rate-0.101 mg/min. This coating exhibited a significant weight loss after 5 min of erosion and then showed a relatively long incubation period of approximately 15 min. Also, the Stellite-6 weld overlay coating shows the highest steady state erosion rate (0.104 mg/min) at 30° impact angle. At 30° impact angle, the Ultimet and TS-2 coatings have steady state erosion rates of 0.082 and 0.091 mg/min, respectively.

IV.B.2. Nickel-Base Weld Overlay Coatings

The erosion kinetics for the nickel-base coatings at 90° and 30° are shown in Figure 31. From Figure 31a it can be seen that Inconel-625 exhibited the lowest erosion rate (0.081mg/min) and the B-60 coating has the highest erosion rate 0.110 (mg/min). Also, the Inconel-625 weld overlay coating showed an incubation time of approximately 20 min. It was found that at 30° impact angle (Figure 31b) all the nickel-base weld overlay coatings showed similar steady state erosion rates (about 0.081 mg/min). Also, for the Inconel-625 coating, the steady state erosion rates did not vary with the impingement angle and an incubation period was not detected at 30° impact angle.

IV.B.3. Iron-Base Weld Overlay Coatings

The erosion kinetics for the iron-base weld overlay coatings at 90° and 30° impact angles are shown in Figures 32 and 33. The Armacor-M coating showed the highest weight loss erosion rate (0.162 mg/min) at 90° impact. 316L SS, 420SS, Iron-Aluminide, and High Chromium Iron showed steady state erosion rates of 0.078, 0.073, 0.073, and 0.084 mg/min, respectively at 90° impact angle. The Armacor-M

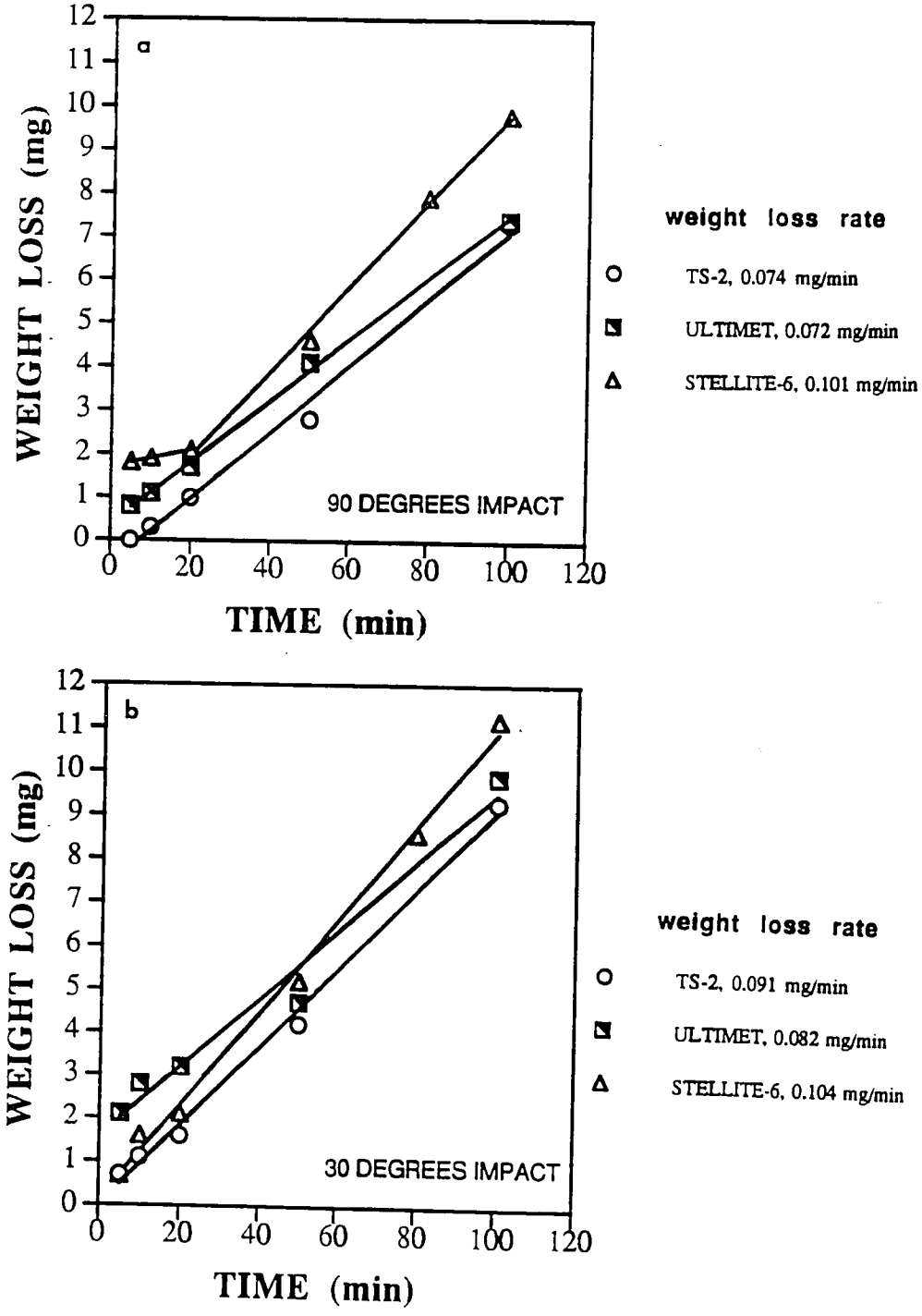

Figure 30. Weight loss as a function of time for cobalt-base weld overlay coatings; (a) 90° impact angle; (b) 30° impact angle.

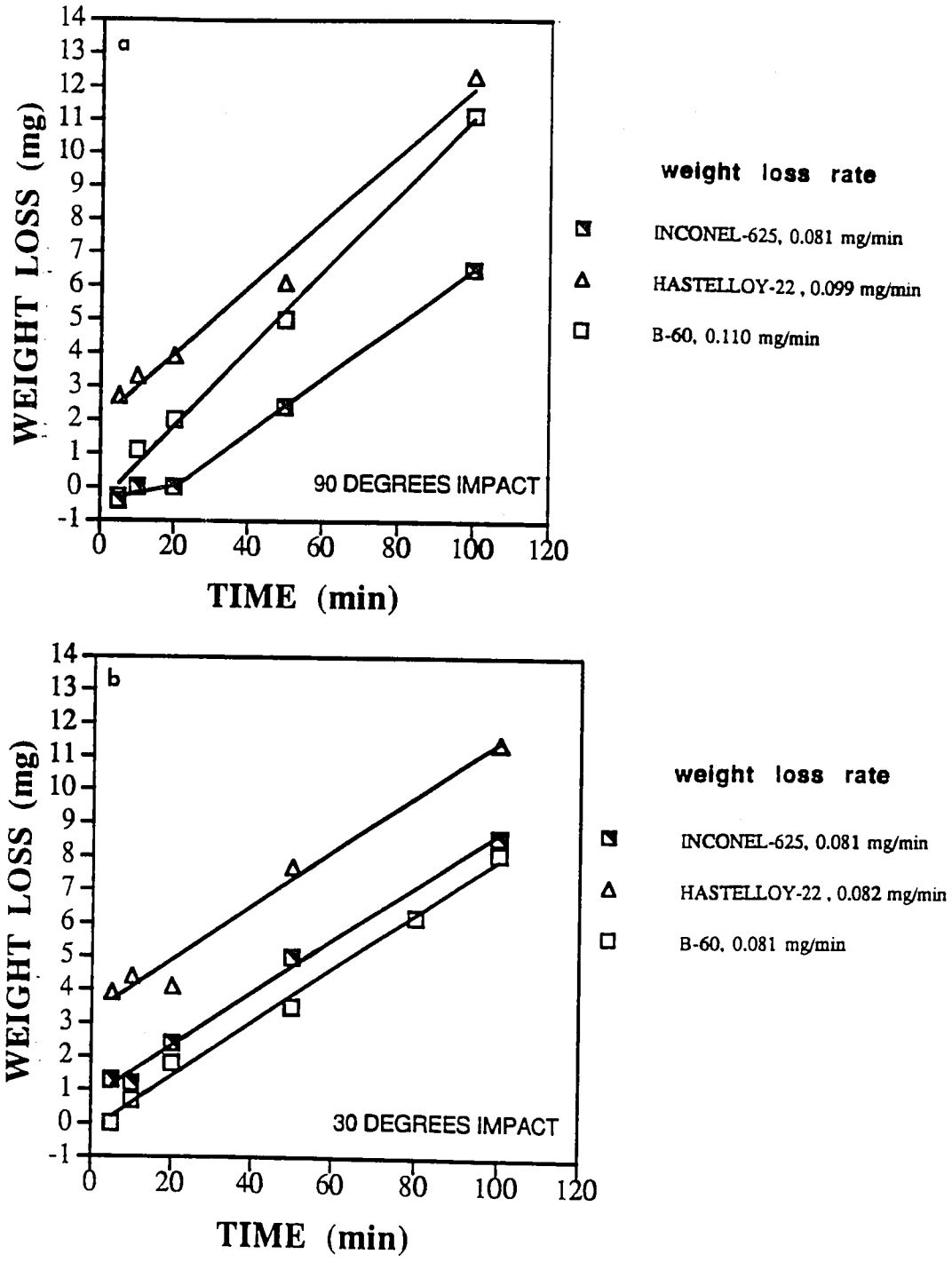

Figure 31. Weight loss as a function of time for nickel-base weld overlay coatings; (a) 90° impact angle; (b) 30° impact angle.

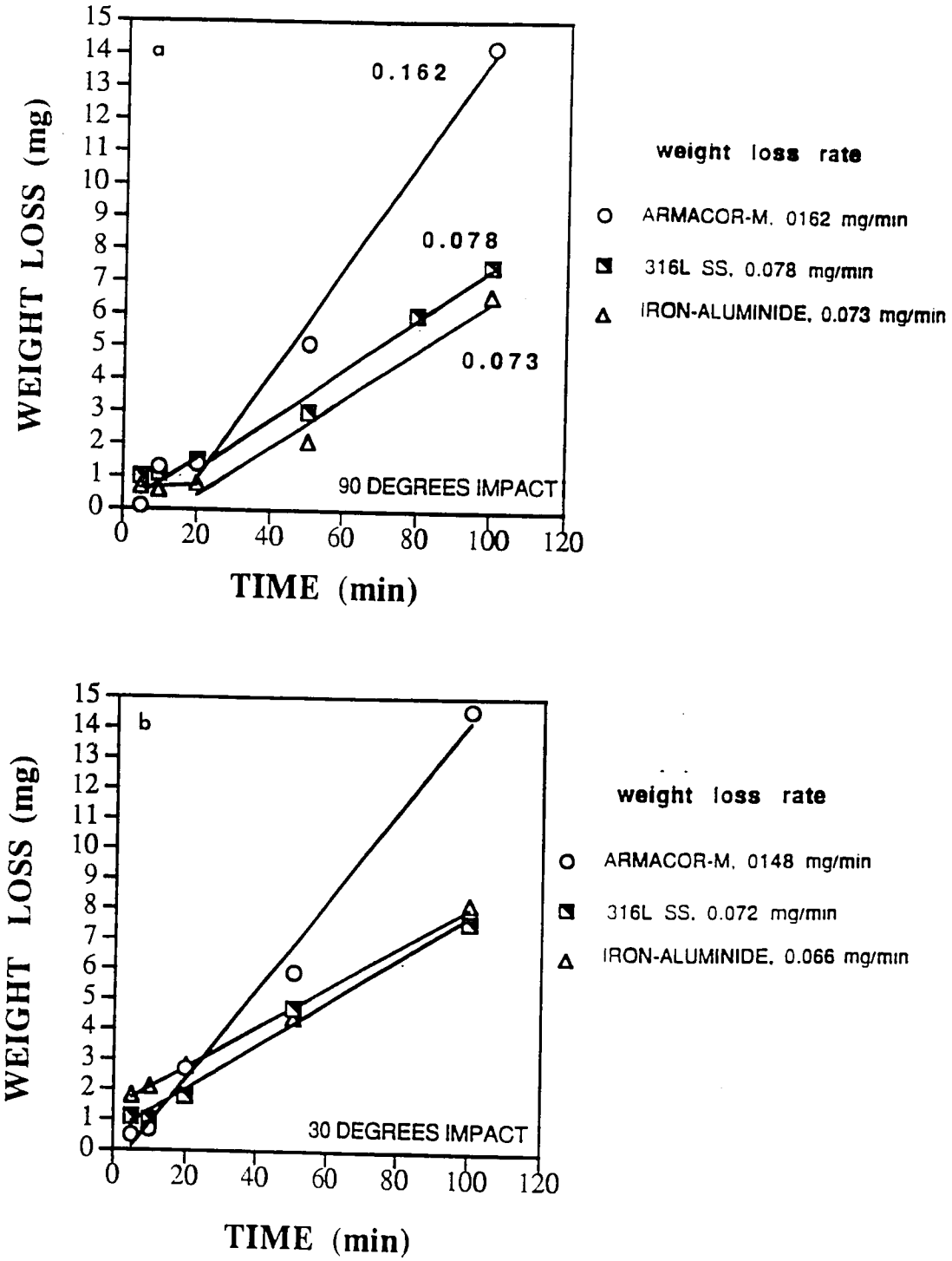

Figure 32. Weight loss as a function of time for iron-base weld overlay coatings; (a) 90° impact angle; (b) 30° impact angle.

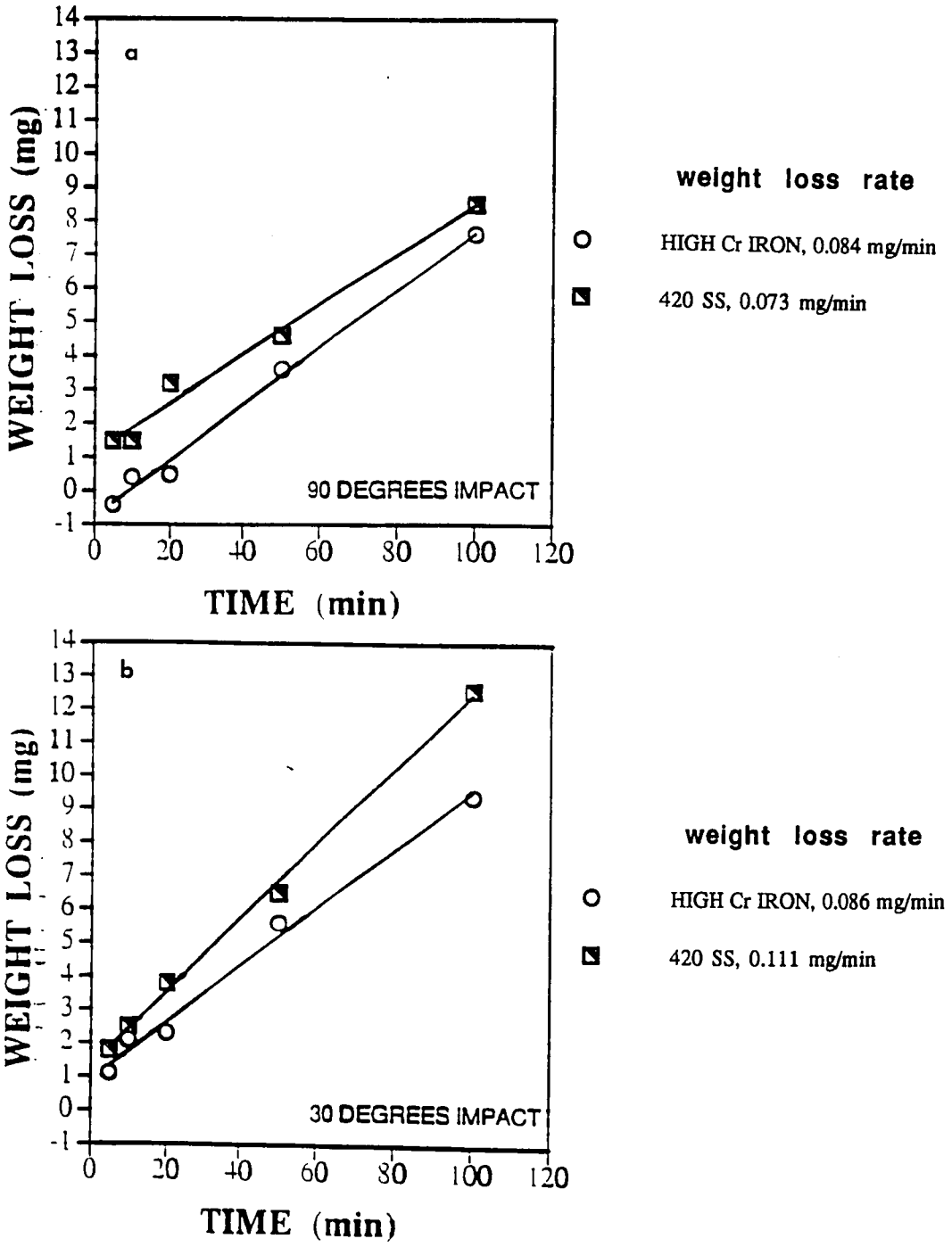

Figure 33. Weight loss as a function of time for iron-base weld overlay coatings; (a) 90° impact angle; (b) 30° impact angle.

and 420 SS coatings showed the highest steady state erosion rates (0.148 and 0.111 mg/min, respectively) at 30° impact angle (Figure 32b and 33b respectively). The 316L SS and Iron-Aluminide weld overlay coatings exhibited the lowest steady state erosion rates (0.072 and 0.066 mg/min) at 30° impact angle. The High Chromium Iron weld overlay coating showed a moderate steady state erosion rate (0.086 mg/min) at 30°.

IV.B.4. Relative Ranking Of The Weld Overlay Coatings

The relative ranking of the coatings at 400°C based upon their combined average of volumetric erosion rates (mm^3/min) for 90° and 30° impact angles is shown in Table 9. The volumetric erosion rates for each weld overlay were obtained by dividing the steady state weight loss rate by the density of the undiluted coating. It should be noted that due to the dilution, densities of the coating could change. However, it was calculated that maximum change in coating densities associated with 10 to 30% dilution (typical for PTA process) did not exceed 4%. Therefore, dilution is not expected to introduce significant error in the calculation of the volumetric erosion rate. It is essential to determine volumetric erosion rates in order to make a comparison of the erosion resistance of materials with different densities. In addition, the life time of the component that exposed to erosion is determined by its volume loss. It can be seen from Table 9 that considering both impact angles some weld overlays such as Ultimet, Inconel-625 and 316L SS exhibited steady state erosion rates which were significantly lower than the erosion rate of the remaining coatings.

Table 9. Relative ranking of the weld overlay coatings based upon their combined average volumetric erosion rates.

WELD OVERLAY COATINGS	EROSION RATE (mm^3/min) x 1000	
	90° impact angle	30° impact angle
ULTIMET	8.5	9.7
INCONEL-625	9.4	9.5
316L SS	10.0	9.2
HASTELLOY-22	11.4	9.4
IRON-ALUMINIDE	11.0	10.0
HIGH Cr IRON	11.1	11.3
TS-2	10.4	12.5
B-60	13.5	9.9
420 SS	9.4	14.2
STELLITE-6	11.9	12.2
ARMACOR-M	22.2	20.3

IV.B.5. Erosion Tests For Wrought Materials

In order to compare the erosion behavior of the weld overlays (dendritic microstructure), with the erosion behavior of wrought materials (equiaxed grains microstructure), erosion tests were performed at 400° for the following wrought materials: 316L stainless steel, Inconel-625, and Iron-Aluminide. The microstructures of these alloys in wrought and weld form are shown in Figures 21, 24 and 27. Erosion test conditions were kept the same as for the weld overlays (section III.E.2.). However, the erosion tester screw fitter and acceleration tube were redesigned before the wrought material tests. As a result of this, the particle feed rate could be different from the feed rate that was used for the erosion tests of the weld overlays. As a result, direct comparison between the erosion test results for welded and wrought materials might involve an error associated with differences in test conditions. In order to make a valid comparison between the erosion resistance of the wrought and welded materials, the erosion tests were also performed for 316L SS and Inconel-625 weld overlays on the redesigned erosion tester.

The erosion kinetics for 316L SS wrought and weld alloys at 90° and 30° impact angles are shown in Figure 34. The slopes of the best-fit straight lines through the data points are also shown on the graph. The slopes of these lines give the steady state erosion rate in milligram per minute (mg/min). It can be seen that the wrought alloy showed a lower steady state erosion rate at 90° than the weld alloy (0.052 mg/min and 0.061 mg/min, respectively). However, at a 30° impact angle the wrought alloy showed a higher steady state erosion rate than the weld alloys (0.085 mg/min

versus 0.071 mg/min). In contrast, the differences between erosion rates of 316L weld overlay at 30° and 90° (0.071 mg/min and 0.061 mg/min, respectively) were not as significant as for the wrought alloy (0.085 mg/min and 0.052 mg/min, respectively). Similar observations were made for the Inconel-625 alloy (Figure 35). For the Inconel-625 wrought alloy, the steady state erosion rate is significantly lower at 90° than at 30° (0.051 mg/min and 0.079 mg/min, respectively). However, the erosion rates for weld overlay at 90° and 30° were similar (0.067 mg/min and 0.060 mg/min, respectively). The erosion kinetics of the Iron-Aluminide wrought alloy is shown in Figure 36. The erosion rates were found to be 0.048 mg/min and 0.044 mg/min at 90° and 30° impact angle, respectively.

The volumetric erosion rates in mm^3/min at 400°C for 316L, Inconel-625 and Iron-Aluminide wrought and weld alloys are shown in Table 10. It can be seen that, Inconel-625 wrought alloy showed the lowest erosion rate at 90° impact angle, while Iron-Aluminide wrought alloy showed the lowest erosion rate at 30° impact angle. Also, Inconel-625 and 316L weld overlays showed superior erosion resistance at 30° impact angle when compared with the same wrought alloys.

IV.C. PLASTIC DEFORMATION MEASUREMENTS

Microhardness tests were performed for all weld overlay coatings after 100 min exposure in the erosion tester at 90° impact angle in order to determine the size of the plastically deformed region beneath the eroded surface. The experimental procedure for these measurements was described in section III.F.2. The results of are shown in

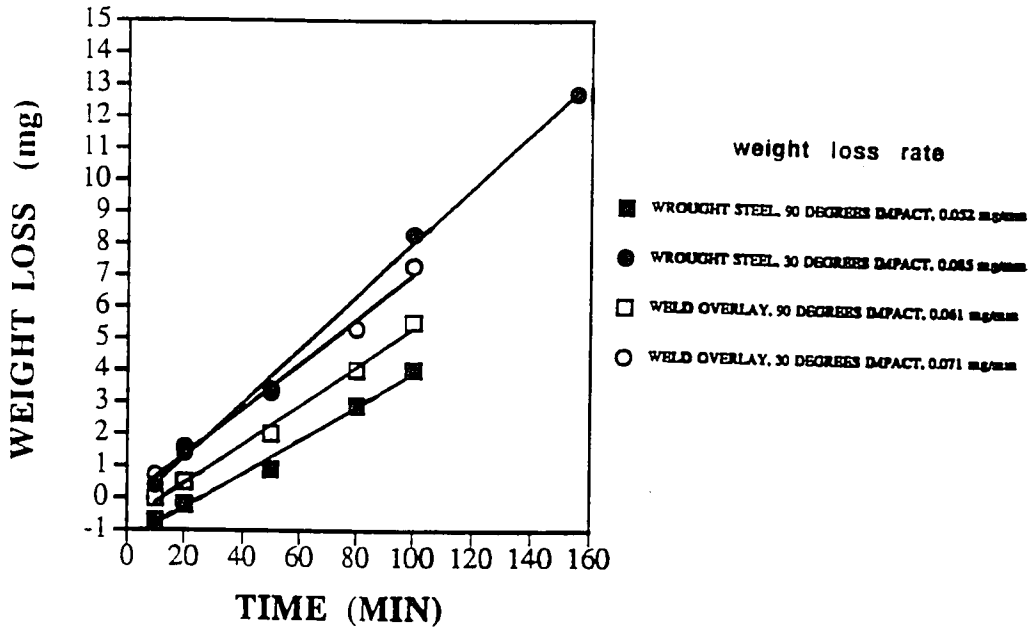

Figure 34. Weight loss as a function of time for 316L SS wrought and weld alloys.

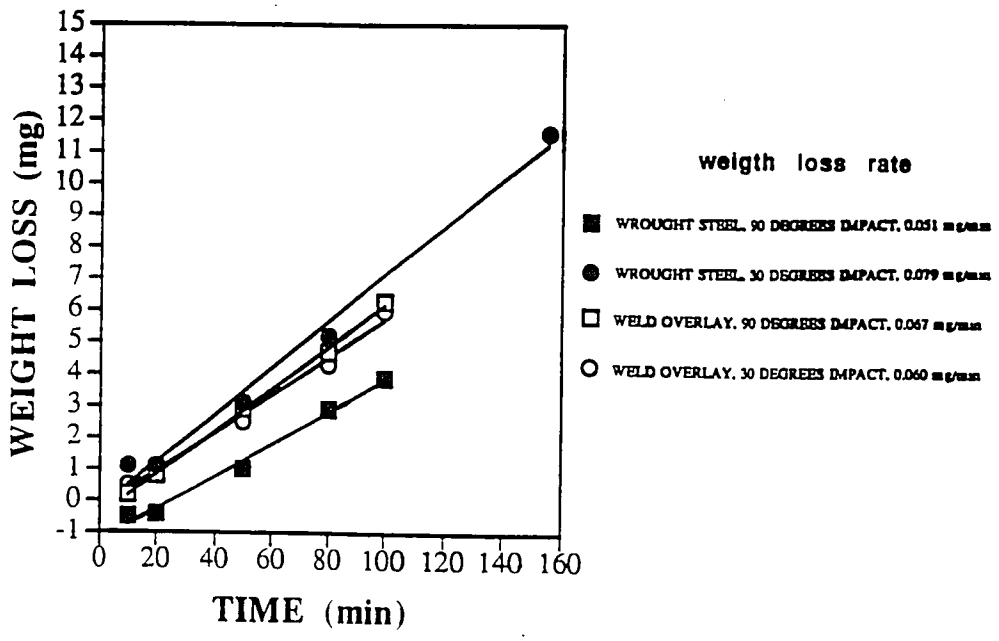

Figure 35. Weight loss as a function of time for Inconel-625 wrought and weld alloys.

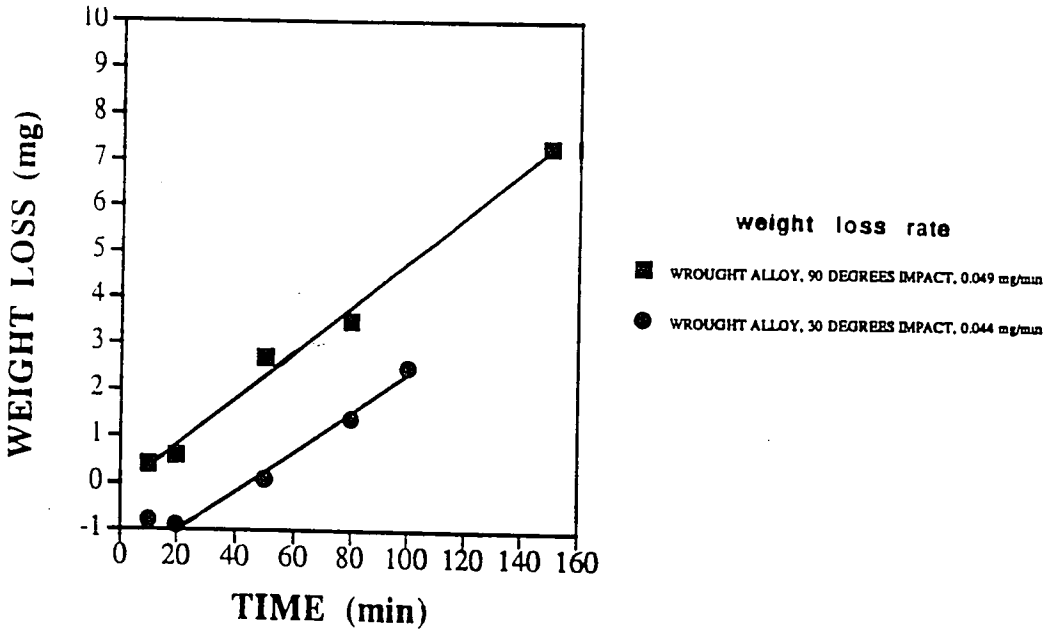

Figure 36. Weight loss as a function of time for Iron-Aluminide wrought alloy.

Table 10 . The volumetric erosion rates for alloys in the wrought and weld forms.

ALLOY	VOLUME EROSION RATE(mm^3/min) x10^3	
	90°	30°
INCONEL-625		
WROUGHT	6.0	9.4
WELD	7.9	7.1
316L SS		
WROUGHT	6.7	10.9
WELD	9.1	7.8
IRON-ALUMINIDE		
WROUGHT	7.4	6.7

Figure 37 (a-k). It can be seen that for some coatings (Ultimet, Inconel-625, 316L SS,Hastelloy-22, Iron-Aluminide, and Stellite-6), hardness significantly increases in the vicinity of the eroded surface (Figure 37 a-f). These results indicate the formation of the plastically deformed zone due to particle impact. During the particle impacts, the coating is plastically deformed and therefore the dislocation density increases in the vicinity of the impact, producing an increase in hardness at the coating surface. However, for Armacor-M, B-60, 420SS, TS-2 and High Chromium Iron coatings (Figure 37 g-k), no work hardening zone could be detected. It should be noted that the resolution of the microhardness measurements is 10 to 20 um. Although for these alloys no work hardening zone was detected at a distance of 10-20 um or more, it is possible that some plastic deformation could have occurred within first 10-20 um from the eroded surface. However, it is beyond the resolution limit of the microhardness technique to make a hardness measurements within this zone. Even if the deformation of these alloys occurred within first 10 to 20 um from the eroded surface, the size of plastic zone is considerably smaller than for the remaining coatings. The results of the microhardness tests for the 316L SS, Inconel-625, and Iron-Aluminide wrought materials are shown in Figure 38 (a-e). It can be seen that these alloys also deformed plastically as a result of the particle impacts.

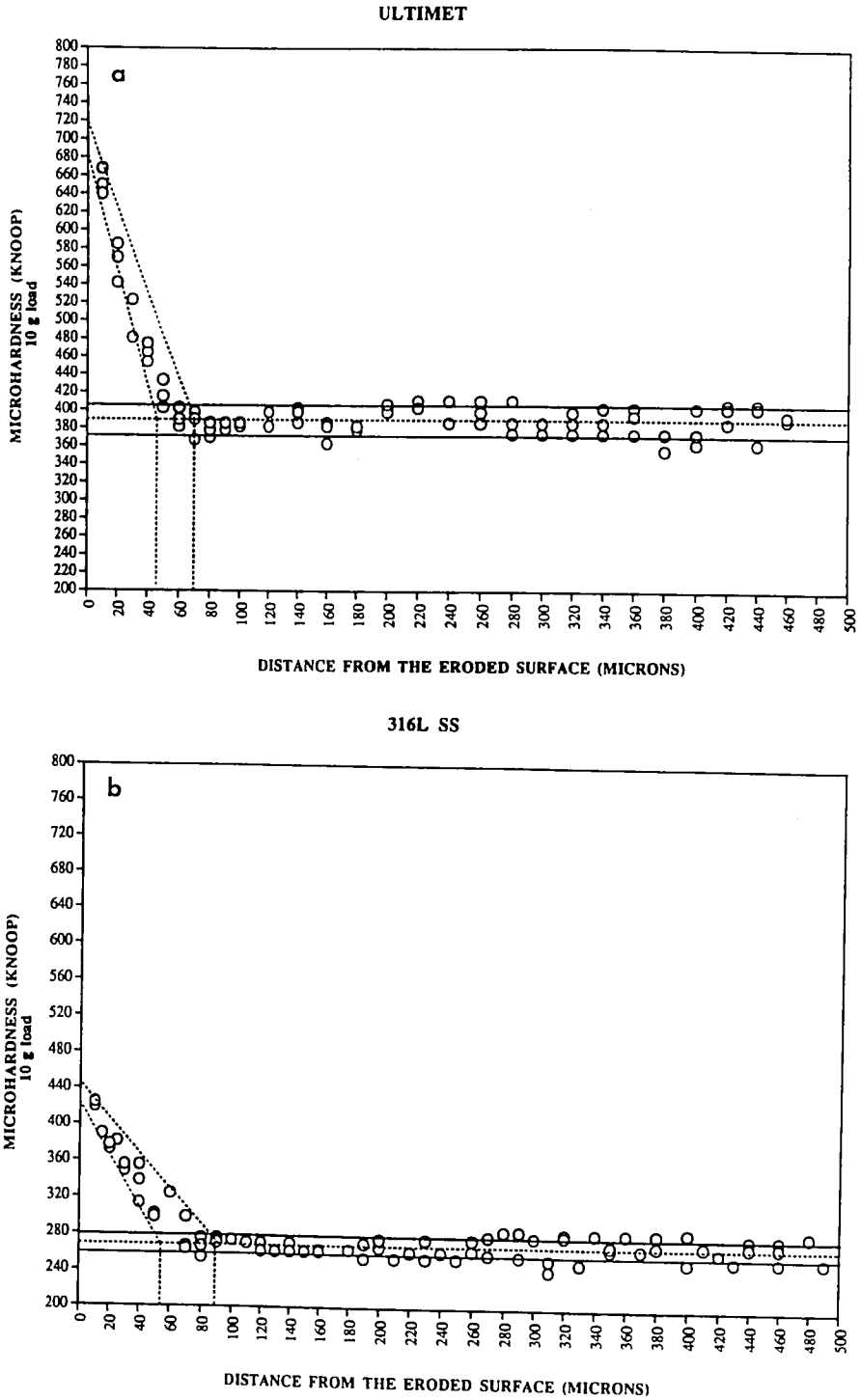

Figure 37 (a and b). Microhardness profiles for weld overlay coatings after 100 minutes of exposure in erosion tester at 90° impact angle.

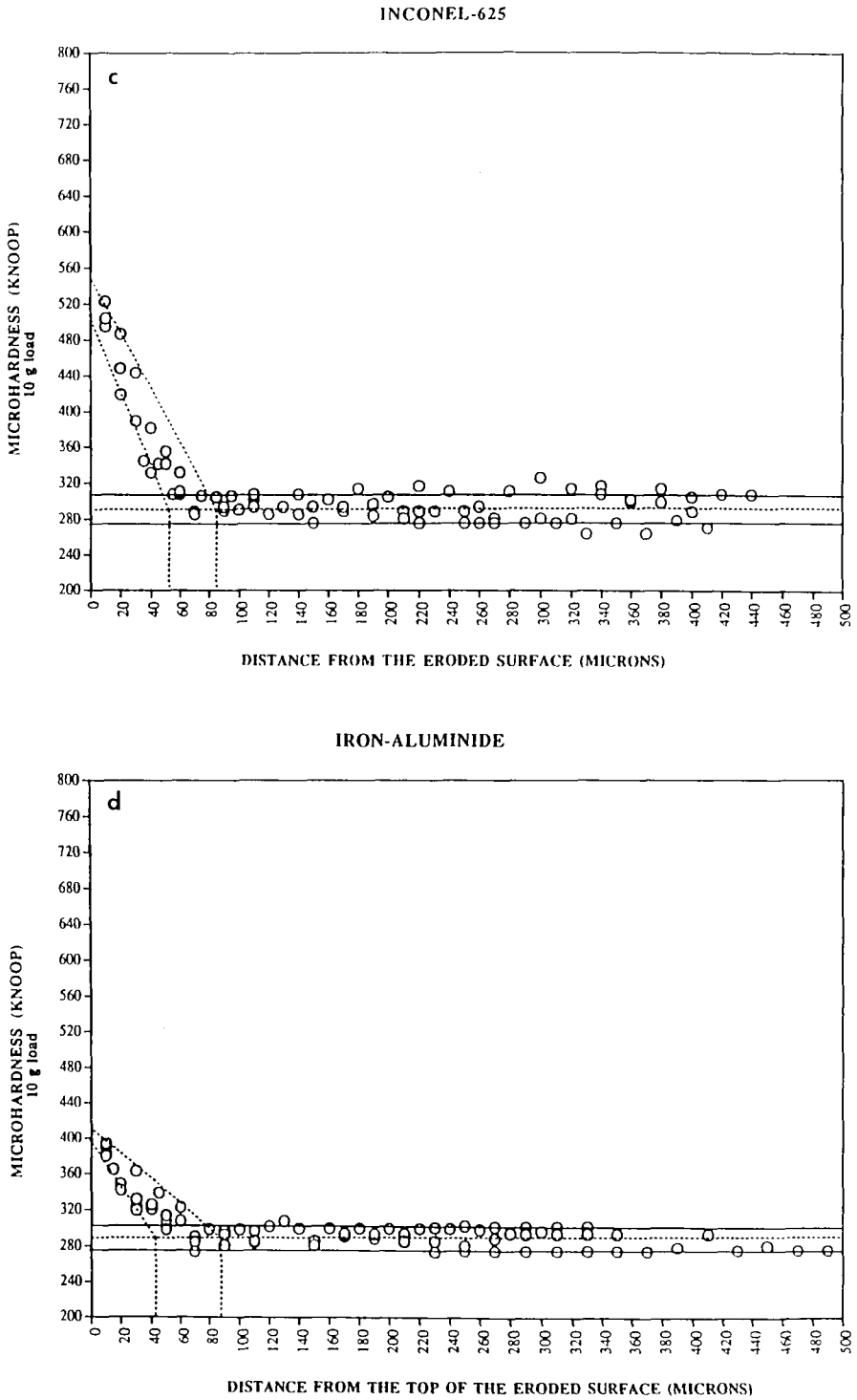

Figure 37 (c and d). Microhardness profiles for weld overlay coatings after 100 minutes of exposure in erosion tester at 90° impact angle.

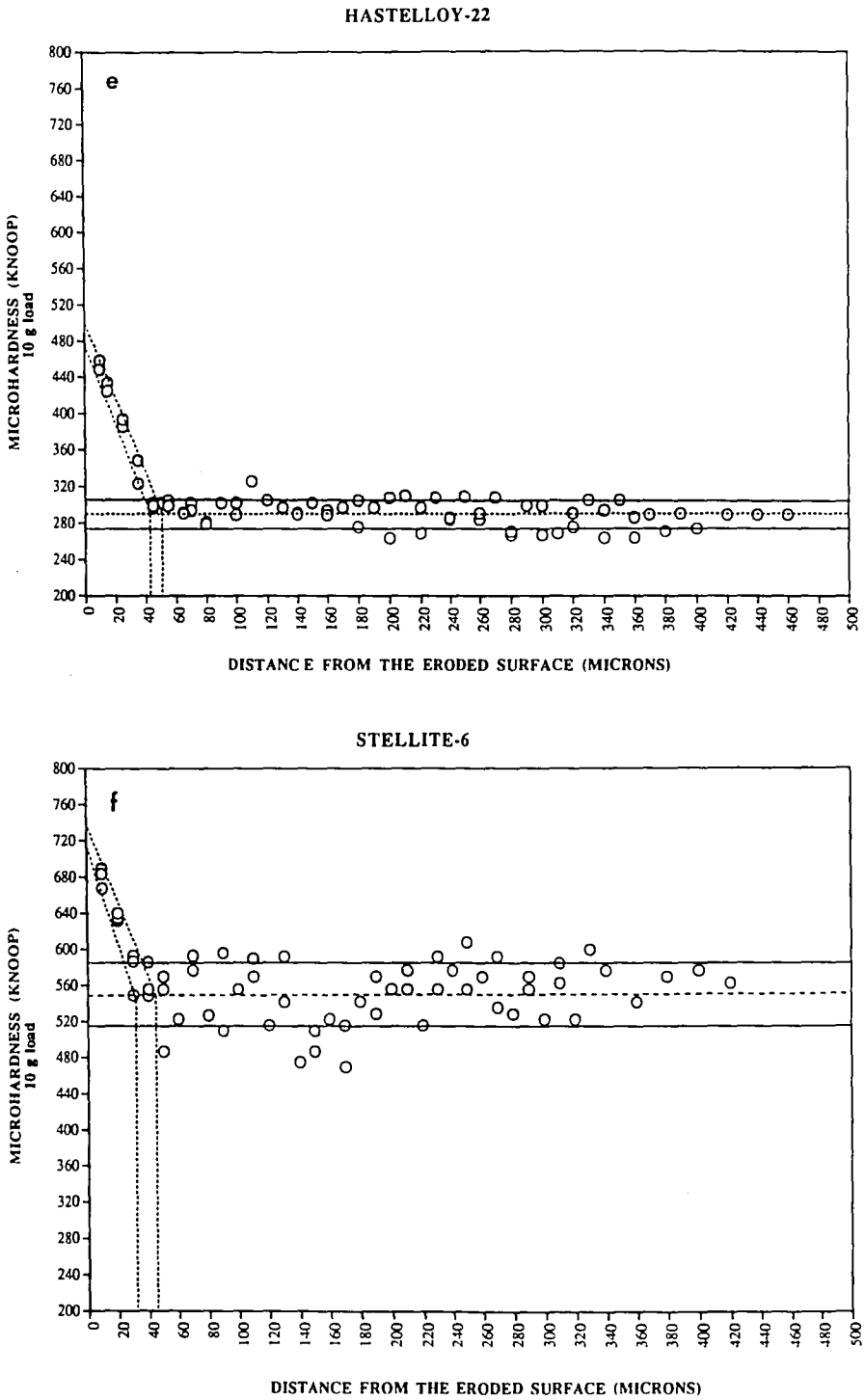

Figure 37 (e and f). Microhardness profiles for weld overlay coatings after 100 minutes of exposure in erosion tester at 90° impact angle.

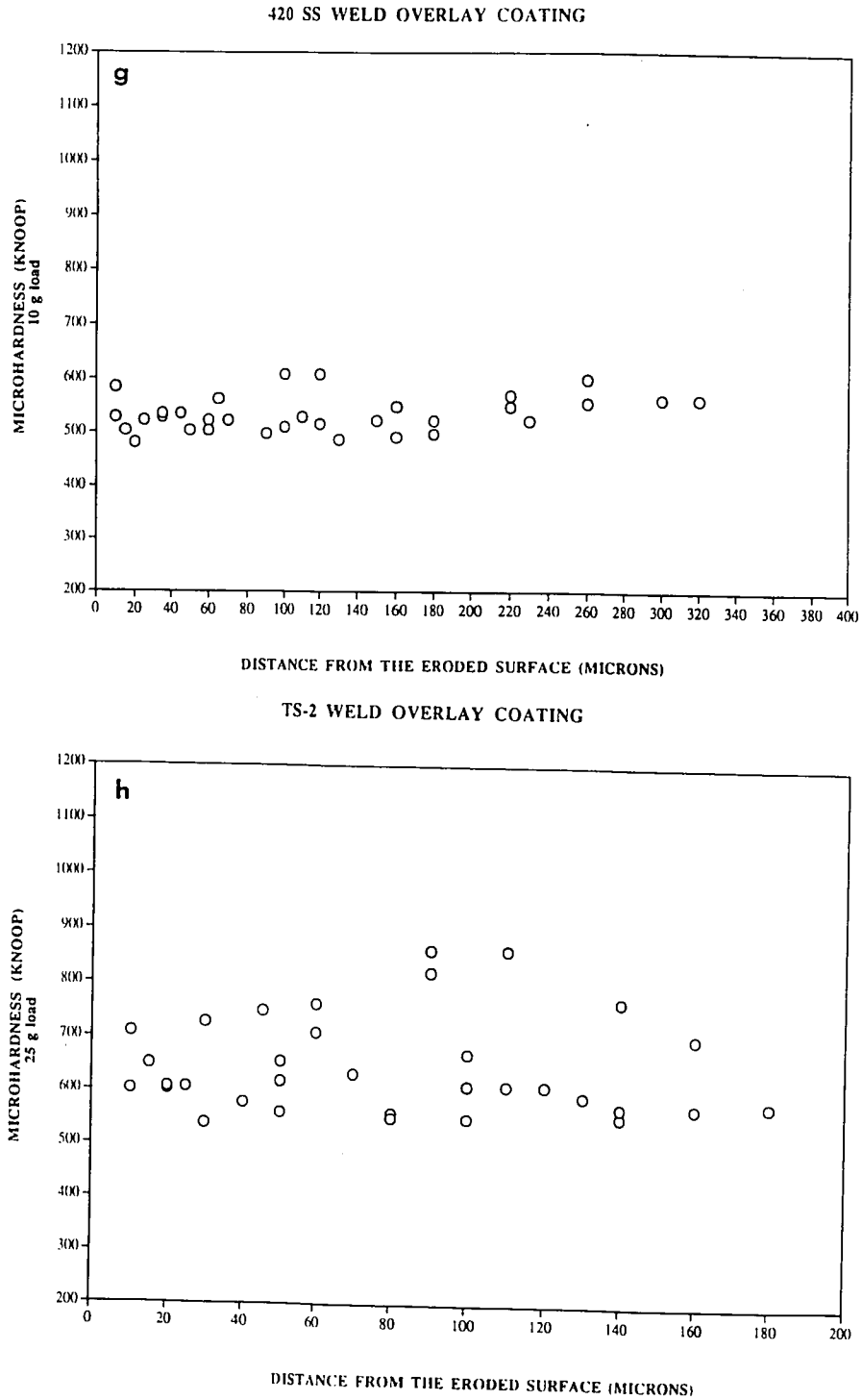

Figure 37 (j and h). Microhardness profiles for weld overlay coatings after 100 minutes of exposure in erosion tester at 90° impact angle.

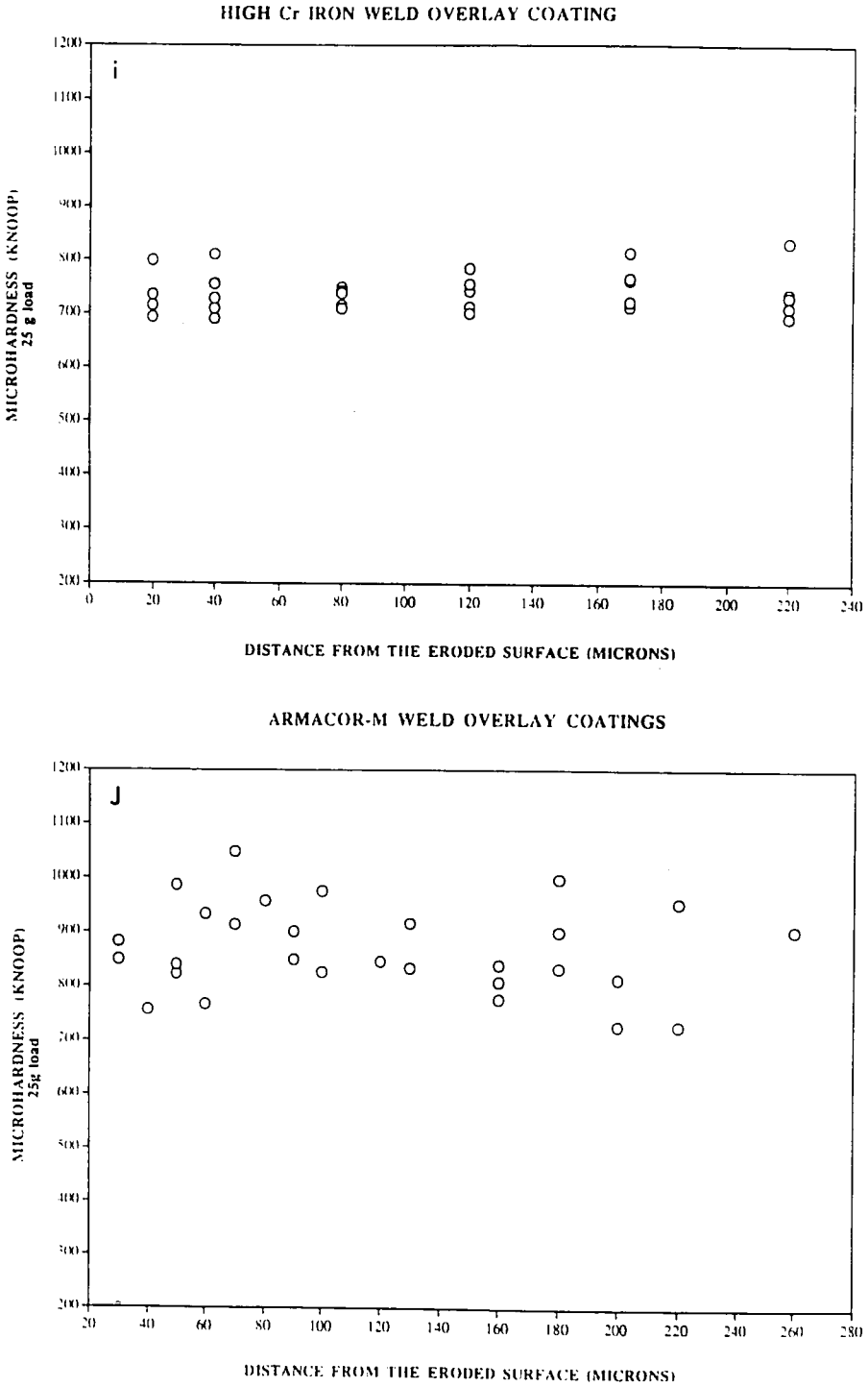

Figure 37 (i and j). Microhardness profiles for weld overlay coatings after 100 minutes of exposure in erosion tester at 90° impact angle.

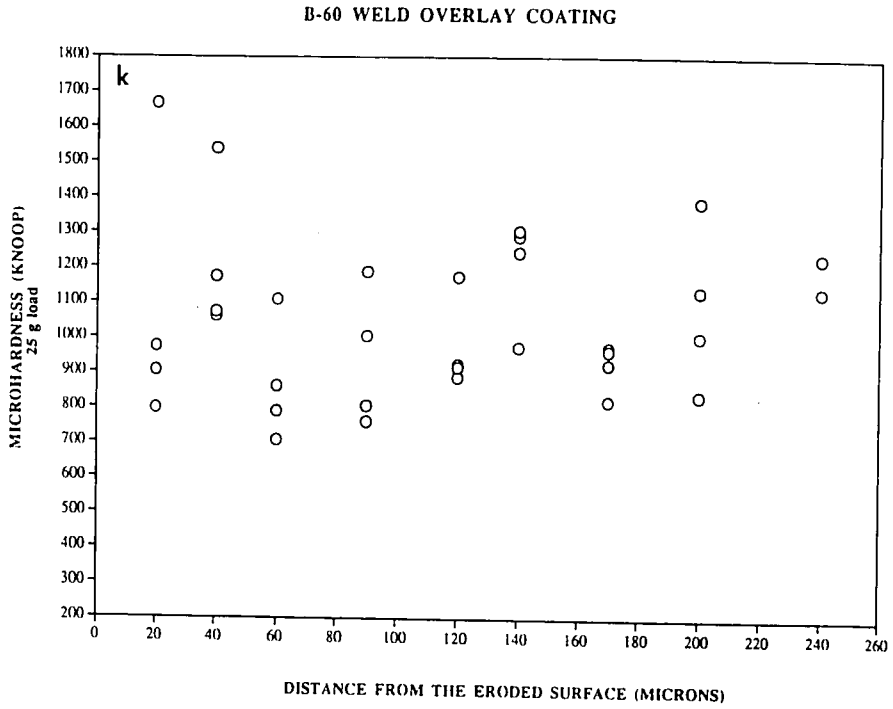

Figure 37 k. Microhardness profiles for weld overlay coatings after 100 minutes of exposure in erosion tester at 90° impact angle.

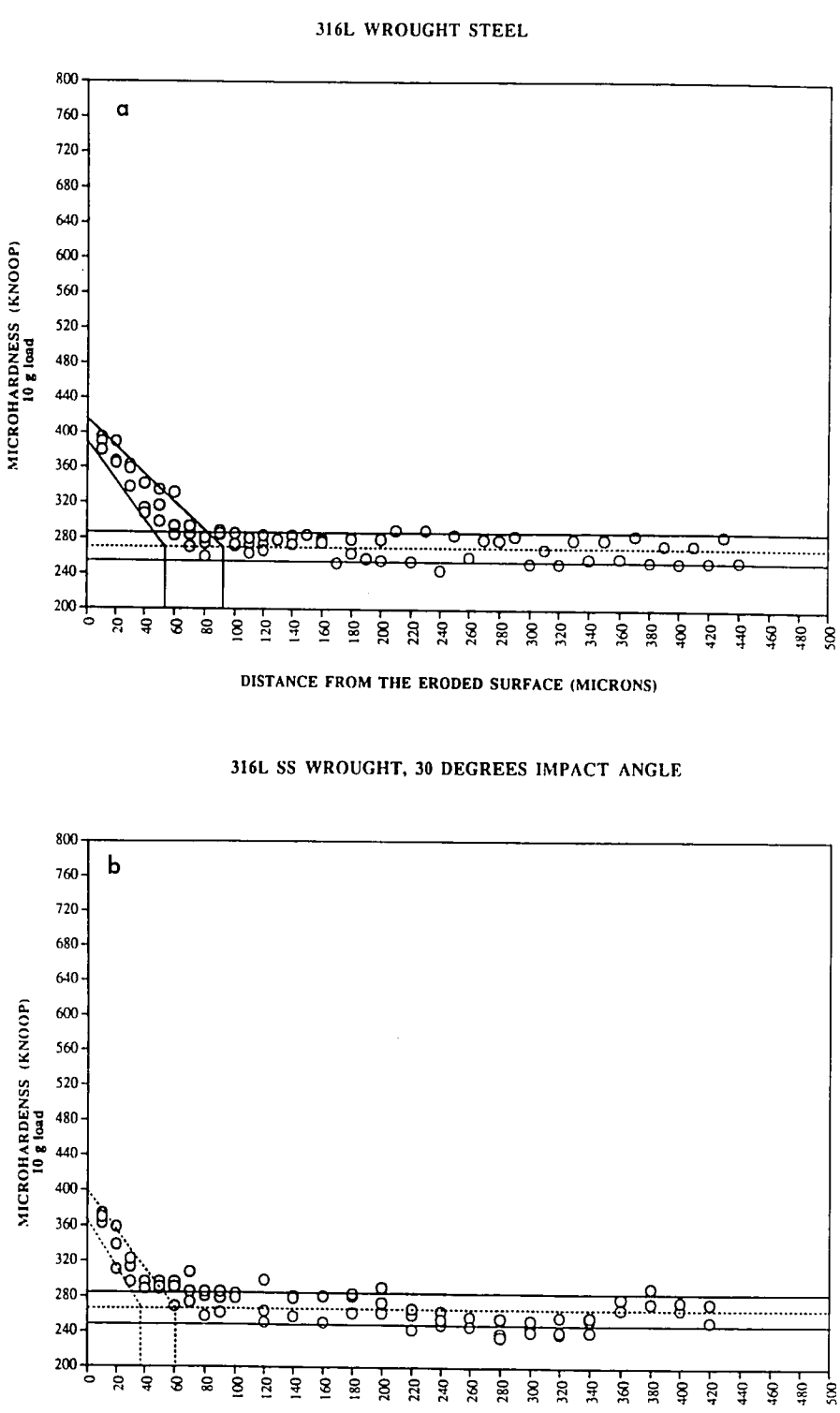

Figure 38 (a and b). Microhardness profiles for 316L SS wrought alloy after 100 minutes of exposure in erosion tester; (a) 90° impact; (b) 30° impact.

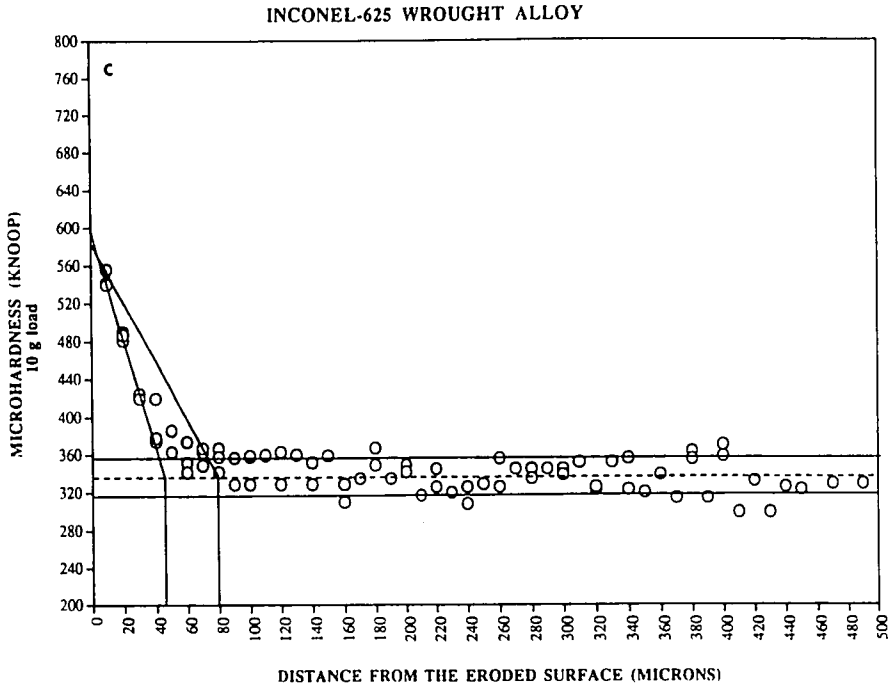

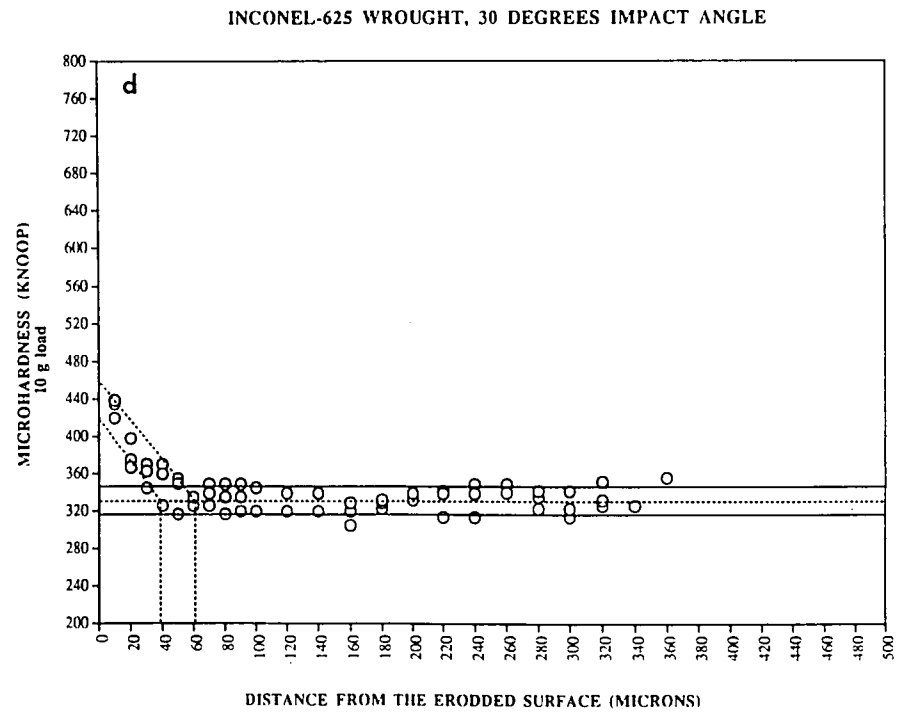

Figure 38 (c and d). Microhardness profiles for Inconel-625 wrought alloy after 100 minutes of exposure in erosion tester; (a) 90° impact; (b) 30° impact.

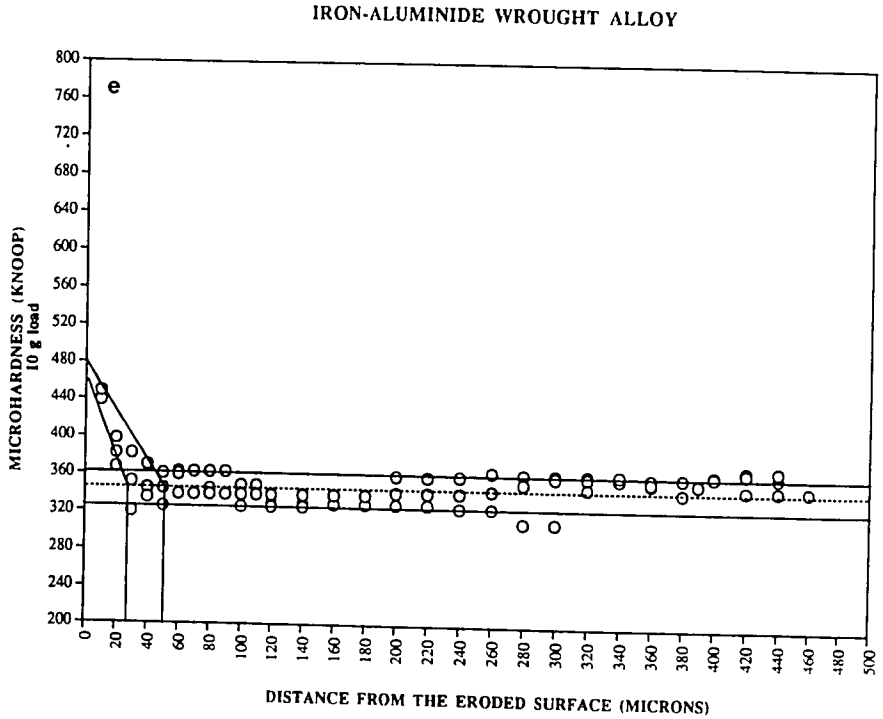

Figure 38 (e). Microhardness profile for Iron-Aluminide wrought alloy after 100 minutes of exposure in erosion tester at 90° impact angle.

V. DISCUSSION

V.A. EROSION RESISTANCE RANKING OF THE WELD OVERLAY COATINGS.

Based upon erosion test results, the relative ranking of the weld overlay coatings has been developed (Table 9). It can be seen that at both impact angles some weld overlays such as Ultimet, Inconel-625, and 316L SS exhibited steady state erosion rates which were significantly lower than the erosion rates of the remaining coatings. In addition, weld overlays such as 420 SS, B-60, and Hastelloy-22 also exhibited similar low erosion rates but only at one impact angle (90° or 30°). These results are rather surprising considering that the coatings have different chemical compositions and microstructures. Also, alloys that are commercially used for abrasion protection such as Stellite-6, B-60, and Armacor-M showed relatively poor erosion resistance at 90° or 30° impact angles compared with Inconel-625 and 316L SS coatings that are used primarily for corrosion protection.

These results suggests that the mechanisms of abrasion and erosion wear are different. The impact velocity of an erosive particle is about two to three orders of magnitude higher than the sliding velocity of abrasive particles [53]. As a result, the erosive particle impact produces more localized strain in the material per impact compared with sliding abrasive particles. Therefore, the strain to fracture is achieved in a shorter period of time under erosive wear conditions. In addition, the high strain rate due to erosion may lower the value of the critical strain to fracture [53]. Since the mechanisms involved in abrasion

and erosion wear are different, the effect of mechanical and physical properties on abrasion and erosion resistance are also expected to be different. For example, some brittle materials with a high hardness show excellent abrasion resistance because the energy of the abrasive particles is not sufficient to cause brittle fracture. In this case, hardness may be a major factor that contributes to increased abrasion resistance. On the other hand, during solid particle erosion of the same material, it may fracture as a result of high strain rates imposed by the particle impacts. Therefore, hardness does not contribute significantly to the erosion resistance. Moreover, the fracture toughness of brittle materials may have a great affect on its erosion resistance because of its contribution to the materials resistance to brittle fracture. It is evident that selection of an erosion resistant weld overlay can not be based upon abrasion resistance.

The present investigation indicates that, in spite of the differences in microstructure and composition, some coatings showed similar erosion rates at elevated temperature (i.e. Inconel-625 and 420 SS at 90°). The results of the plastic deformation measurements (section IV.D.) showed that Ultimet, Inconel-625, 316L SS, Iron-Aluminide, Hastelloy-22, and Stellite-6 coatings appreciably deformed plastically as a result of erosion, while 420 SS, B-60, Armacor-M, High Cr Iron, and TS-2 did not. This suggests that these two groups of coatings may undergo different erosion mechanisms (i.e. ductile versus brittle) and, as a result, different mechanical properties may control the erosion resistance of these weld overlay groups. Therefore, coatings from each group that have similar low erosion rates may attain these similarities by having optimal mechanical properties (different for each group) that contribute to their erosion resistance. The critical

mechanical properties that are thought to control erosion resistance include hardness [2], toughness [7], ductility [12] and strain hardening coefficient [20].

V.B. EROSION MECHANISMS AND FACTORS CONTRIBUTING TO EROSION RESISTANCE

V.B.1. BRITTLE MATERIALS

The volumetric erosion rate of each coating at 90° impact angle is plotted against the average microhardness at 400°C in Figure 39 (a and b). There is no correlation between hardness and steady state erosion rate at 400°C for coatings that were deformed plastically ("ductile" coatings), figure 39b. However, for weld overlays that did not significantly deform plastically at a 90° impact angle ("brittle coatings"), an increase in coating hardness lead to an increase in their volumetric erosion rates (420 SS, TS-2, High Cr Iron, B-60, Armacor-M). The erosion of materials that do not appreciably deform plastically may involve brittle fracture (i.e. chipping, cracking) after particle impact. For these materials, the ability to resist brittle fracture is a major factor that may contribute to erosion resistance. It was documented [7,54] that for brittle materials, an increase in hardness leads to a decrease in toughness and as a result, the resistance to brittle fracture is decreased. Therefore, for coatings that did not appreciably deform plastically, an increase in hardness may have lead to a decrease in their toughness and, as a result, their erosion resistance decreased.

In order to explain the effects of hardness and fracture toughness on erosion resistance of relatively brittle weld overlays, one should consider two types of possible

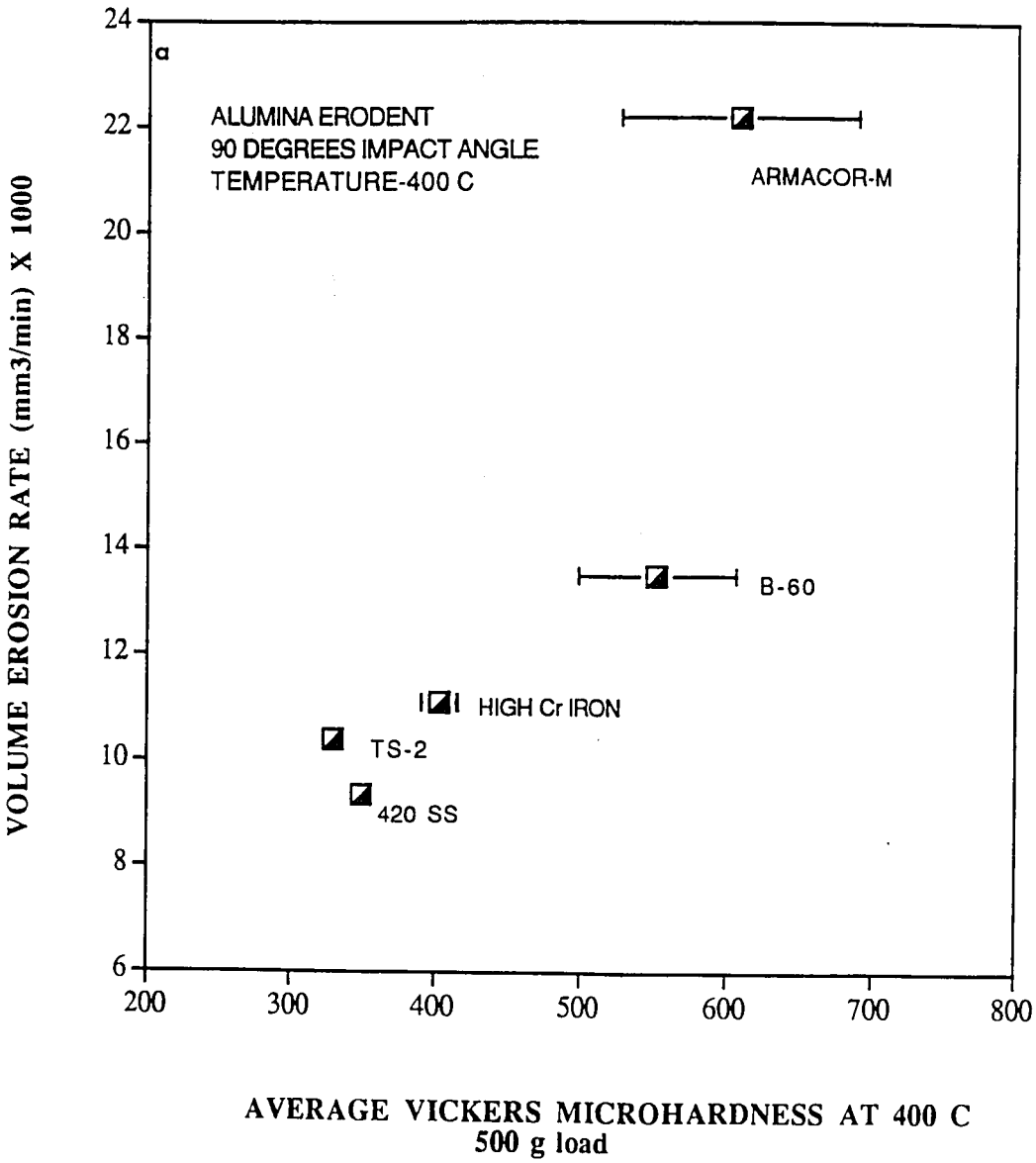

Figure 39a. Effect of average microhardness at 400°C on volume erosion rates at 400° for weld overlay coatings that did not appreciably deform plastically.

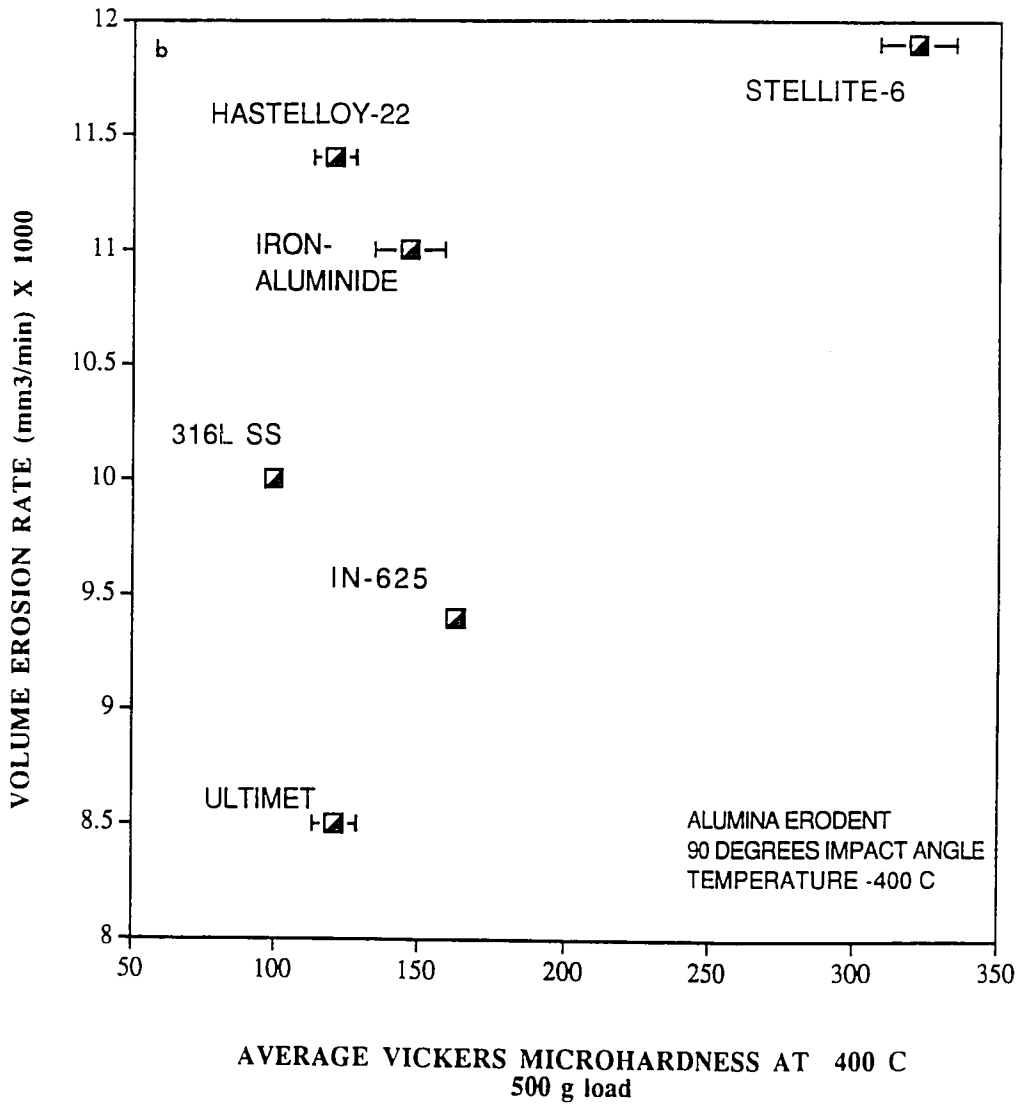

Figure 39b. Effect of average microhardness at 400°C on volume erosion rates at 400°C for weld overlay coatings that deformed plastically.

material responses to erosive particle impacts. **Type I (Elastic Behavior)** is associated with particle impacts that cause only elastic deformation. In this case, particle energy is not sufficient to cause immediate fracture due to the particle impact. However, material may still experience volume loss as a result of the fatigue processes which will lead to crack propagation under cyclic loading (multiple particle impact). Therefore, materials with a relatively high fracture toughness may offer good resistance to crack propagation and may exhibit low erosion rates. **Type II (Fracture Behavior)** material response to particle impact involves material volume loss that occurs by immediate crack formation and propagation upon particle impact (high particle impact energy). In this case, the volume erosion rate can be expected to be significantly higher than when only elastic deformation occurs. However, materials with high fracture toughness will still offer better erosion resistance than materials with low fracture toughness. If during the erosion experiments, erodent conditions such as velocity, feed rate, and size are kept constant (present investigation) the erodent impact energy is expected to be the same. In this instance, the mechanical properties of the target material may define a transition between Type I and Type II behavior. For most classes of materials an increase in hardness is associated with a decrease in toughness [7]. Therefore, the observed decrease in erosion resistance with hardness at 400°C for weld overlays that did not significantly deform plastically can be attributed to a decrease in their fracture toughness. However, this relationship is valid only if coating hardness is high enough to prevent plastic deformation due to erosion.

Apparently, the combination of high hardness to prevent plastic deformation and high

toughness to resist brittle fracture provides the best erosion resistance for brittle coatings. For example, it is anticipated that 420 SS coating, with a microstructure consisting of lath martensite and regions of austenite or ferrite (white phase, Figure 28) has a relatively high fracture toughness. For example, it was documented [55] that fracture toughness (K_{Ic})of the 403 martensitic stainless steel, which is similar to 420 SS, is approximately 80 MPa $m^{1/2}$. However, heat treatment conditions for this steel were not reported. In comparison, fracture toughness values (K_{Ic}) of High Chromium Cast Iron (similar to High Cr Iron weld overlay) vary from 10 to 35 MPa $m^{1/2}$ [56]. At the same time, 420 SS coating has a relatively high hardness at 400°C that provides a good resistance to plastic deformation. As a result, the 420 SS weld overlay showed the best erosion resistance at 400°C for 90° impact angle among the coatings that did not appreciably deform plastically. One should remember that for a given erosion test condition (constant impact energy), depending upon the material fracture toughness and hardness, the material may deform elastically (**Type I behavior**) as a result of particle impact or it may fracture (**Type II behavior**). Therefore, when comparing the erosion rates of different materials, it is important to determine whether all of the materials are in the same erosion regime or not. If the impacting particles have the same sizes and shape, their velocity defines the critical impact energy that cause transition from Type I to Type II behavior for the same material. A schematic diagram that shows the effect of erodent velocity on erosion behavior of brittle materials is presented in Figure 40. The comparison of materials erosion resistance in regime I or II is possible, when critical velocity (V_c, figure 40) is determined. Clearly, for the same test conditions, materials that experienced elastic defromation will have a

lower erosion rate compared with materials that experienced immediate fracture upon particle impact. However, if the impact velocity increases, materials that showed Type I behavior may fracture upon impact and Type II behavior may be observed. In this case, the relative ranking of the materials might change. Nevertheless, for both types of erosion behavior, materials with high hardness and fracture toughness may offer good erosion resistance.

In spite of the inverse proportionality between hardness and fracture toughness, a certain level of high hardness is necessary to prevent plastic deformation. If the coating hardness is not high enough, it will deform plastically and the mechanism of erosion might change from fracture dominated to plastic deformation dominated. In materials that exhibit fracture dominated behavior ("brittle"), the particle impact energy transforms to the work needed to produce a new crack surface. But for materials that shows plastic deformation dominated behavior, particle impact energy transforms to the energy required to produce plastic deformation.

V.B.2. Ductile Materials

Based upon the results of the microhardness measurements (see section IV.D., Figure 37), it was established that Ultimet, Inconel-625, 316L SS, Iron-Aluminide, Hastelloy-22, and Stellite-6 coatings were deformed plastically during erosion ("ductile" materials). It was also found that Inconel-625, 316L SS, and Iron-Aluminide wrought alloys also plastically deformed during erosion. In the following sections, the factors that contribute to the erosion resistance of these materials will be discussed.

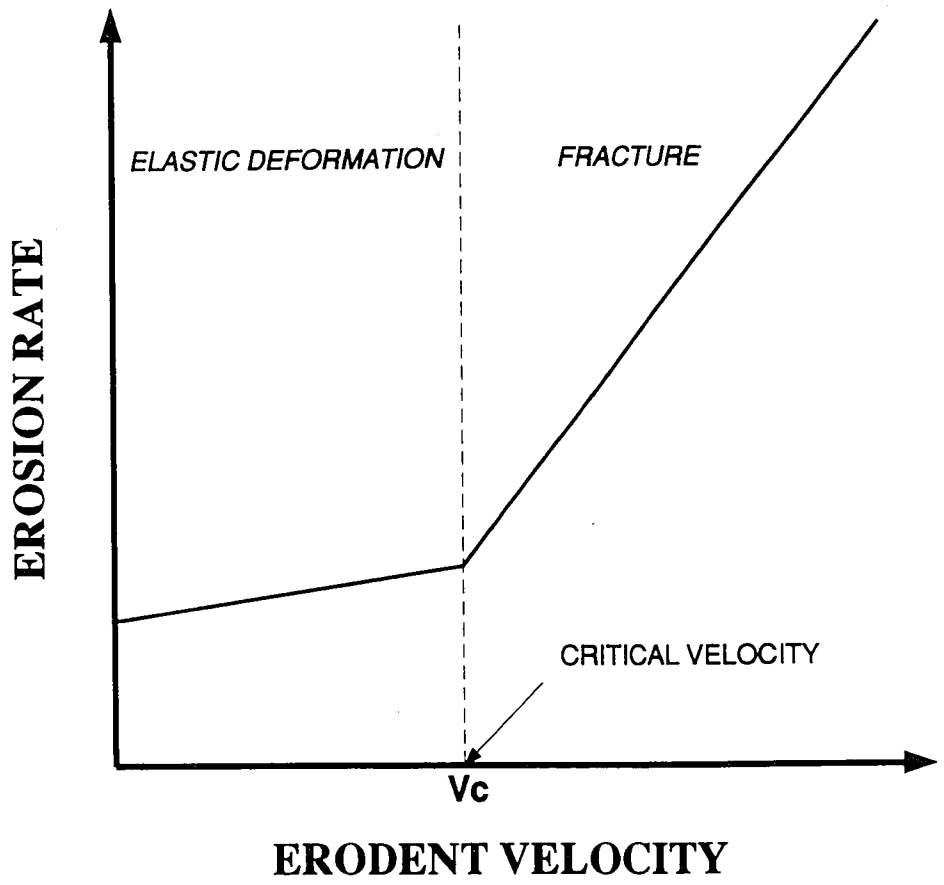

Figure 40. A schematic diagram that illustrate the effect of erodent particles veocity on erosion behavior of brittle materials

V.B.2.a. Determination Of The Area Under The Microhardness Profile Curve

The ability of a material to dissipate particle impact energy can be estimated by calculating the area under the curve of microhardness versus distance from the eroded surface curve. The area of this curve can be interpreted as a measure of the amount of energy that the material absorbs during particle impact before it reaches the critical stress for fracture. The analogy between the true stress-strain diagram and the microhardness profile curve after erosion may be appropriate. The area under the stress-strain diagram represents the amount of energy per unit volume that the material can absorb before fracture. For the microhardness profiles, hardness of the material can be correlated to its strength within a reasonable approximation. This relationship can be in the form of $H=A\sigma_y$, where H is hardness, σ_y is yield strength, and A is a constant [57]. A schematic illustration of the change in microhardness with depth below the eroded surface is shown in Figure 41. The microhardness profile curve represents the variation in strength beneath the eroded surface with strain that was imposed by particle impacts. The decrease in hardness with distance from the eroded surface is caused by a decrease in strain. Therefore, hardness versus distance from the eroded surface curve can be qualitatively correlated to the stress versus strain curve (see Figure 41). By analogy with the true stress-strain diagram, the area under this curve may be interpreted as a measure of the amount of energy that a material can absorb during erosion before it will fracture. It should be noted that this analogy between the true stress-strain diagram and the microhardness profile is only qualitative. The conventional stress-strain diagram is obtained by static loading at low strain rates. The microhardness profiles curves were

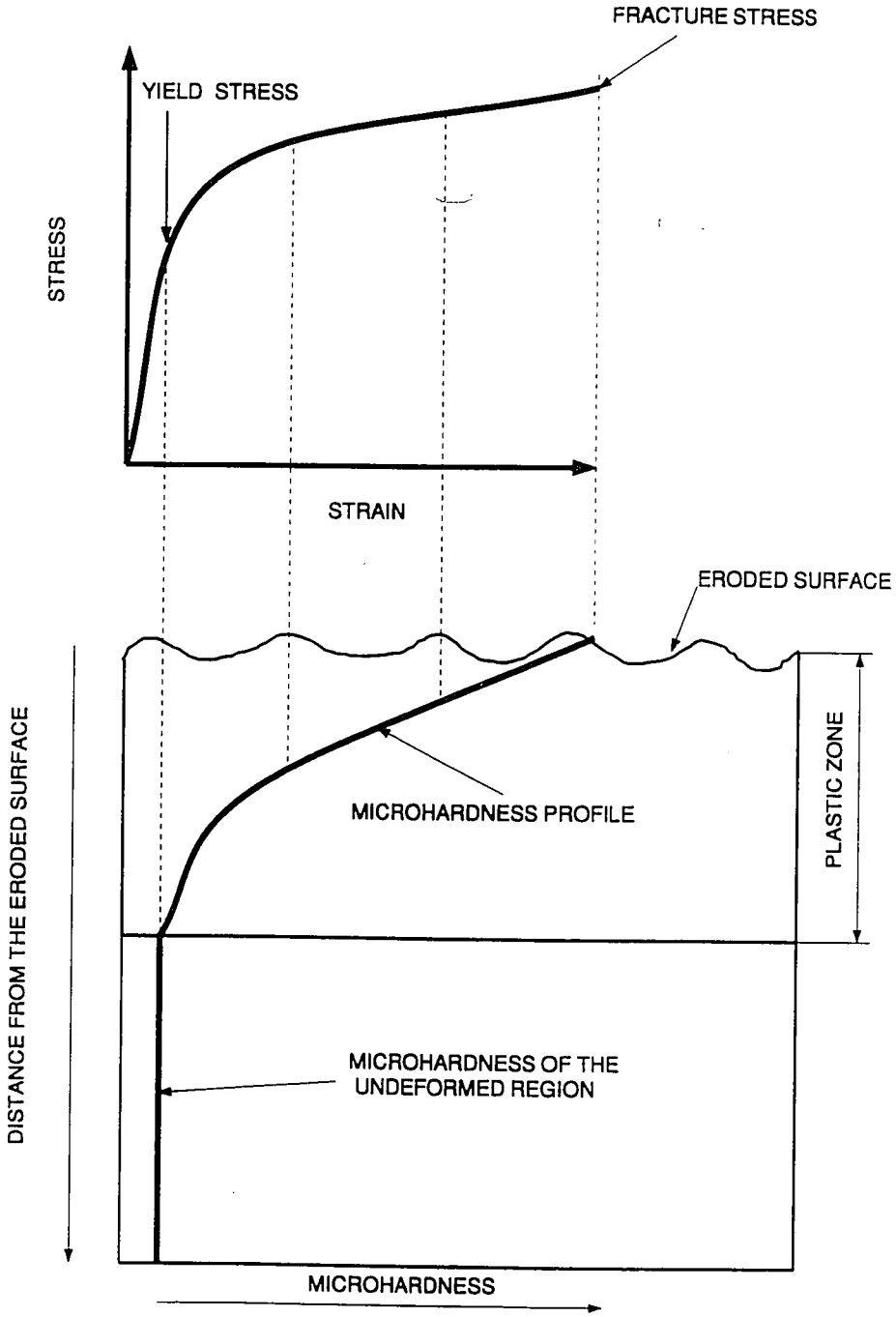

Figure 41. A schematic diagram of change in microhardness with distance from the eroded surface. Correlation between the drown true stress-strain diagram and microhardness profile is only qualitative.

obtained after particles impacts that impose a very high strain rates. Due to the large differences in strain rates, the true stress-strain diagram does not represent actual variations in stress with strain that may result from particle impacts.

A typical microhardness profile curve, showing the 316L weld overlay as an example, is presented in Figure 42. The data used to determine the average hardness of the undeformed material was taken from the region between 120 um and 500 um depth (line AF on Figure 42). This region was well below the depth of the plastic deformation. The standard deviation of the mean is given by the solid lines. Two lines were drawn that encompassed the data in the plastic zone region given by BD and CE on the Figure 42. These lines were drawn from the microhardness axis to the average hardness line of the material. The minimum and maximum area under the curve was found from calculating areas ABD and ACE, respectively ($Area_{ABD}$=0.5xAB xAD and $Area_{ACE}$=0.5xACxAE). From this data, an average area under the curve and a standard deviation were calculated.

It should be noted that two assumptions were made during calculation of the plastic zone size and area under the curve. First, microhardness values were extrapolated to the eroded surface, although the first indentation was made at a distance 10 um from the eroded surface. Indentations could not be made closer to the erosion surface because of a lack of sufficient supporting material on one side that would produce larger than actual indentations. Therefore, hardness measurements within first 10 um involve significant error. This extrapolation is justified, since it is clear that the hardness values are increased toward the eroded surface. Even if an error is introduced due to this approximation of the surface hardness, it will represent only a small region (10 um) and

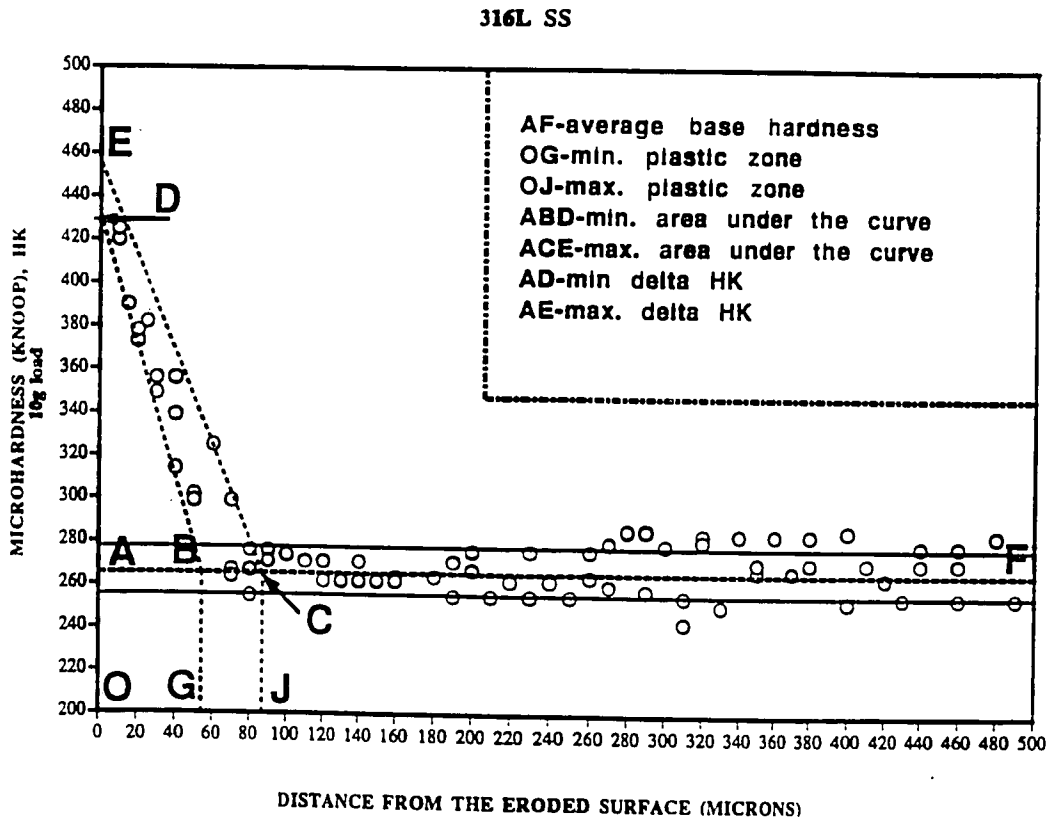

Figure 42. A typical example of the microhardness profile (316L SS Coating) from which area under the curve can be determined.

therefore, the area under the curve will not significantly change. The second assumption involves the lines that encompassed the plastic zone region (lines BD and CE). These lines were drawn straight and the area under the curves was calculated from the right angle triangles. The plastic zone region could also be described by curving these lines in a power law fit. However, this method would be highly subjective. It is believed that these assumptions would not change the relative comparison between plastically deformed regions of different materials.

V.B.2.b. Plastic Deformation In Steady State Erosion Regime

For all tested materials, the measurements of the plastically deformed region were made after 100 min exposure (longest time) in the erosion tester at 90° impact angle. The results of these measurements were employed to find a correlation with the volumetric steady state erosion rate. Steady state erosion is defined by the linear portion of the weight loss versus erosion time graph. It is widely accepted in the literature that in this region, the material experiences surface weight (or volume) loss and surface strain hardening at the same rates [2]. It is also hypothesized that the size of the plastically deformed region is constant in the steady state regime [5]. However, no evidence of this in the form of experimental observations were found in the literature. Thus, in order to make a valid link between plastic deformation measurements for samples in the steady state regime and erosion rate, it is essential to verify that, in this regime, the size of the plastically deformed region does not change with time. During the erosion experiments, all materials reached steady state after 5 to 20 min exposure. The microhardness profiles for 316L SS weld overlay after 20 and 100 min exposure are shown in Figure 43. This

coating reached steady state after 20 min of erosion. The results of the microhardness tests are summarized in Table 11. It can be seen that surface hardness, plastic zone size, and area under the curve values are similar for the 20 and 100 minutes samples. This experiment demonstrates that for the 316L SS weld alloy in the steady state regime, the size of the plastically deformed region is constant. Therefore, under steady state conditions, each particle impact will cause the same pattern of plastic deformation and, as a result, a steady state erosion rate is attained. Based upon this experiment, it is apparent that valid correlations can be made between erosion rates and measurements of the microhardness profiles, after erosion in steady state regime.

V.B.2.c. Erosion Behavior of Ductile Weld Overlay Coatings

The present results indicate that coatings with hardness values below 320 HK (Knoop hardness number) at 400°C experienced plastic deformation as a result of particle impact (Ultimet, Inconel-625, 316L SS, Iron-Aluminide, Hastelloy-22, and Stellite-6). It is well known that the hardness of a material determines the resistance to plastic deformation. For weld alloys with hardness above 320 HK, no appreciable plastic deformation was observed. Apparently, under the present erosion conditions this hardness level is sufficient to prevent significant plastic deformation due to erosion. However, for plastically deformed weld overlays no correlations were found between hardness at 400°C and volume steady state erosion rates (Figure 39b). Furthermore, the Stellite-6 weld overlay that exhibited the highest hardness also showed the highest erosion rate (0.0119 mm^3/min) among the ductile coatings. Clearly, the ability of the ductile coatings to resist plastic deformation did not contribute to the erosion resistance. Usually, the erosion of

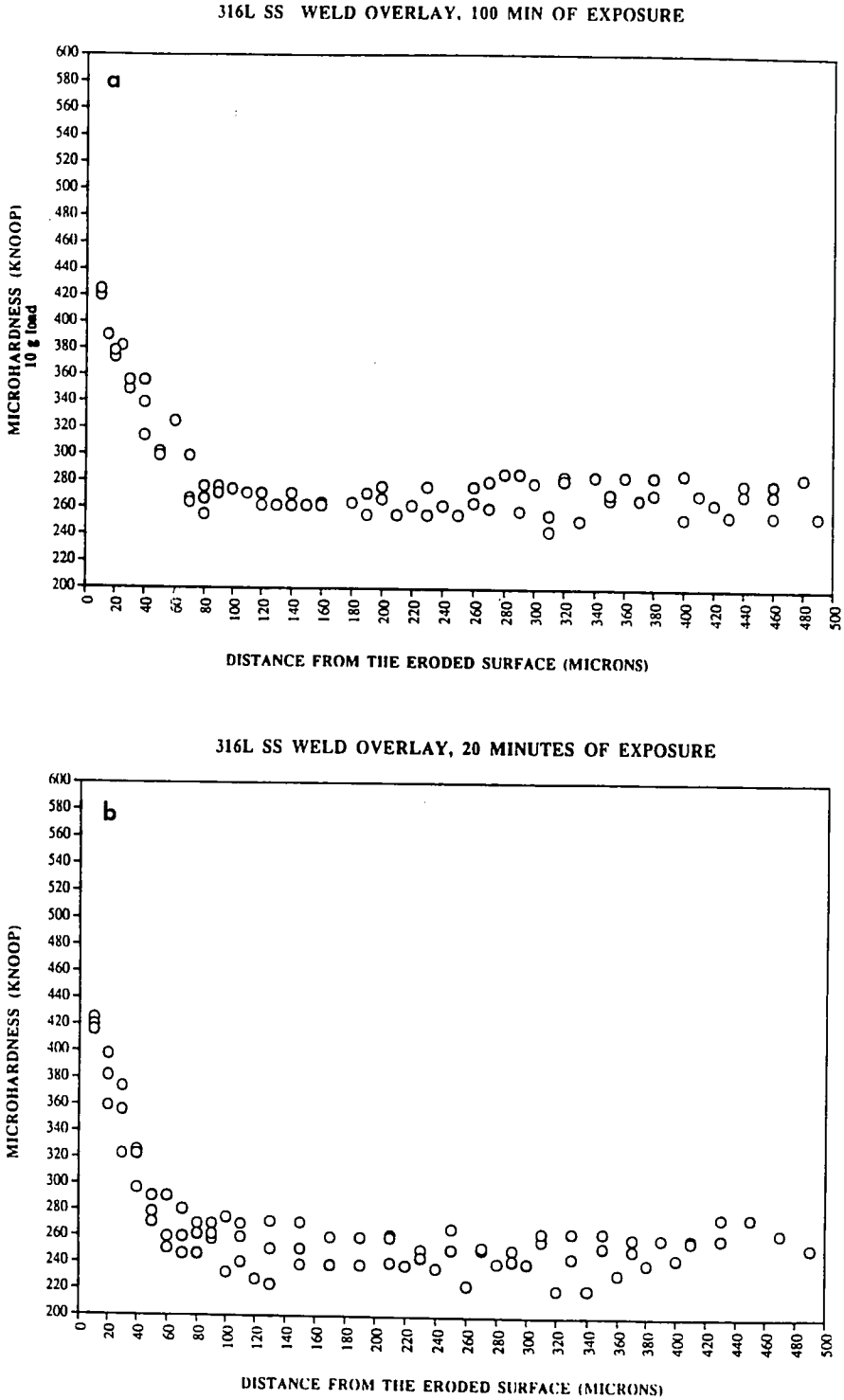

Figure 43. Microhardness profiles for 316L weld overlay coating after exposure in erosion tester at 90° impact angle; (a) 100 min. of exposure; (b) 20 min. of exposure.

Table 11. Results of the microhardness profile tests for the 316L SS weld overlay coating after 20 and 100 minutes of exposure in erosion tester at 90° impact angle.

WELD OVERLAY	BASE HARDNESS (HK_{10})	SURFACE HARDNESS (HK_{10})	PLASTIC ZONE SIZE (um)	AREA UNDER THE CURVE (kg/m)
316L SS (100 min)	267±12	437±7	70±15	6068±1586
316L SS (20 min)	253±13	445±5	65±15	6277±1602

ductile materials is accompanied by accommodation of the strain underneath the eroded surface. When a critical strain is exceeded in the deformation volume beneath the surface, the material is detached from the eroded surface by ductile fracture [5]. In this case, the ability of material to absorb impact energy through plastic deformation may play a major role in its erosion resistance.

The results of microhardness tests for weld overlay coatings are summarized in Table 12. The volumetric erosion rates for these coatings are plotted against the area under the microhardness profile curves in Figure 44. It can be seen that as the area under the curve increases the volume erosion rate decreases. The large error involved in the area under the curve measurements is a result of scatter in microhardness measurements. This scatter is due to the small applied load during the measurements. When the smallest applied load is used (10g), even small variations in microstructure of the weld have a significant effect on microhardness values. However, it is necessary to use such a small applied load because it produces a small indentation size and even small variations in microhardness with distance from the eroded surface can be detected. The "area under the curve" parameter incorporates the increase in surface hardness (or strength) due to the particle impacts ($H_{surface}$-H_{bulk}) and the distance over which this increase occurred (plastic zone size). An increase in surface hardness due to erosion represents the material's ability to strain harden, while the plastic zone size indicates the distance over which strain hardening occurs. For example, materials with a high ability to strain harden (high $H_{surface}$-H_{bulk}), require a higher applied stress to exceed the critical fracture stress than materials with low ability to strain harden (low $H_{surface}$-H_{bulk}). But if this increase in

Table 12. Results of the microhardness profile tests for the weld overlay coatings after 100 minutes of exposure in erosion tester at 90° impact angle.

WELD OVERLAY	BASE HARDNESS (HK_{10})	DELTA H $H_{surface}$-H_{base} (HK_{10})	PLASTIC ZONE SIZE (um)	AREA UNDER THE CURVE (kg/m)	VOLUME EROSION RATE (mm^3/min) x10^3
ULTIMET	390±14	315±15	55±10	8737± 1987	8.5
INCONEL-625	292±15	241±22	66±15	8105± 2546	9.4
316L SS	267±12	170±7	70±15	6068± 1586	10.0
IRON-ALUMINIDE	291±12	114±5	63±12	3646± 1412	11.0
HASTELLOY-22	290±13	203±8	48±3	4924± 536	11.4
STELLITE-6	552±34	178±10	38±7	3417± 813	11.9

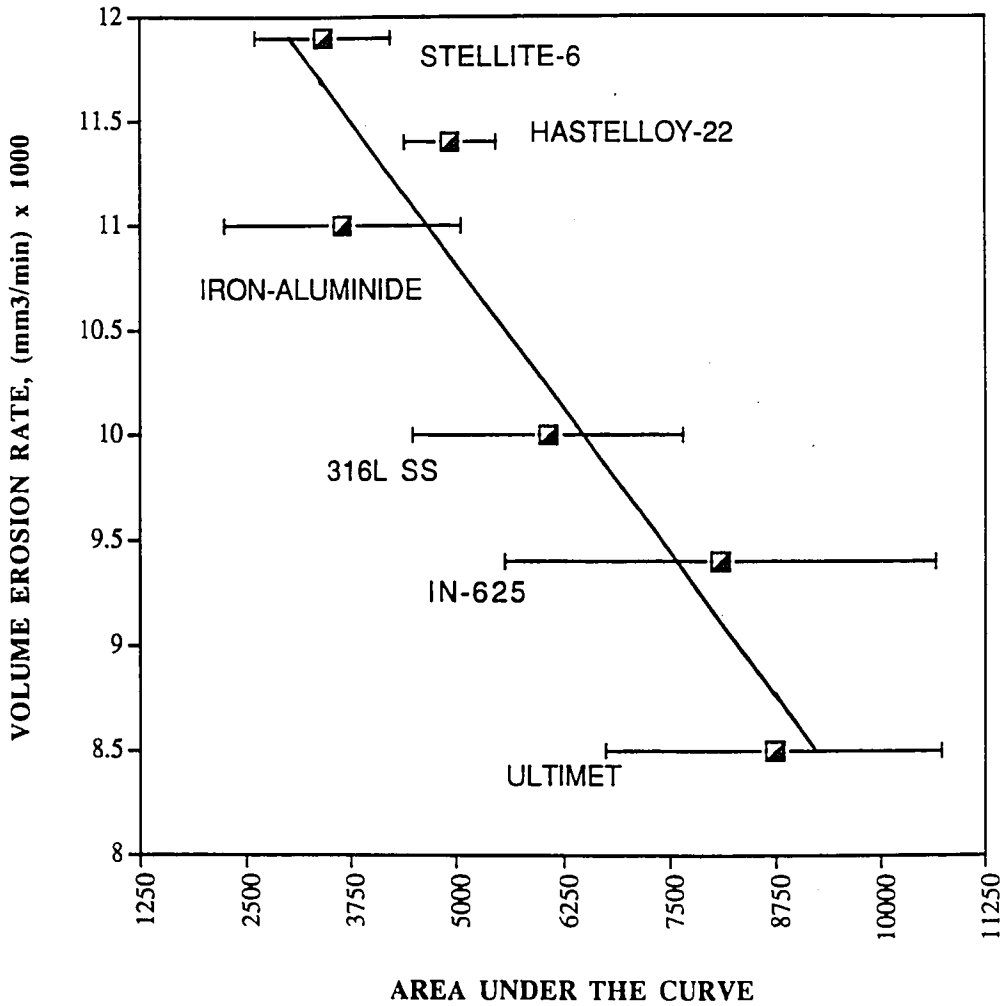

Figure 44. Effect of calculated area under the curve of microhardness versus distance from the eroded surface on volumetric erosion rates for weld overlay coatings.

stress to fracture (due to strain hardening) occurs over a small volume, it will fracture because deformation is very localized and stress to fracture can be reached after only a few impacts. On the other hand, if the material has a large plastic zone size but has low ability to strain harden (low $H_{surface}$-H_{bulk}) it will also fracture after only a few impacts. In this case, fracture may occur because only a small applied stress is needed to exceed the critical stress to fracture for the material. To illustrate that a large plastic zone size is not a sufficient requirement for erosion resistance, its effect on erosion rate is shown in Figure 45. In this figure, the volume erosion rates is plotted against plastic zone size. No correlation can be seen between these two parameters. These measurements demonstrate that a large plastic zone size does not necessarily lead to a high erosion resistance. Clearly, the calculated area under the curve is a better representation of erosion resistance because its include both strain hardening and plastic zone size.

If the energy to fracture increases ("area under the curve" increases), erosion resistance also increases. It can be concluded that ductile coatings that are able to considerably strain harden (high $H_{surface}$-H_{base}) over a large volume (large plastic zone) may have a higher energy to fracture and, therefore, good erosion resistance (Ultimet, Inconel-625, and 316L SS welds). The ability of a material to absorb impact energy before fracture is a critical parameter that controls erosion resistance.

V.B.2.d. Erosion Behavior Of Wrought Alloys

The results of the microhardness profile measurements and volumetric erosion rates for Inconel-625, 316L SS and Iron-Aluminide wrought materials at a 90° impact angle are summarized in Table 13 and plotted in Figure 46. It can be seen that as the area

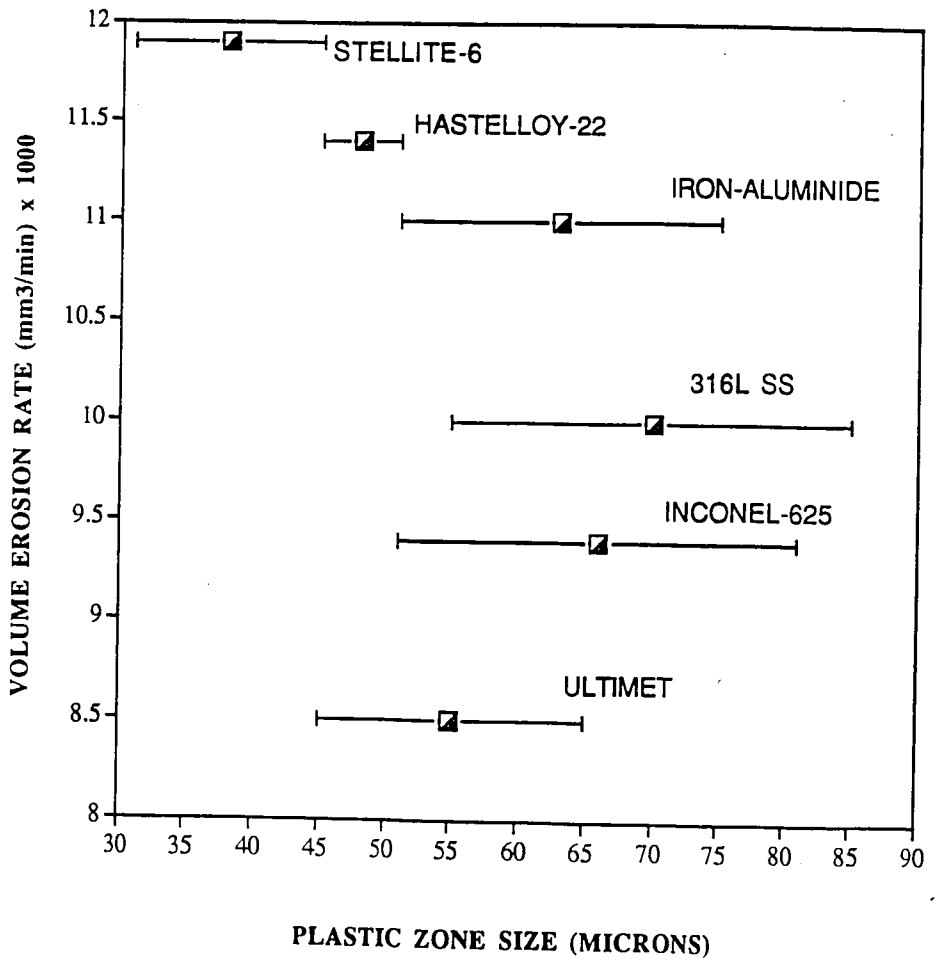

Figure 45. Effect of the measured plastic zone size on volumetric erosion rates for weld overlay coatings.

under the curve increases the erosion rate decreases. Again, the calculated area under the curve showed a good correlation with erosion resistance, suggesting that the ability to absorb impact energy during erosion is a critical parameter that controls the erosion behavior of the material. In order to confirm that this parameter can also be used for explaining erosion behavior of others alloy systems, data from the literature was used to calculate the area under the microhardness profile curves. Reddy et. al [22,58] have studied the erosion behavior Cu and Cu-Zn alloys. They obtained microhardness profiles for these materials after erosion (see Figure 47). The following erosion test conditions were used in their work: particle velocity 40 m/sec, particle material-AISI 4140 steel, particle size 300-450 microns, particle impact angle-90°. The reported steady state erosion rates, plastic zone sizes, and surface hardness along with the calculated areas under the curves are shown in Table 14. According to Reddy et. al [58] the steady state erosion rate for each tested material was reached when the weight loss rate became independent from the total weight of the impacting particles. The erosion rate was measured in gram/gram, which means materials weight loss per weight of the impacting particles. The values of the area under the microhardness profiles curves were calculated based upon this data and also presented in Table 14. The reported erosion rates are plotted against calculated area under the curves values in Figure 48. It can be seen that an observed increase in area under the curve led to an increase in erosion resistance for Cu and Cu-Zn alloys. Similar effects were found for weld overlays and Inconel-625, 316L SS and Iron-Aluminide wrought alloys. This result demonstrate that the "area under the curve" parameter, that accounts for energy to fracture during erosion, may be used to

Table 13. Results of the microhardness profile tests for the wrought alloys after 100 minutes of exposure in erosion tester at 90° impact angle.

ALLOY	BASE HARDNESS (HK_{10})	DELTA H $H_{surface}H_{base}$ (HK_{10})	PLASTIC ZONE SIZE (um)	AREA UNDER THE CURVE (kg/m)	VOLUME EROSION RATE (mm^3/min) $x10^3$
INCONEL-625	339±20	252±10	62±18	7931± 2508	6.0
316L SS	271±15	132±8	72±18	4832± 1422	6.7
IRON-ALUMINIDE	346±15	132±8	38±12	2512± 963	7.4

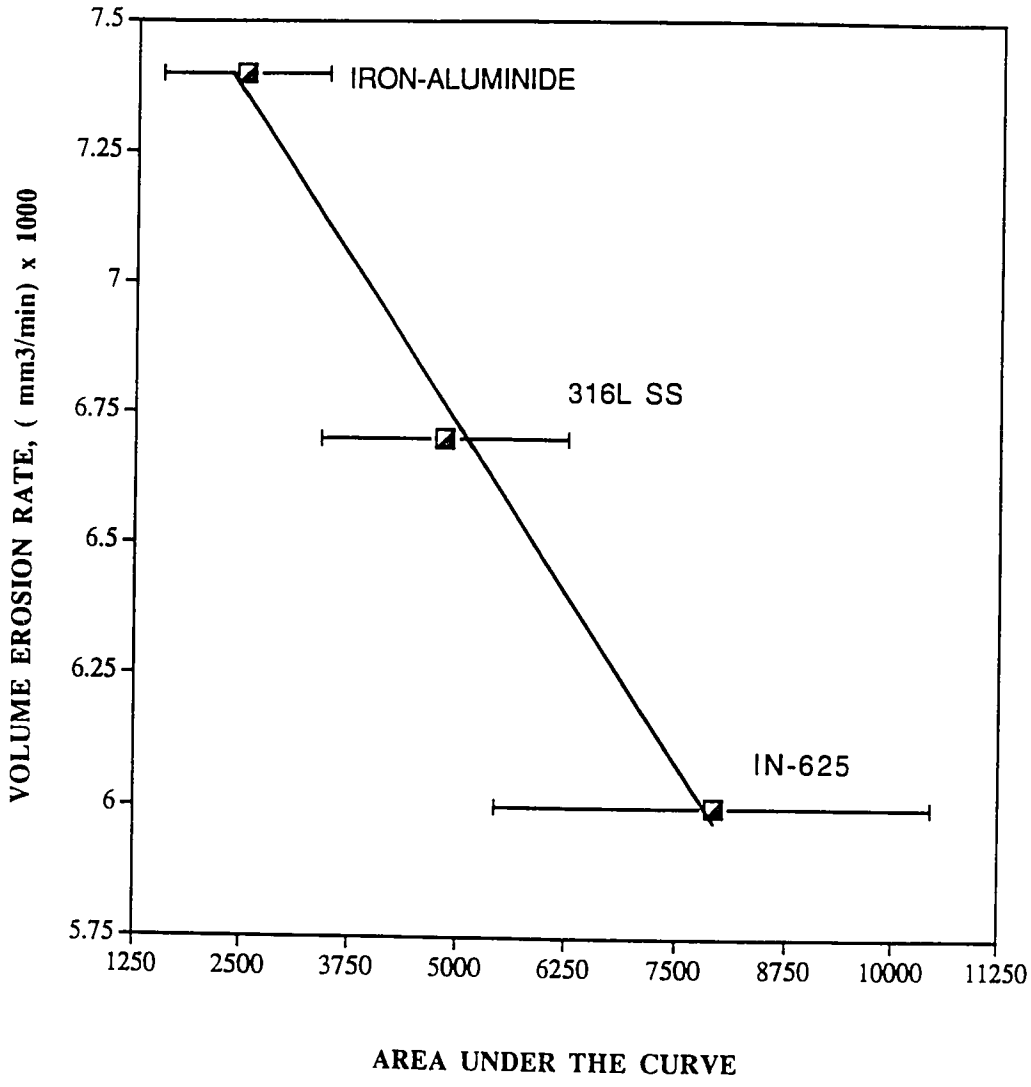

Figure 46. Effect of calculated area under the curve of microhardness versus distance from the eroded surface on volumetric erosion rates for wrought alloys.

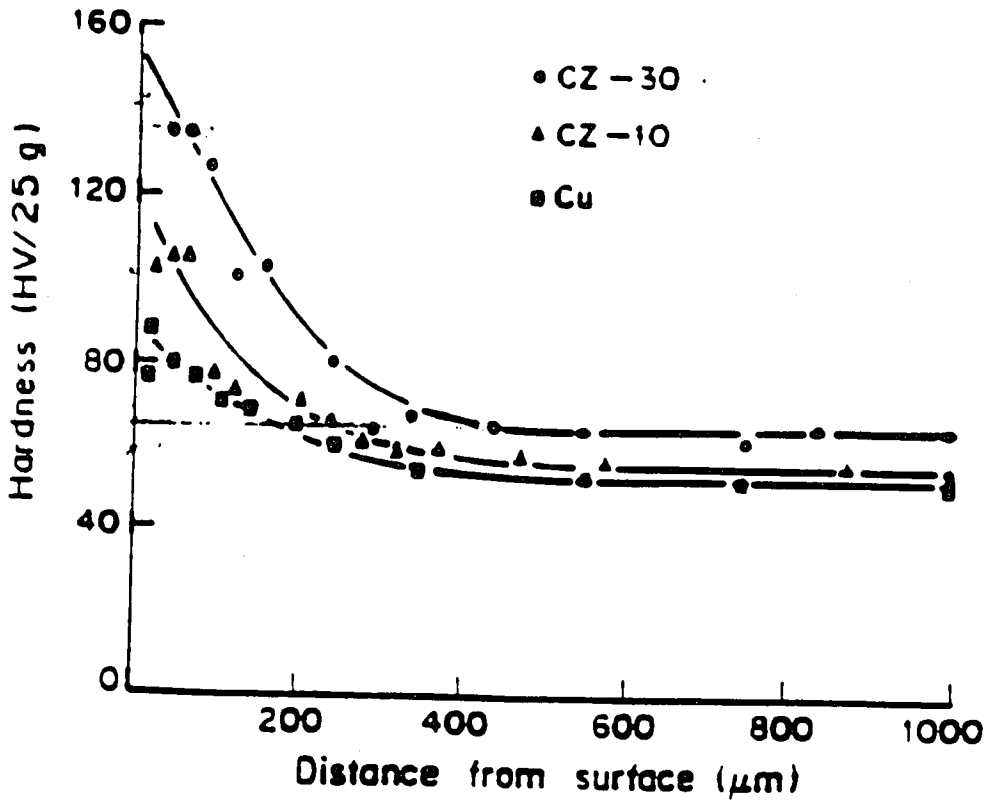

Figure 47. Microhardness profiles for Cu and Cu-Zn alloys after exposure in erosion tester at 90° impact angle. The profiles were obtained by Reddy et.al [58].

Table 14. Results of the microhardness profile tests for Cu and Cu-Zn alloys [22, 58]. The area under the curve for each alloy was calculated in present work base upon the reported data.

ALLOY	SURFACE HARDNESS $H_{surface}$ (HV_{25})	DELTA H $H_{surface}$-H_{base} (HV_{25})	PLASTIC ZONE SIZE (um)	AREA UNDER THE CURVE (kg/m)	EROSION RATE (g/g)X10^{4}
Cu	90	39	240	4680	4.65
Cu-10%Zn	103	50	220	5500	4.45
Cu-30%Zn	127	64	250	8000	3.25

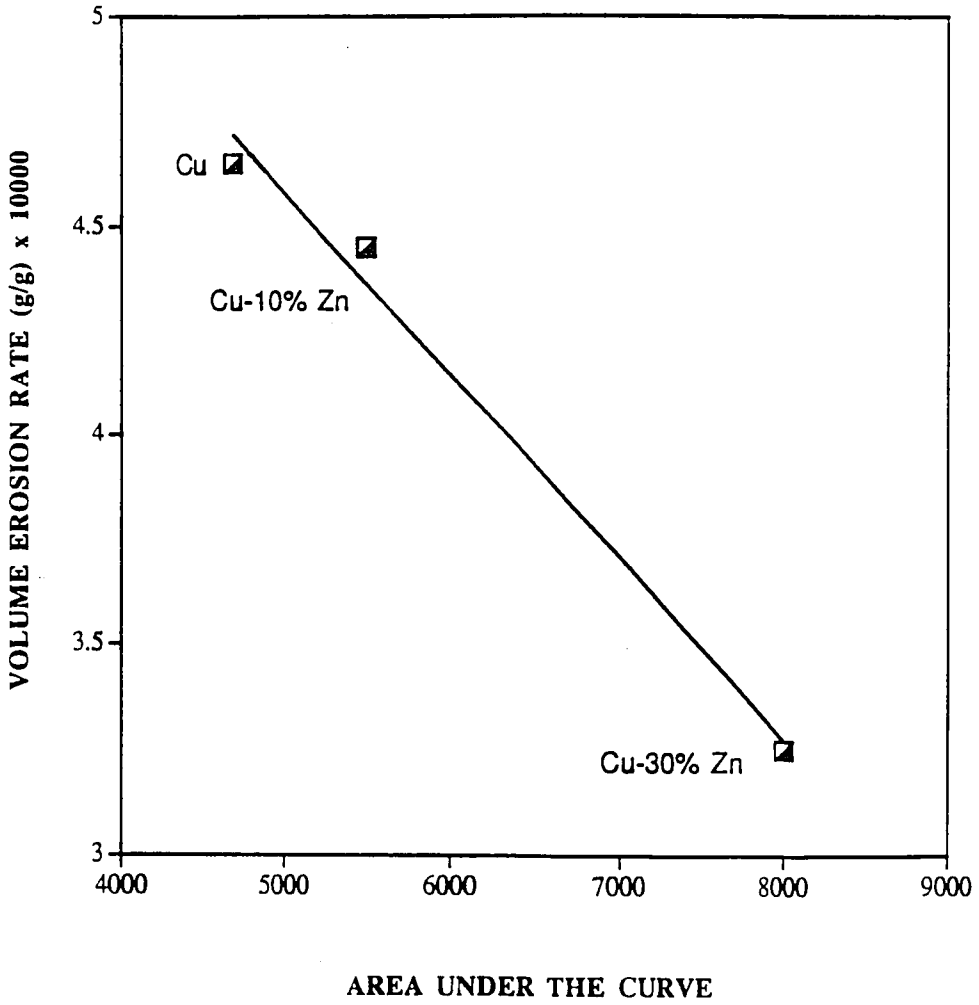

Figure 48. Effect of calculated area under the curve of microhardness versus distance from the eroded surface on volumetric erosion rates for Cu-Zn alloys.

explain erosion behavior of various alloy systems.

This analysis of the microhardness profile was also used to examine the erosion behavior of the wrought alloys at 90° and 30° impacts. The microhardness profiles for these alloys at 90° and 30° impact angles are shown in Figure 38 (a-e). The results along with the volumetric erosion rates for 316L and Inconel-625 wrought alloys are summarized in Table 15. It can be seen that erosion rates for these alloys are significantly higher at a 30° impact angle than at a 90° angle. From the microhardness profile data it was also observed that Inconel-625 and 316L alloys showed a considerably lower increase in surface hardness ($H_{surface}$-H_{bulk}) at 30° than at 90°. As a result, the calculated area under the curve was also small for the 30° impact. This data reveals that for these alloys at a 30° impact angle, the critical stress to fracture ($H_{surface}$) is smaller than at 90°. Thus, a much lower impact stress is needed to remove material from the surface when eroded at an oblique angle.

The impact at 30° involves a shear deformation, while impact at 90° involves primarily a compression. Apparently, shear deformation requires a smaller flow stress compared with compression or tension. It was shown by Meyers et.al [59] that $\delta_{max}=\sigma_y/1.7$, where δ_{max} is a maximum shear stress and σ_y is a yield stress of the material. It can be seen that a smaller stress is required to cause shear deformation compare with stress that is necessary to cause yielding. Therefore, material can be more easily removed when eroded at 30° impact. As a result of this, erosion rates are significantly higher for Inconel-625 and 316L alloys at 30° than at 90°.

From the results of the erosion tests it was established that the steady state erosion

Table 15. Results of the microhardness profile tests for the 316L SS and IN-625 wrought after 100 min of exposure in erosion tester at 30° and 90° impact angles.

ALLOY	DELTA H $H_{surface}$-H_{base} (HK_{10})		PLASTIC ZONE SIZE (um)		AREA UNDER THE CURVE (kg/m)		VOLUME EROSION RATE (mm^3/min) $x10^3$,	VOLUME EROSION RATE (mm^3/min) $x10^3$,
	30°	90°	30°	90°	30°	90°	30°	90°
316L SS	115 ±20	132 ±8	49 ±11	70 ±15	2928± 1123	4832± 1422	10.9	6.7
INCONEL-625	107 ±20	251 ±10	50 ±11	62 ±18	2786± 1090	7931± 2508	9.4	6.0

rate for Inconel-625 wrought alloy is significantly higher at 30° than at 90° (0.0094 and 0.0060 mm^3/min, respectively). For the weld alloys the differences between the erosion rates at 30° and 90° were much smaller (0.0071 and 0.0079 mm^3/min, respectively).

Scanning Electron Microscopy (SEM) was used for observation of the eroded surfaces of the Inconel-625 alloy in the weld and wrought forms after 100 min exposure in the erosion tester. SEM photomicrographs of the eroded surfaces of Inconel-625 alloy at 90° and 30° impact angle are shown in Figures 49(a-f). From Figures 49a and 49c it can be seen that the eroded surface appeared to be similar for wrought and weld alloys at 90° impact angle. Both have a significant amount of topography and surface roughness. However, the surface appearance at the 30° impact angle for the wrought alloy is considerably different from the 90° impact angle. The surface of the wrought alloy (Figure 49b) possessed a substantial amount of deep gouging (see arrows) oriented in the direction of the particle impact. Gouging is typical for ductile materials when eroded at oblique angles. On the other hand, the eroded surface of the weld alloy at 30° did not exhibit such distinct gouging. Although some evidence of gouging can be seen (see arrows), they are not as well defined as for the wrought alloy. For the wrought alloy, the surface appearances at 30° are considerably different then at 90°, while for the weld alloy these differences are not as striking. High magnification SEM photomicrographs of the eroded surfaces for wrought and weld alloys at 30° are shown in Figure 49(e,f). The differences between surface appearances are evident. These observations are in agreement with the erosion test results, since for wrought alloy erosion rates are also significantly different at 30° and 90° impact, while for weld alloy the differences were not as notable.

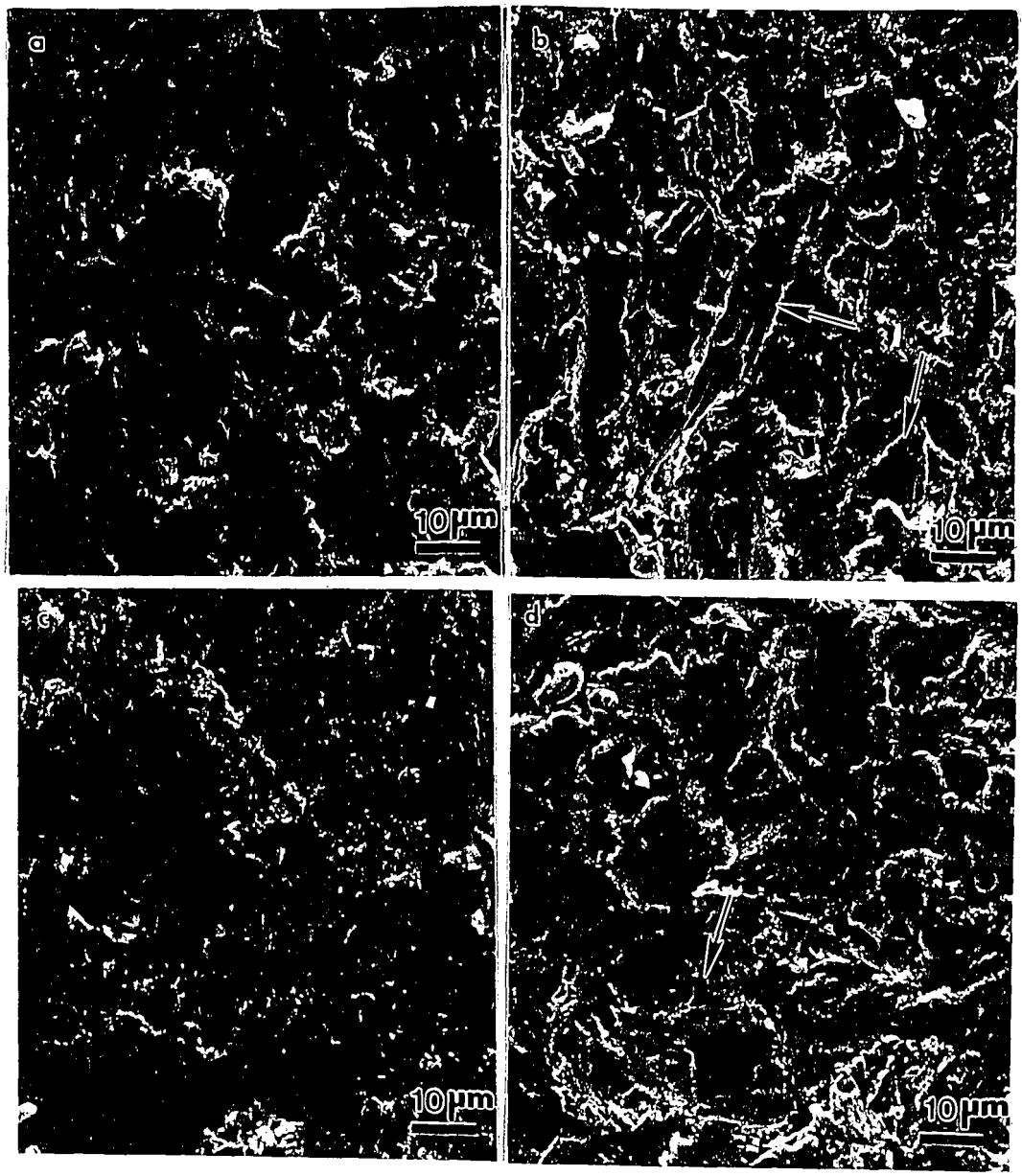

Figure 49. Secondary Electron Image of the eroded surface of the Inconel-625 wrought and weld alloys after 100 minutes of exposure in erosion tester; (a) wrought alloy, 90° impact angle; (b) wrought alloy, 30° impact angle; (c) weld alloy, 90° impact angle; (d) weld alloy 30° impact angle. Arrows indicate gauging.

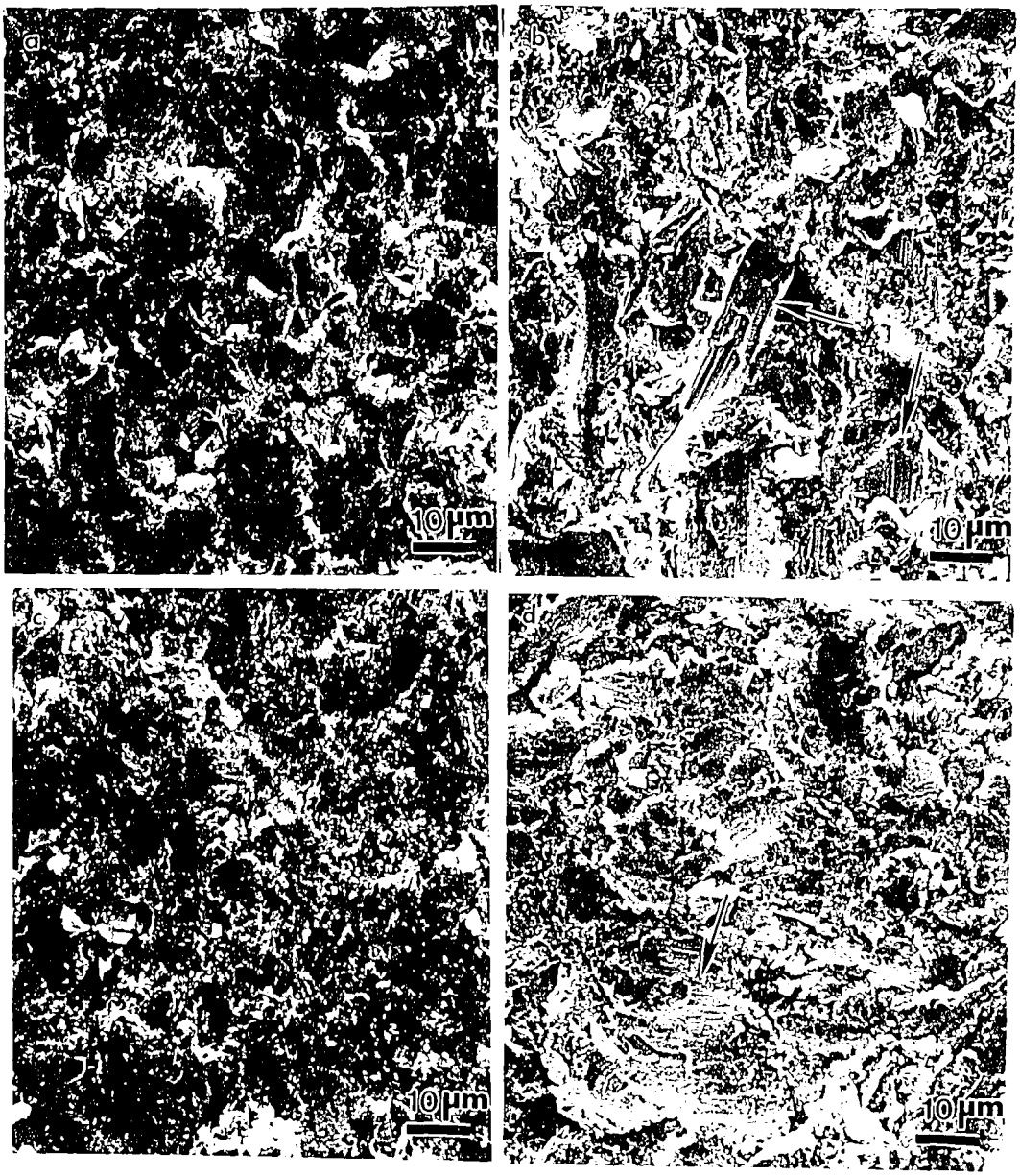

Figure 49. Secondary Electron Image of the eroded surface of the Inconel-625 wrought and weld alloys after 100 minutes of exposure in erosion tester; (a) wrought alloy, 90° impact angle; (b) wrought alloy, 30° impact angle; (c) weld alloy, 90° impact angle; (d) weld alloy 30° impact angle. Arrows indicate gauging.

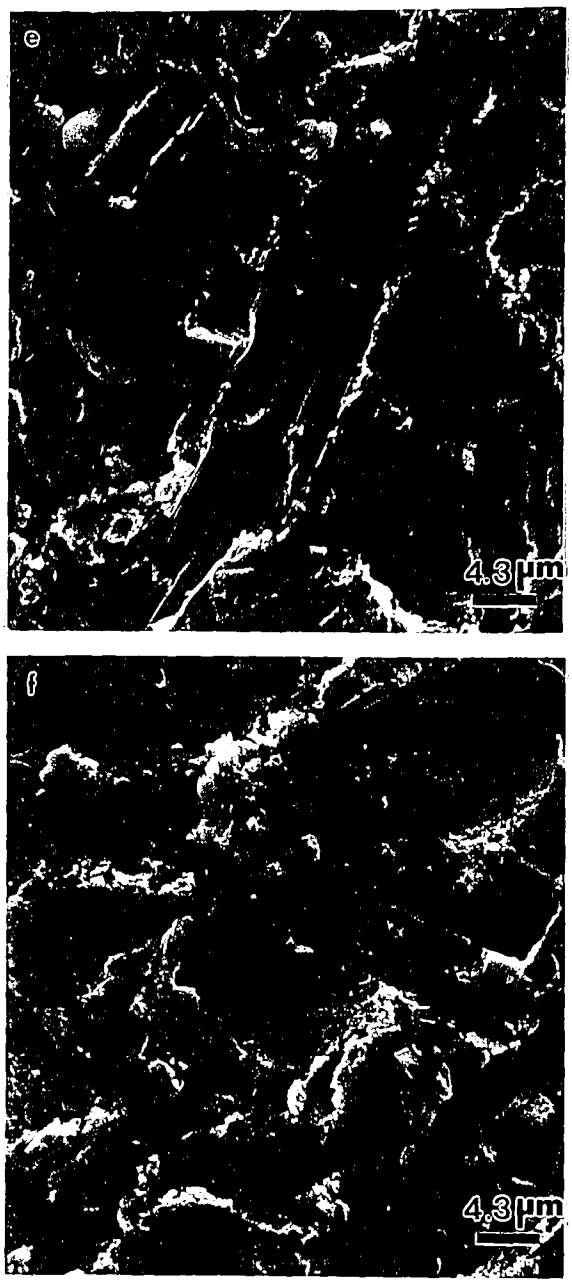

Figure 49 (e,f). Secondary Electron Image of the eroded surface after 100 minutes of exposure in erosion tester at 30° impact angle; (e) wrought alloy; (f) weld alloy.

Figure 49 (e,f). Secondary Electron Image of the eroded surface after 100 minutes of exposure in erosion tester at 30° impact angle; (e) wrought alloy; (f) weld alloy.

The light optical micrographs of Inconel-625 wrought and weld alloy is shown in Figure 21. Inspection of the photomicrographs showed that the weld overlay microstructure is significantly finer than the wrought alloy microstructure. The microstructure of the weld alloy consists of gamma (γ) phase dendrites and interdendritic regions of NbC type carbides and Laves phases [49,50] (see section IV.A.2.). The microstructure of the wrought alloy consists of small equiaxed grains and annealing twins. Large columnar grains also can be observed. It has been documented that second phase particles may disrupt material plastic flow during erosion [12]. Thus, for the weld overlay coating, second phase particles may prevent removal of material at a 30° impact angle because they free path for the impacting particle and plastic flow that cause material removal will be low. The "free path" term can be define as a distance over which plastic flow that resulted from the particle impact has occurred. In this case the erosion rates at 30° and 90° are expected to be similar. For the wrought alloy, erosion at 30° may involve a substantial plastic flow because the "free path" for the plastic flow is large. The 30° impact involves more abrasion type wear compared with 90° impact. During impact at oblique angles, particles can slide along the surface of the material. Therefore, for wrought alloy, if no second phase particles are present each impact may cause a significant plastic flow. These factors might be responsible for the considerable differences in surface appearances for the Inconel-625 wrought alloy at the 30° and 90° particle impact angle.

Based upon the presented results, it is apparent that the ability of the ductile materials to absorb impact energy through plastic deformation is a critical factor that controls the

erosion behavior. The impact energy can be absorbed through the increase in surface hardness (strain hardening) over a certain volume of the material. The energy to fracture due to erosion can be estimated by calculating the area under the curve of hardness versus distance from the eroded surface. The best erosion resistance can be achieved when a large increase in surface hardness ($H_{surface}$-H_{base}) occurs over a large volume of material (plastic zone size). In this case, the calculated area under the curve (energy to fracture) is maximized and the erosion rate is low. It is essential to determine the mechanical property or combination of the properties that provide the maximum area under the curve. If these properties are identified, the intelligent selection of the erosion resistant coatings can be made.

The results and discussion presented in sections IV and V describe erosion behavior of the commercially available weld overlay and wrought alloys at elevated temperature (400°C). The relative ranking of erosion resistance for weld overlay coatings was developed. Two groups of materials were identified (ductile vs. brittle) depending upon their erosion behavior. Although, some alloys from each group may show similar erosion rates, the factors that contribute to their erosion resistance are different.

VI. CONCLUSIONS

The erosion behavior of eleven commercially available weld overlay coatings were evaluated. The following can be concluded based upon the results of this research:

1. The relative ranking of the erosion resistance of the coatings at elevated temperature (400°C) for both 90° and 30° particle impact angles was developed. The Ultimet, Inconel-625 and 316L SS showed the lowest overall volumetric steady state erosion rates at both impact angles.

2. Abrasion resistant coatings such as Stellite-6, B-60, and Armacor-M exhibited poor erosion resistance at 400°C compared with corrosion resistant alloys (Inconel-625 and 316L SS). Since the mechanisms for abrasion and erosion wear are expected to be different, the selection of erosion resistant weld overlays can not be based upon abrasion resistance.

3. 316L SS, Inconel-625, Ultimet, Iron-Aluminide, Hastelloy-22, and Stellite-6 weld overlays plastically deformed due to erosion at 90° impact angle, while High Chromium Iron, 420 SS, TS-2, B-60, and Armacor-M did not deform appreciably. Therefore, the mechanisms that control erosion behavior are different for these two groups of coatings.

a. BRITTLE COATINGS

An increase in hardness for coatings that did not deform plastically (Armacor-M, B-60, High Cr Iron, 420 SS, and TS-2 led to a decrease in their erosion resistance. This effect was attributed to the decrease in fracture toughness with an increase in hardness. For this group of brittle materials, a combination of relatively high hardness to prevent plastic deformation and fracture toughness may provide excellent erosion resistance.

b. DUCTILE COATINGS

No correlation were found between hardness at 400°C and volumetric erosion rate 90° impact angle for coatings that deformed plastically (Ultimet, 316L SS, Inconel-625, Iron-Aluminide, Hastelloy-22, Stellite-6). It was established that an increase in calculated area under the curve of hardness versus distance from the eroded surface led to a decrease in erosion resistance. The increase in area under the curve corresponds to an increase in amount of energy that the material can absorb before fracture. This indicate that materials with the ability to strain harden over a large volume may show good erosion resistance. Wrought materials such as Inconel-625, 316L SS, and Iron Aluminide also showed an increase in erosion resistance with an increase in calculated area under the curve. These results suggest that the amount of energy that a material can absorb through plastic deformation before it will fracture may be a critical parameter that controls erosion resistance for different classes of

ductile materials.

4. The Inconel-625 and 316L SS wrought alloys showed significantly higher erosion rates at 30° impact angle than at 90°. From the obtained microhardness profiles, it was determined that a considerably lower stress level is required to cause fracture for these alloys when impacted at 30°.

REFERENCES

1. Lamarre, L., EPRI Journal, October/November, 1990, pp. 31-37.
2. Hutchings, I.M., Monograph On The Erosion Of Materials By Solid Particle Impact, MTI Publication No 10, 1983.
3. McCabe, L.P., Sargend, G.A., and Conrad, H., Wear, vol. 105, 1985, 257-277.
4. Hutchings, I.M. and Levy, A.V., Wear, vol. 131, 1981, pp. 105-121, 1989.
5. Sundararajan, G., and Shewmon, P.G., Wear, vol. 84, 1983, pp. 237-258.
6. Veerabhadra Rao, P., Young, S.G., and Buckley, D.H., Wear, vol.85, 1983, pp. 223-237.
7. Hutchings, I.M., Journal Of Applied Physics, 25, 1986, pp. A212-A221.
8. Atkins, A.G. and Mai, Y-W, Journal Of Material Science, 21, 1986, pp. 1093-1100.
9. Hertzberg R.W., Deformation and Fracture Mechanics of Engineering Materials, third edition, 1989, John Wiley and Sons.
10. Hutchings, I.M., Corrosion/Erosion of Coal Conversion Systems (Proc. Conf.), January, 1979, pp.393-428.
11. Doule, R.A, and Ball, A., Wear, Vol. 151, 1991, pp. 87-95.
12. Ninham A., Wear Of Materials 1987 (Conference Proceeedings), pp. 813-823.
13. Hutchings, I.M., and Levy, A., Wear, Vol. 131, 1989, p. 105.
14. Richman, R.H. and McNaughton W.P., Wear, Vol 140, 1990, pp. 63-82.
15. Levy, A., and Jahamir, Corrosion-Erosion Behavior Of Materials, edited by Natesan, K., Metallurgical Society Of AIME, New York, 1980, p. 177.
16. Oca, Y. and Hutchings I.M., Corrosion Engineering, 39, 1990, pp.677-687.
17. Guo, D.Z., Wang, L.J., and Li, J.Z., Wear, Vol. 161, 1993, pp. 173-178.
18. Wert, J.J., and Oppliger., S.J., Materials Science and Technology, Vol. 8, September, 1992, pp. 825-835.
19. Ruff, A.W., and Wiederhorn, S.M., Treatise on Materials Science and Technology (ed. C. Preece), Vol.16, 1979, pp.69-124, New-York/London, Academic Press.
20. Ball, A., Wear, Vol. 91, 1983, pp.201-207.
21. de Gee, A.W.J., Wear, Vol. 81, 1981, p. 373.
22. Venugopal Reddy, A. and Sundararajan, G., Wear, Vol. 103, 1985, pp. 133-148.
23. Srinvas M., Malakondaiah, G., Linda Murty, K., and Rama Rao, P., Scripta Metallurgica et Materialia, Vol. 25, 1991, pp.2585-2588.
24. Srinvas, M., Malakondaiah, G., and Rama Rao, P., Acta Metallurgica et Materialia, Vol. 41, No. 4, 1993, pp. 1301-1312.
25. Argon, A.S., Im, J., and Safoglu, R., Metallurgical Transactions, 6A, 1975, p. 825.
26. Lawn, B.R., Evans, A.G., and Marshall, D.D., Journal of American Ceramic Society, 63, 1980, p. 574.
27. Metals Handbook, Volume 11: "Friction, Lubrication and Wear Technology", American Society for Metals, p. 206-207, 757-765, 1992.
28. Misra, A. and Finnie, I., Wear, Vol 68, p.33-39, 1981.
29. Anand, K., and Conrad, H., Wear of Materials (Proceedings), 1989, ASME, pp. 135-142.

30. Ellis, D. and Squires, R., Metal Construction, p. 388-393, July, 1983.
31. Berns, H., Fischer, A. and Theisen, W., Wear of Materials, Vol 2, p. 601-610, 1989.
32. Ninham, A. and Levy A., Proceedings of International Conference on Wear of Materials, American Society of Mechanical Engeeners, p. 325-332, 1983.
33. Berns, H., Fischer, A. and Theisen, W., Wear of Materials, Vol. 2, p. 535-542, 1987.
34. Lugscheider, E., Krautward, A., Eschnauer, H. and Wilden, J., Surface Coatings Technology, 32, p. 273-284, 1987.
35. Report, EPRI-NP-4993, " Laboratory Evaluations of Cobalt-Free, Nickel-Based Hardfacing Alloys for Nuclear Applications", 1987.
36. Metals Handbook, Volume 9: "Metallography and Microstructures", 9th edition, p. 309.
37. Scoll, M., Devanathan, R. and Clayton, P., Wear, 135(2), p. 355-368, 1990.
38. Dawson, R., Shewchuk, S. and Pritchard, J., Welding Journal, p.15-23, November, 1982.
39. Scruggs, D., Welding Journal, August, 1991.
40. Johnson, M., Mikkola, D.E., March, P.A., and Wright, R.N., Wear, Vol. 140, 1990, pp. 279-289.
41. Stoloff, N.S. and Davies, R.G., Letters to the Editor, Acta Metallurgica, Vol. 11, October, 1963, pp. 1187-1188.
42. Metals Handbook, Vol. 6, 7th Ed., Gas Metal Arc Welding, ASM, Metals Park, Ohio, 1983.
43. DuPont, J.N., Masters Thesis, Lehigh University, 1994.
44. Lewnard, J., Air Products and Chemicals, Private Communications.
45. Levy, A.V., and Wang, B., Surface and Coatings Technology, Vol. 33, 1987, pp. 285-299.
46. Tennini, M. and Nakagava, T., Journal of JSLE International Edition, 10, 1989, p.39.
47. Edited by Boyer, H.E., Hardness Testing, 1987, ASM International.
48. ASTM E 384 Standard, Annual Book of ASTM Standurds, vol. 03.01, Metals Tests Methods and Analitical Procedures, 1988.
49. Ciezlak, M.J., Welding Research Supplements, February 1991, pp. 49-56.
50. Bordos, P.I., Gupta, K.P., and Beck, P.A., Transactions TMS-AIME, vol. 221, 1961, p. 1087.
51. Aptecar, S.S. and Kosel, T.H., Proceedings Wear of Materials Conference, 1985, pp. 677-686.
52. Sharpless, R.V., and Gooch, T.G., Welding Research Supplements, May 1992, pp. 195-200.
53. Sundararajan, G., Wear, 162-164, 1993, p. 773.
54. Lou H.O., and Krizman A., Wear, 134, 1989, p. 253.
55. Latzko, D.H., Post-Yield Fracture Mecahnics, 1979, Applied Science Publishers LTD, London, pp. 211-253.
56. Ikeda, M., Umeda, T., Tong, C. P., Suzuki, T., Niwa, N., and Kato, O., ISIJ International, vol. 32, n. 11, 1992, pp. 1157-1162.
57. Tabor, D., The Hardness Of Metals, Clarendon Press, Oxford, 1951.
58. Reddy A.V., Sundararajan G., Sivakumar, R., and Rama Rao, P., Acta Metallurgica,

vol. 32, 1984, pp. 1305-1316.
59. Meyers, M.E., and Chawla, K.K., Mechanical Metallurgy principles and applications, Printice-Hall, Inc., Englewood Cliffs, New Jersey, 1984, pp. 612-615.

VITA

Boris Feliksovich Levin was born to Felix and Anna Levin on June 15, 1968 in Moscow, Russia. He received his secondary degree from Moscow high school # 201 in the spring of 1985. The fall of the same year he enrolled at Moscow Institute of Steel and Alloys, where he completed four years.

Boris enrolled Lehigh University in January of 1992 and began work on his M.S. in the Material Science and Engineering department. Mr. Levin is a member in good standing of ASM International.

END OF TITLE